SPIZWURZ Benchmark Phase 1

Blind Benchmark Report

Version 1

GRS - 856

Gesellschaft für Anlagen-
und Reaktorsicherheit
(GRS) gGmbH

SPIZWURZ Benchmark Phase 1

Blind Benchmark Report

Version 1

Aleksandra Rezchikova (GRS)
Juri Stuckert (KIT)
Jürgen Sievers (GRS)
Robert Kilger (GRS)

April 2026

Remark:

This report refers to the in-house research project RS1586A which has been funded by German Federal Ministry for the Environment, Climate Action, Nature Conservation and Nuclear Safety (BMUKN).

The work was conducted by Gesellschaft für Anlagen- und Reaktorsicherheit (GRS) gGmbH.

The authors are responsible for the content of the report.

GRS - 856
ISBN 978-3-911727-49-5

Keywords
Blind Benchmark, Creep, Dry storage, Fuel rod, Hydrides, Spent nuclear fuel, SPIZWURZ

Abstract

The originally licensed dry storage period of 40 years for spent nuclear fuel requires extension due to the lack of a duly available final disposal facility in Germany. The assessment of fuel rod integrity at the end of extended storage periods relies heavily on numerical predictions. Therefore, the development, verification, and validation of reliable fuel performance codes are essential to allow for a robust safety assessment of long-term dry storage operation.

Within the framework of the SPIZWURZ project, the SPIZWURZ bundle experiment at KIT was conducted to provide an experimental basis for model development and validation. In this test, a fuel rod bundle was subjected to a gradual cooling transient over a period of 250 days, with an average cooling rate of approximately 0.95 °C per day. The experiment generated integral measurement data on cladding creep deformation and hydrogen behavior under conditions representative of dry storage.

This report documents the results of a blind benchmark exercise performed to assess the capability of existing fuel performance codes to predict the thermo-mechanical and hydrogen-related phenomena occurring during a long-term cooling transient. The benchmark results provide insight into the current predictive capabilities and limitations of the applied models and contribute to their further improvement for safety assessments of extended dry storage.

Acknowledgements

The authors gratefully acknowledge all participants of the benchmark exercise for their dedicated involvement and valuable technical contributions. The study benefited from the contributions of the following individuals:

- Carlos Aguado Basabe – CIEMAT, Spain
- Martin Dostal – ÚJV Řež, Czech Republic
- Akram El Abdi – EDF, France
- Emmanuel Jannot – Framatome GmbH, Germany
- Changhyun Jo – SNU, South Korea
- Francisco Feria Marquez – CIEMAT, Spain
- Mikhail Kolesnik – KIT, Germany
- Piotr Konarski – PSI, Switzerland
- Youho Lee – SNU, South Korea
- Verma Lokesh – PSI, Switzerland
- Aleksandra Rezchikova – GRS gGmbH, Germany
- Francisco Rotea – CNEA, Argentina
- Radan Sedláček – Framatome GmbH, Germany
- Martin Zemek – Axpo Power AG, Switzerland

The authors would like to sincerely acknowledge the contributions of Karlsruhe Institute of Technology (KIT) Institute for Applied Materials (IAM) for conducting the experimental work presented in this benchmark report. The authors would also like to thank Mirco Große, Mikhail Kolesnik, Conrado Rößger, and Sarah Weick for their contributions and continued support.

The authors would like to take this opportunity to extend their sincere appreciation to Maik Stuke and Felix Boldt, former GRS colleagues, for their invaluable contributions in the initiation of the SPIZWURZ project and the establishment of the benchmark.

Table of Contents

1 Introduction

Spent nuclear fuel passes through multiple storage phases after being discharged from a reactor. In Germany's strategy for managing spent nuclear fuel, the fuel is initially stored for a short period in on-site cooling pools before being transferred to dry storage in dual-purpose casks. The originally authorized storage period is up to 40 years. However, since the timeline for commissioning a final geological repository remains uncertain, this period must now be extended to a longer, however, unknown period of time into the future, necessitating an additional licensing agreement. Up to 100 years or longer are currently under consideration.

Ensuring fuel integrity over the entire storage period is one critical safety requirement. Its assessment relies largely on numerical simulations, since experimental data are limited. Moreover, real dry storage conditions can be reproduced only partially in experiments due to time periods that extend over decades, and safety constraints associated with handling irradiated materials. Therefore, the development of reliable and robust numerical tools is of paramount importance.

Hydrogen-related effects are considered one of the primary fuel rod degradation mechanisms during long-term dry storage, yet they remain not fully understood. The joint research project SPIZWURZ[1] between the Karlsruhe Institute of Technology (KIT) and the Gesellschaft für Anlagen- und Reaktorsicherheit (GRS) was thus initiated to investigate hydrogen behavior in fuel rod cladding tubes during long-term dry storage of spent nuclear fuel in transport and storage casks. This project was funded by the Federal Ministry for the Environment, Climate Action, Nature Conservation and Nuclear Safety (BMUKN).

Within the framework of the SPIZWURZ project, the SPIZWURZ bundle test was conducted at the KIT-LICAS[2] facility. A bundle of 21 electrically heated fuel rod simulators, each 2.5 m in length, was subjected to a slow cooling process over a period of 250 days. The temperature at the center of the bundle initially reached a maximum of 405 °C and decreased to 165 °C by the end of the experiment, corresponding to an average cooling

[1] SPIZWURZ – **Sp**annungs**i**indu**z**ierte **W**asserstoff**u**mlagerung in Brennstabhüllrohren während längerfristige**r** **Z**wischenlagerung (Stress-induced hydrogen rearrangement in fuel rod claddings during long-term dry storage)

[2] LICAS - **L**ong-term **I**nvestigation of **C**l**A**ddings behavior under **S**torage conditions

rate of approximately 0.95 °C per day. It should be noted that the experimental duration was limited due to project constraints. In contrast, the cooling rates encountered under actual dry storage conditions are substantially lower - by approximately one to two orders of magnitude - than those applied in the SPIZWURZ experiment. The non-irradiated cladding tubes were pre-charged with hydrogen at two different levels to simulate hydrogen uptake during reactor operation. Combined with two pressurization levels and a bell-shaped axial temperature profile, this setup enabled the simultaneous examination of various initial conditions.

The post-test measurements conducted on the cladding tubes from the SPIZWURZ bundle, including the quantification of creep strains and the characterization of hydride distribution and morphology, form the foundation of the SPIZWURZ Benchmark, which aims to validate and improve the modeling of creep and hydrogen behavior in cladding materials under dry storage conditions.

2 SPIZWURZ Benchmark Description

The SPIZWURZ Benchmark was designed to be carried out in two distinct phases:

1. Blind Benchmark (first phase);
2. Open Benchmark (second phase).

In the first phase of the benchmark, the existing fuel performance codes are compared against the experimental results obtained from the bundle experiment conducted as part of the SPIZWURZ project. This phase aims to evaluate the accuracy and reliability of the current models in predicting the behavior of fuel rods during dry storage, with a particular focus on creep and hydrogen behavior. The results of this first phase are presented and discussed in this report.

In the second phase, the experimental results will be used to refine and calibrate the existing models. This phase aims to ensure that the refined models provide a more accurate representation of long-term fuel behavior.

2.1 SPIZWURZ Bundle Experiment

2.1.1 Experimental Setup

The QUENCH facility is a unique out-of-pile facility designed for large-scale bundle experiments and has been operated by the KIT since 1997. The QUENCH experimental program was initiated to investigate core degradation and hydrogen generation rates during a reflood of an overheated uncovered core. Within the SPIZWURZ project, the QUENCH facility was modified to conduct a long-term cooling transient and was later named the LICAS facility. Further details on the QUENCH Program, including its latest updates, are available in /STE 25/.

The test section of the LICAS facility is shown in Fig. 2.1. The test bundle consists of 21 electrically heated fuel rod simulators containing non-irradiated zirconium-based cladding tubes, and four corner rods. The bundle cross-section is schematically depicted in Fig. 2.2. The test bundle is surrounded by a zirconium shroud, a ZrO_2 fibre insulation, and a cooling jacket. During the SPIZWURZ bundle experiment, the water temperature inside the cooling jacket was kept constant at a value of around 13 °C to protect from ambient temperature fluctuations and to ensure the targeted cooling rate.

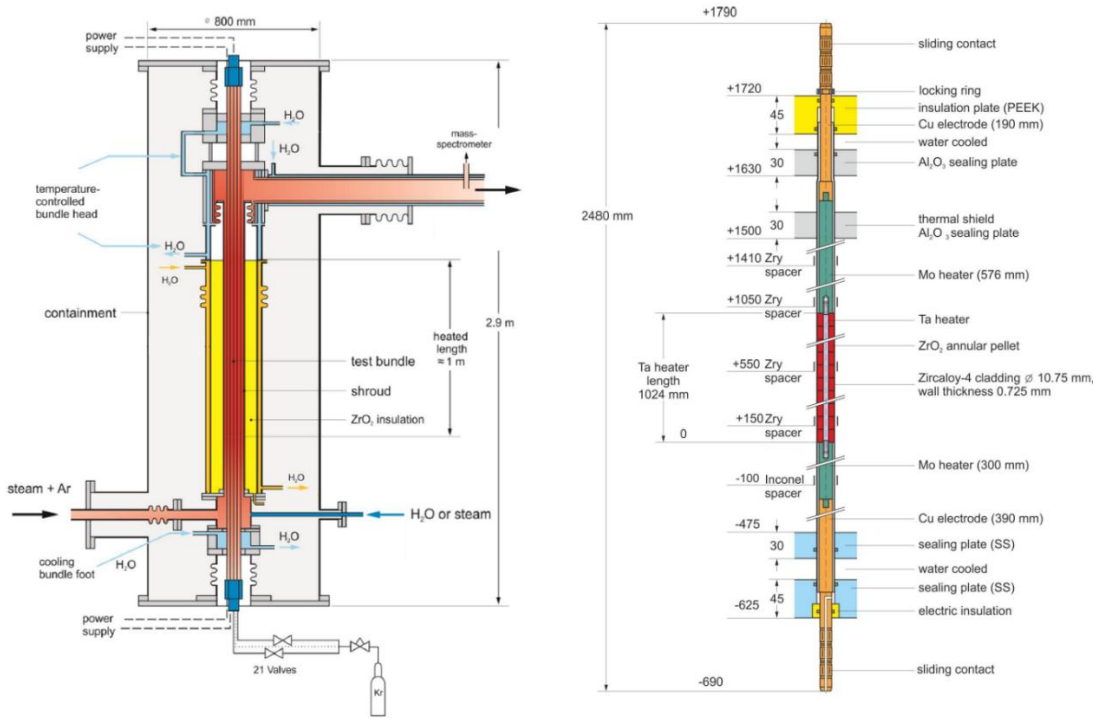

Fig. 2.1 Schematic overview on the LICAS facility

Test section (left), fuel rod simulator (right).

Fuel rod simulators with a length of approximately 2480 mm each are arranged using grid spacers with a pitch of 14.3 mm and are heated electrically. As shown in Fig. 2.1, the midsection of the rod (from 0 mm up to 1024 mm) is heated by a tungsten heater of 4.6 mm diameter, which is surrounded by ZrO_2 annular pellets. Two molybdenum heaters of 9.0 mm diameter are connected in series above and below the tungsten heater, resulting in a total heated length of 1900 mm.

The instrumentation of the LICAS facility allows for control of the rod's internal pressure individually during the experiment. Two different pressurization levels, 103 bar and 142 bar, were applied to the rods in the SPIZWURZ bundle, which correspond to cladding hoop stresses of 66 MPa and 91 MPa, respectively.

Before mounting to the bundle, the cladding tubes were pre-treated with hydrogen in the HoKi furnace at KIT, which was specially designed for this purpose. This furnace allowed to attain uniform temperatures of 450 °C over a length of approximately 1250 mm, which defined the effective hydrogenation region. The hydrogen was supplied from the inner side of the tubes, whereas an oxygen atmosphere was created outside the tubes to

prevent a hydrogen release from the cladding tubes. For the SPIZWURZ bundle experiment, the target hydrogen concentrations were chosen to be 100 wppm and 300 wppm, to lie below and above the solubility limit of the hydrogen at the maximum temperature within the bundle at the beginning of the experiment.

After the loading, the hydrogen content in the claddings was evaluated using the following non-destructive procedure. First, the outer cladding diameter was measured by a laser scanner before and after the hydrogenation to evaluate the growth of the cladding's outer diameter. Then, the hydrogen concentration was measured in several samples using a destructive hot extraction method to establish a correlation between the hydrogen concentration and the growth of the outer diameter. Finally, the hydrogen concentration in the remaining cladding tubes was estimated based on the obtained correlation and the laser scanner measurements of the outer diameter.

It should be noted that the scanner measurements provided only a qualitative representation of the axial hydrogen distribution and did not determine the exact hydrogen concentration along the cladding length. This limitation was particularly relevant for claddings with a target hydrogen content of 100 wppm, where the resulting increase in cladding diameter was approximately 1.7 µm and thus on the order of the scanner measurement uncertainty of ±1 µm. For samples with 300 wppm hydrogen, the resolution was improved, as the corresponding diameter increase was approximately 5.3 µm. More details about the hydrogenation can be found in /STU 23/.

In order to preserve the outer oxide layer of the claddings during the experiment, a mixture of Argon 80 % and Oxygen 20 % was supplied to the space between fuel rod simulators, which created a slight overpressure of 1.1 bar within the shroud.

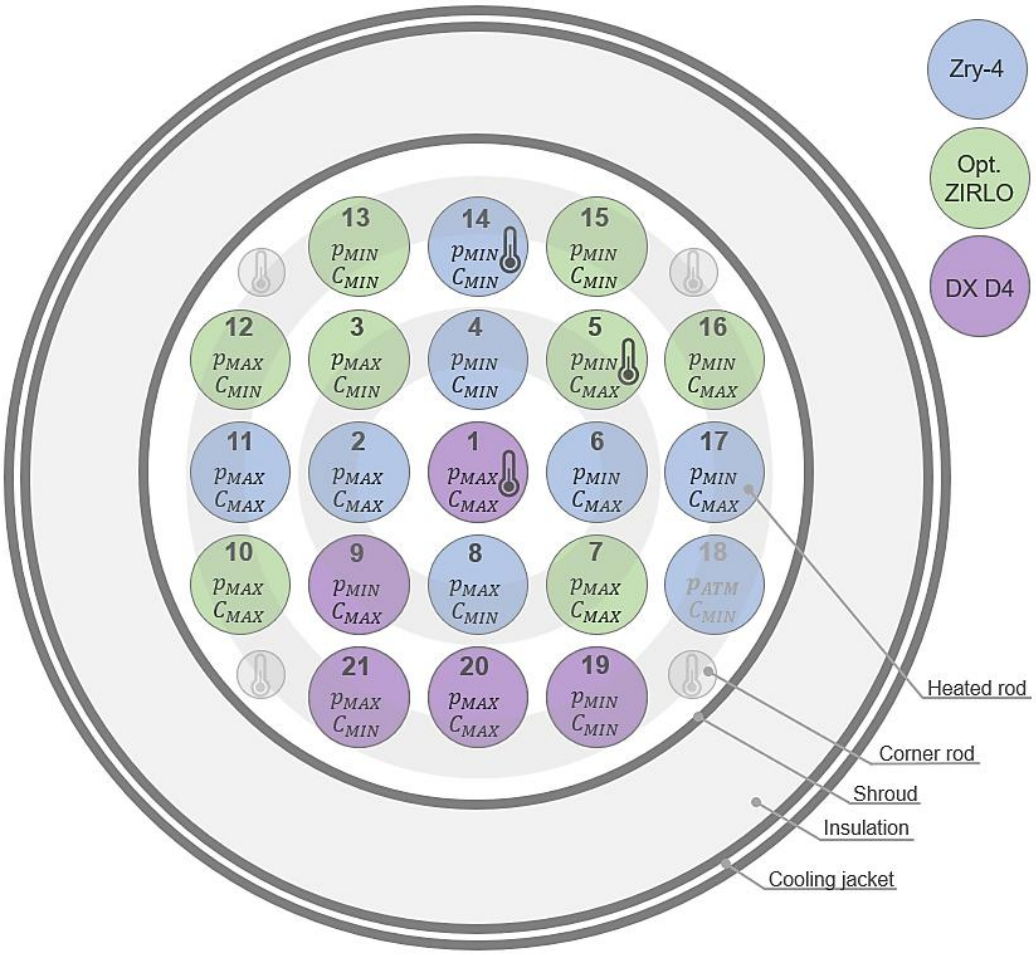

Fig. 2.2 SPIZWURZ test bundle (top view). Thermocouple instrumentation

A scheme of the bundle cross-section is shown in Fig. 2.2. Here, the proportions of the bundle to the other test section components are slightly distorted to better visualize the arrangement of the fuel rods. The classification into central, internal, and peripheral rods is indicated by light grey rings in the sketch of the test bundle.

The SPIZWURZ bundle includes three different zirconium alloys used in Western Europe: Zircaloy-4 (Zry-4), Optimized ZIRLO, and Duplex DX D4, which consists of the Zry-4 bulk material and an outside liner DX with a reduced tin concentration. The allocation of the cladding tubes within the bundle is illustrated in Fig. 2.2 with different colours, whereas the chemical composition of cladding tube materials is given in Tab. 2.1.

Tab. 2.1 Chemical composition of cladding tube materials

Alloying element, wt.%	Cladding tube material			
	Zry-4	Duplex		Opt.ZIRLO
		Zry-4 substrate	DX D4 outer liner	
Sn	1.3	1.5	0.5	0.75
Fe	0.21	0.21	0.5	0.11
Cr	0.1	0.1	0.2	0.005
Nb	0.01	< 0.01	< 0.01	1.0
O	0.13	0.14	0.14	0.12

Tab. 2.2 SPIZWURZ test matrix

Central rod (C), internal rod group (I), and peripheral rod group (P). Internal rod pressure: p_{MIN} =103 bar, p_{MAX} =142 bar; hydrogen concentration: C_{MIN} =100 wppm, C_{MAX} =300 wppm.

Cladding tube material	p_{MIN} and C_{MIN}	p_{MIN} and C_{MAX}	p_{MAX} and C_{MIN}	p_{MAX} and C_{MAX}
Zry-4	I, P	I, P	I	I, P
Opt.ZIRLO	P, P	I, P	I, P	I, P
DX D4	P	I	P	C, P

The target hydrogen concentrations of 100 wppm and 300 wppm are denoted with C_{MIN} and $C_{MAX,}$ respectively. The rods at internal pressures of 103 bar and 142 bar are marked in Fig. 2.2 with p_{MIN} and $p_{MAX,}$ respectively. Due to the leakage of the sealings, the internal pressure in the rod №18 remained at the level of 1.5 bar during the entire experiment. Therefore, only 20 out of 21 rods were considered for the benchmark. The test matrix in Tab. 2.2 summarizes all test conditions considered by the SPIZWURZ bundle.

The design characteristics of the SPIZWURZ bundle experiment are summarized in Tab. 2.3.

Tab. 2.3 Design characteristics of the SPIZWURZ bundle experiment

Bundle	Size	21 heated rods + 4 corner rods
	Effective number of rods	20 heated rods
	Pitch	14.3 mm
Fuel rod simulator	Total length (elevations)	2480 mm (-690 to 1790 mm)
	Rod internal pressure (rods)	
	p_{MAX} =142 bar	1, 2, 3, 7, 8, 10, 11, 12, 20, 21
	p_{MIN} = 103 bar	4, 5, 6, 9, 13, 14, 15, 16, 17, 19
	Total heated gas volume inside the rod	15 cm^3
Cladding tubes	Outside diameter	10.75 mm
	Wall thickness	0.725 mm
	Length (elevations)	2278 mm (-593 to 1685 mm)
	Material (rods)	
	Zircaloy-4	2, 4, 6, 8, 11,14, 17
	Optimized ZIRLO	3, 5, 7, 10, 12, 13, 15, 16
	Duplex DX D4	1, 9, 19, 20, 21
	Hydrogen pre-treatment	
	Effective hydrogenated length (elevations)	≈1250 mm (-18 to 1232mm)
	Target hydrogen concentration (rods)	
	C_{MAX} = 300 wppm	1, 2, 5, 6, 7, 9, 10, 11, 16, 17, 20
	C_{MIN} = 100 wppm	3, 4, 8, 12, 13, 14, 15, 19, 21
	Oxide layer thickness	
	Outer	2.4 µm
	Inner	1.0 µm
Annular pellet	Pellet stack	0 to 1020 mm
	Material	ZrO_2; Y_2O_3-stabilized
	Outer diameter	9.15 mm
	Inner diameter	4.75 mm
	Length	11 mm
	Surface roughness	0.3 µm
Heaters	Total length (elevations)	1900 mm (-300 to 1600 mm)
	Molybdenum heater	
	Length	
	- lower part	300 mm (-300 to 0 mm)
	- upper part	576 mm (1024 to 1600 mm)
	Diameter	
	- after ZrO_2 coating	9 mm
	- prior coating	8.6 mm
	Coating surface roughness	6-12 µm
	Tungsten heater	
	Length	1024 mm (0 to 1024mm)
	Diameter	4.6 mm
	Surface roughness	1.6 µm

2.1.2 Post-Test Cladding Analysis

Upon completion of the bundle experiment, the bundle was dismantled, and all cladding tubes were subjected first to non-destructive outer diameter measurements using a laser scanner. The entire length of each rod was analyzed with a resolution of 1 mm. Measurements at each axial location were taken at 3°radial angular intervals, and the average of these measurements was used to compute the resulting diameter at each specific

axial position. The creep strain was then calculated by comparing the diameter measurements obtained before and after the bundle experiment.

Destructive examinations were performed at a minimum of five axial locations along the cladding length to characterize the local hydrogen concentration and hydride morphology. At each axial location, the upper segment was allocated for hydrogen quantification by hot vacuum gas extraction, while the lower segment was prepared for metallographic analysis.

The local hydrogen concentration was determined by hot vacuum gas extraction from four circumferentially distributed lamellae extracted at 90°intervals. The reported hydrogen concentration represents the arithmetic mean of these four measurements to account for potential circumferential variations.

Metallographic samples were prepared using standard grinding and polishing procedures, followed by appropriate etching to reveal hydride structures. Light optical microscopy (LOM) images were acquired and subsequently analyzed to quantify hydride metrics, including hydride distribution, orientation, and morphology, as described in /KOL 26/.

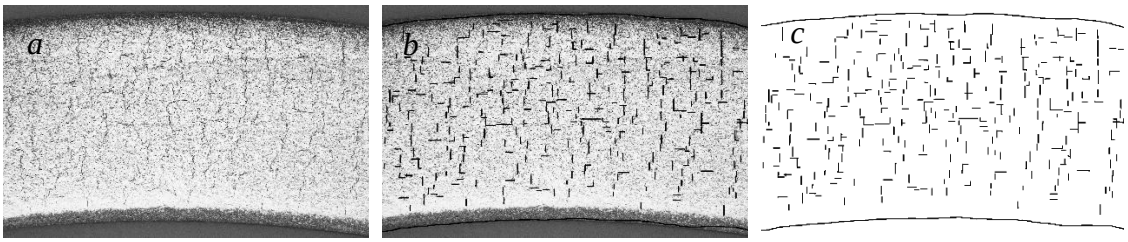

Fig. 2.3 An example of the manual part of the micrograph processing (Rod № 2, bundle elevation 520 mm, angle 0°)

a – original image, b – the original image with outlined hydrides, c – outlined hydrides only (used for further numerical analysis).

Image processing of the metallographic micrographs was carried out in two consecutive steps: a manual pre-processing step and a subsequent numerical analysis step. In the first step, hydrides visible in the micrographs were manually outlined using image analysis software. This procedure improved the contrast of the hydride phase and allowed artefacts associated with mechanical polishing and acid etching of the sample surface to be excluded from further analysis. Without this pre-processing, such artefacts could be

mistakenly interpreted as hydrides during automated evaluation. An example of this procedure is shown in Fig. 2.3.

In accordance with ASTM B811 /SUB 22/, only hydride platelets with a length exceeding 15 µm, or with an extension of more than 15 µm in the secondary direction, were included in the analysis. In the second step, the pre-processed images containing only the outlined hydrides were evaluated using the numerical tool described in /SIM 21/. The tool was used to determine the radial hydride fraction (RHF) and the radial hydride continuous path (RHCP).

Profilometry measurements and subsequent destructive examinations revealed pellet–cladding contact at several axial positions in some of the fuel rods. The observed pellet–cladding interaction (PCI) is attributed to the comparatively higher thermal expansion of the ZrO_2 pellets under the experimental conditions, combined with a slight rod ovality, which resulted in localized mechanical interaction with the cladding. This issue will be addressed further in the discussion of results, including its implications for the comparison between benchmark calculations and experimental observations.

2.2 SPIZWURZ Blind Benchmark

2.2.1 Boundary Conditions

Cladding temperatures

During the SPIZWURZ experiment, the temperatures within the bundle were constantly measured by the thermocouples placed at the outer surface of the fuel rod simulators № 1, № 5, and № 14 and inside of all non-heated corner rods, as illustrated in Fig. 2.2. The three heated rods were instrumented with thermocouples at 14 different axial positions with a 100 mm step starting with the bundle elevation of -50 mm. Additionally, one thermocouple was installed at each bundle elevation at the outer surface of the shroud.

The axial temperature profiles at the beginning (day 0) and at the end (day 250) of the bundle experiment are plotted for fuel rod simulators № 1, № 5, and № 14 in Fig. 2.4.

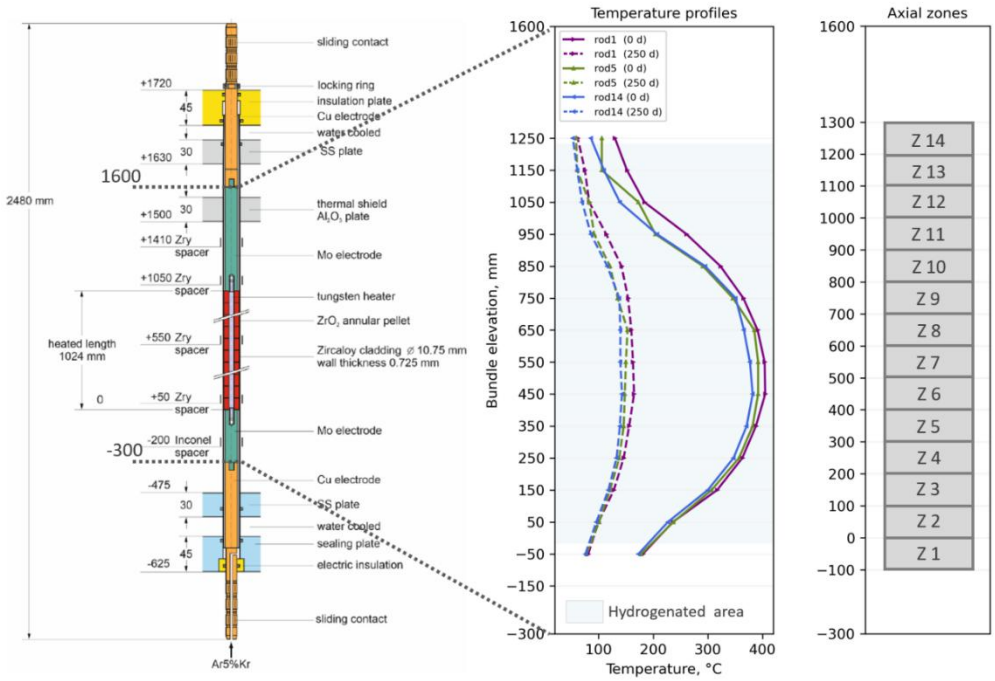

Fig. 2.4 Fuel rod simulator (left). Axial temperature profiles at the beginning and the end of the experiment (middle). Axial zone layout for the benchmark (right)

The suggested partitioning for the benchmark computations is illustrated on the right of Fig. 2.4. The rod region was divided into 14 zones, each 100 mm long, with temperature measurements taken at the midpoint of each zone. Together, these zones fully cover the effective hydrogenated region (the shaded region on the temperature plot in Fig. 2.4).

The maximum temperatures within the bundle were recorded at the central rod at an elevation of 450 mm -550 mm (zones 6 and 7). It decreased from its initial value of around 405 °C down to 165 °C within 250 days, with an average slope of 0.94 °C/d. The temperatures in the central region of the cladding of the central rod (№ 1), an internal rod (№ 5), and a peripheral rod (№ 14) are plotted in Fig. 2.5.

As illustrated in Fig. 2.5, four electrical power failures occurred during the experiment, resulting in rapid cooling of the rods. Apart from these unplanned events, the temperature was decreased in a controlled, stepwise manner, with maximum gradients of up to 6 °C/h during the scheduled cooling phases. However, unintended operational interventions associated with manual power adjustments produced substantially higher localized cooling rates of up to 40 °C/h. Even more pronounced effects were observed during accidental complete power outages, where cooling rates reached as high as 160 °C/h at individual measurement locations.

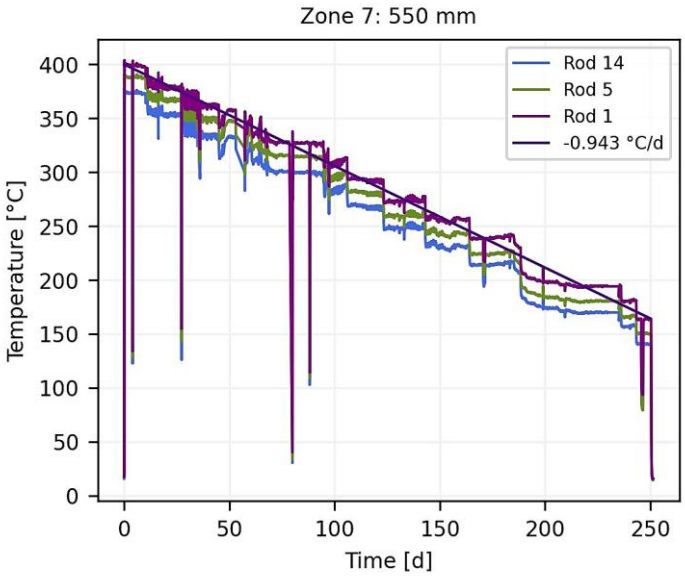

Fig. 2.5 Temperature evolution in the central part of the cladding over the 250-day SPIZWURZ Bundle Experiment

Central rod (№1) internal rod (№5), and peripheral rod (№14).

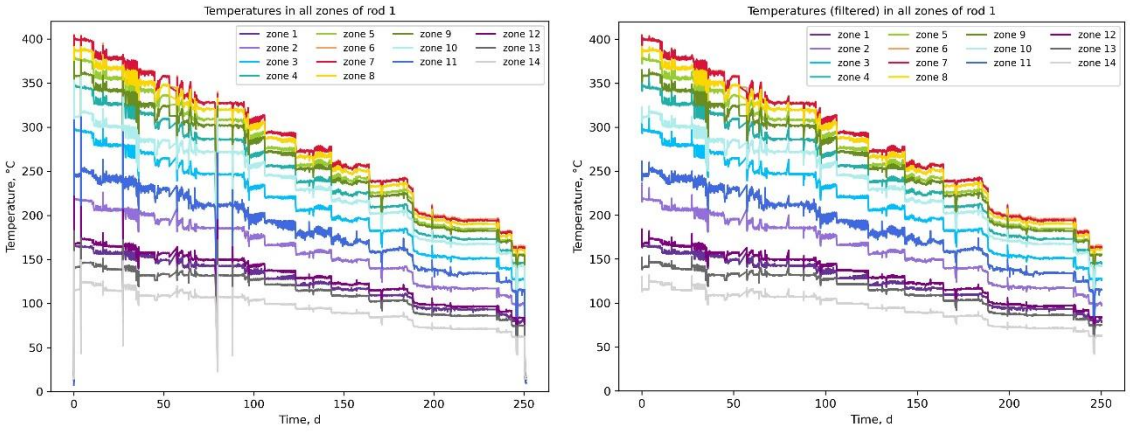

Fig. 2.6 Cladding temperatures during the bundle experiment in all 14 zones of the central rod (left: original data, right: filtered data)

The temperature data recorded by the thermocouples on the central rod (Rod № 1) were used as the temperature boundary condition for the benchmark calculations. Assuming radial symmetry within the bundle for calculation purposes, the temperature recordings from fuel rod simulator № 5 were used to define the boundary conditions for the eight internal rods (Rods № 2–№ 9), while the data from fuel rod simulator № 14 were used for the simulation of the eleven peripheral rods (Rods № 10–№ 21).

The cladding temperatures recorded in all 14 zones of the central rod are presented on the left side of Fig. 2.6, while the temperature data from the remaining rods are provided in Appendix 0. From the *filtered* temperature histories shown on the right side of Fig. 2.6, those power shortage events have been removed. For the benchmark calculations, the use of the original *unfiltered* data was the preferred option, although the filtered data could be used to avoid potential numerical issues arising from the transient cooling of the rods.

Rod internal pressure

The pressure within each rod was controlled individually. Small leaks required periodic refilling of 7 out of the 20 rods, and the replacement of sealing rings in 6 rods caused brief depressurization events, visible in the pressure recordings as abrupt pressure drops on the left side of Fig. 2.7. These events are not related to the electrical power failures noted earlier and have also been removed from the filtered data shown on the right side of the figure. For the benchmark calculations, the original unfiltered pressure data are preferred, although the filtered data could be used to avoid potential numerical issues from the abrupt drops.

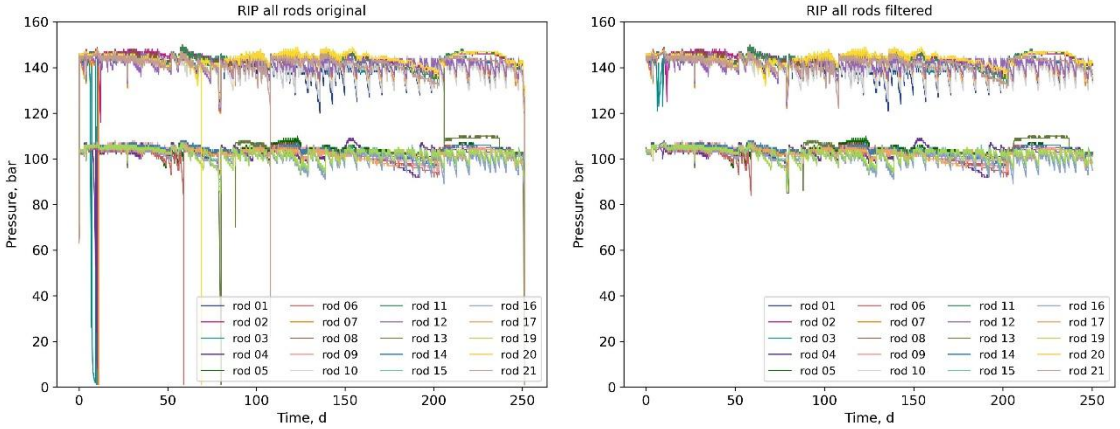

Fig. 2.7 Rod internal pressure in all 21 fuel rod simulators during the bundle experiment (left: original data, right: filtered data)

Hydrogen concentration

The initial hydrogen content of all cladding tubes was quantified from the diameter increase measured after hydrogen charging, using laser scanner measurements as described in Section 2.1.1. The resulting axial hydrogen concentration profiles at the start

of the bundle test are shown in Fig. 2.8 for rods № 1 and № 5 as representative examples; the corresponding axial distributions for all rods are compiled in Appendix B.

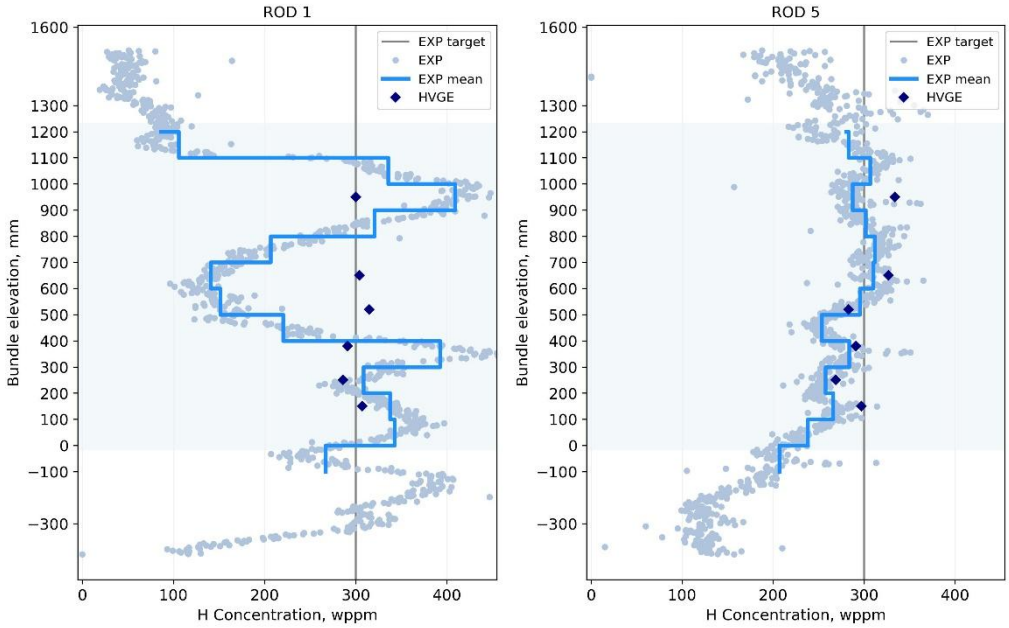

Fig. 2.8 Axial hydrogen distribution in the cladding of the fuel rod simulator № 1 (left) and № 5 (right)

Although the target hydrogen concentration for both claddings was 300 wppm as marked by the grey vertical lines in Fig. 2.8, the measured concentrations exhibited rod-specific axial variations. For the benchmark calculations, the hydrogen content was averaged over the predefined axial zones, as indicated by the solid blue lines in Fig. 2.8.

Post-test cladding analysis using hot vacuum gas extraction (HVGE), as shown by dark blue diamonds in Fig. 2.8, revealed deviations from the estimated values and indicated a more uniform axial hydrogen distribution.

The uncertainty in the pre-test estimates arises primarily from measurement limitations, since the diameter increase corresponding to 100 wppm of hydrogen uptake is comparable to the measurement accuracy, as explained in Section 2.1.1. Furthermore, the correlation between diameter change and hydrogen uptake was established using a limited number of samples subjected to destructive analysis after hydrogen charging and prior to the bundle test. The hydrogen concentrations determined at the conclusion of the experiment via hot vacuum gas extraction are considered more representative than the initial diameter-based estimates, as only minor axial hydrogen diffusion is expected at the temperatures investigated.

The hot vacuum gas extraction measurements were performed after completion of the bundle test and were therefore not available at the time the benchmark calculations were carried out. Consequently, the benchmark simulations relied solely on the estimated hydrogen concentrations. This introduces uncertainty in the initial hydrogen content that must be considered when comparing benchmark results with experimental observations.

2.2.2 Scope of the Benchmark

The benchmark was conducted in accordance with the setup described in the benchmark specification /REZ 24/. Distributed experimental data included temperature and pressure measurements recorded during the experiment, as well as the estimation of hydrogen content along the cladding length, as detailed in Section 2.1.1.

Benchmark participants were requested to report, for each fuel rod in the test bundle, the hydrogen concentration, hydride concentration and orientation (including radial and circumferential distribution), and cladding strains (including creep strain and total strain components).

All results were to be submitted in the data format defined in the benchmark specification to ensure consistency and comparability among participants.

The submitted results were subsequently compared to the experimentally measured creep strain and radial hydride fractions derived from light optical microscopy analyses. The evaluation assessed the participants' ability to reproduce both the magnitude and the axial distribution of creep deformation, as well as the measured fraction of radially oriented hydrides. These results are presented below in Section 3.

3 SPIZWURZ Blind Benchmark Results

The blind phase of the SPIZWURZ Benchmark began in April 2024, involving a total of 11 contributions by 10 organizations from 7 countries. The following organizations participated in the benchmark:

1. AXPO Power AG (AXPO), Switzerland
2. Centre for Energy, Environmental and Technological Research (CIEMAT), Spain
3. National Atomic Energy Commission (CNEA), Argentina
4. Électricité de France SA (EDF), France
5. Framatome GmbH, Germany
6. Gesellschaft für Anlagen- und Reaktorsicherheit gGmbH (GRS), Germany
7. Karlsruhe Institute of Technology (KIT), Germany
8. Paul Scherrer Institut (PSI), Switzerland
9. Seoul National University (SNU), South Korea
10. Nuclear Research Institute ÚJV Řež (UJV), Czech Republic

The following sections present the results of the benchmark exercise, including comparisons between submitted predictions and experimental reference data. Section 3.1 provides a detailed summary of the benchmark outcomes related to cladding creep behavior, while Section 3.2 focuses on hydrogen behavior in the cladding.

Initial results from the benchmark exercise were presented during the 21st International Symposium on Zirconium in the Nuclear Industry /GRO 25/.

3.1 Creep behavior

This section of the benchmark addresses the creep behavior of the fuel rod cladding during a long-term cooling transient. It opens with an overview of the participating organizations and their respective modeling approaches, followed by a presentation of the benchmark results. The analysis then compares the predicted creep responses with experimental data, highlighting overall trends, areas of agreement, and key discrepancies among the different calculations.

3.1.1 Participants and Modeling Approaches

Eight organizations submitted a total of nine contributions to the benchmark addressing creep behavior. The computational tools employed by the participants are summarized below, with the organizations listed in alphabetical order.

AXPO

AXPO used the 1.5D in-house code DSTL to simulate the behavior of a fuel rod during dry storage and to compute creep strains of Zry-4 and DX D4 claddings. For the modeling of DX D4, the correlation proposed by Cappelaere et al. /CAP 12/ was applied with a custom parameterization, while the generic correlation developed by Spilker et al. /SPI 97/ was used for Zry-4 rods. The effect of hydrogen on the creep rate of Zircaloy was accounted for based on the study by Mallipudi et al. /MAL 12/.

CIEMAT

The cladding creep strain was evaluated exclusively for the Zry-4 rods using the correlation developed by CIEMAT, which is based on a database containing Zry-4 material data /FER 11/. This correlation is implemented in FRAPCON-xt, the dry storage extension of the fuel performance code FRAPCON /FER 15/.

CNEA

DIONISIO is a fuel performance code developed at the Codes and Models Section of CNEA. It is designed to simulate the behavior of nuclear fuels under irradiation during normal reactor operation and under loss-of-coolant accident conditions. The code is applicable to fuel rods from nuclear power plants (PWR, BWR, PHWR, and SMR) as well as to plate-type fuels used in research reactors. In addition, DIONISIO includes a dedicated module for the simulation of out-of-pile experiments, which was employed for the SPIZWURZ Benchmark calculations.

Creep calculations were carried out using filtered input in combination with the CREPR model implemented in FRAPCON-4.0 /GEE 15/. The CREPR formulation is based on the model proposed by Limbäck and Andersson /LIM 96/. Model parameters corresponding to stress-relief-annealed cladding were adopted for Zry-4 and DX D4. For Opt.ZIRLO, the same parameter set was applied with a reduction factor of 0.8 /SAB 94/.

EDF

EDF carried out simulations using the SICRAC code /EL 24/, a 1.5D numerical tool specifically developed to calculate cladding creep under back-end conditions. The creep behavior of Zry-4 and Opt.ZIRLO claddings was modeled using the correlations proposed by Cappelaere et al. /CAP 12/.

Framatome

Framatome employed CSAS, an in-house tool for evaluating cladding stress and strain under dry storage conditions. For the benchmark, a specialized R&D version of the code was employed to simulate the creep behavior of Zry-4 and DX D4 claddings, using filtered input data and a model calibrated against Framatome creep data.

GRS

GRS performed the benchmark calculations using the 1.5D in-house code TESPA-ROD, which is capable of simulating fuel rod behavior under normal operation, a range of accident scenarios, and has recently been applied to long-term storage scenarios /SAP 25/. The creep strains of Zry-4 and DX D4 rods were calculated using the CIEMAT correlation /FER 11/. For Opt.ZIRLO claddings, this correlation was adapted to reproduce the experimental creep data reported for unirradiated Opt.ZIRLO /AND 20/.

PSI

PSI evaluated the mechanical behavior of the fuel rods using two different codes: Falcon V1.5 /YAG 15/ and OFFBEAT /SCO 20/. Falcon is a 2D finite element code co-developed by the Electric Power Research Institute and PSI, capable of modeling BWR and PWR rod designs under a variety of scenarios. Creep behavior under dry storage conditions was simulated using the Bouffioux model /BOU 05/. All rods were treated as Zry-4, as thermo-mechanical parameters for Opt.ZIRLO and DX D4 are not available in the version of Falcon used.

OFFBEAT is a multi-dimensional thermomechanical fuel performance code, co-developed by EPFL and PSI, based on the OpenFOAM platform. All rods were modeled as Zry-4, and creep was computed using the model by Limbäck and Andersson /LIM 96/. The submitted creep strain corresponds to the volume-averaged hoop component of the

strain tensor for each axial zone. Full input data were used, except for DX D4 rods, which were simulated using filtered data.

UJV

UJV contributed to the benchmark calculations using TRANSURANUS, a fuel performance code developed by the Joint Research Centre and widely used by research centers, nuclear safety authorities, universities, and industry partners /LAS 92/. The code supports thermal and mechanical analyses of fuel rods in BWR, PWR, and VVER reactors under normal, off-normal, and accident conditions. Creep of DX D4 and Zry-4 rods was calculated using the standard Zircaloy TRANSURANUS model, while an internal UJV creep model was applied for Opt.ZIRLO claddings.

3.1.2 Benchmark Results

Key factors to consider when comparing creep deformation of different rods in the bundle include their position within the bundle, the pressure evolution during the test, and the hydrogen content. To enable a clear comparison between the rods, only one parameter is varied at a time while all other conditions are held constant.

As discussed in Section 2.2.1, post-test examinations of several bundle cladding tubes revealed significant discrepancies between the initially estimated hydrogen contents used as input for the benchmark calculations and the concentrations measured by hot vacuum extraction. These discrepancies introduce additional uncertainty in the comparison between benchmark predictions and experimental observations, particularly when evaluating the capability of the codes to simulate hydride reorientation. However, this issue poses only limited impact on the creep assessment, since nearly all models applied in the present study do not explicitly account for hydrogen effects in their creep correlations.

When comparing experimental results with simulations, it is important to account for the pellet-cladding interaction, which is particularly pronounced in rods № 6, № 8, and № 12.

In the axial creep profiles shown below, the y-axis corresponds to the axial position (bundle elevation), while the x-axis represents the creep strain. Experimental data are displayed in black, whereas numerical results are shown in color and labeled according to

the contributing organization. For clarity, ‘PSI-F’ and ‘PSI-O’ refer to PSI results obtained with the Falcon and OFFBEAT codes, respectively.

Zry-4 Cladding

The maximum creep was observed in rods subjected to higher hoop stress and positioned in the hotter regions of the bundle. For Zry-4 claddings, these correspond to rods № 2 and № 8, both located in the inner rod ring and pressurized at their respective maximum pressures (144.5 bar and 144.1 bar). Using the thin-wall approximation based on the inner diameter, this results in a hoop stress of approximately 92.5 MPa. At the beginning of the experiment, the temperature in the central part of the internal rods reached a maximum of 392 °C.

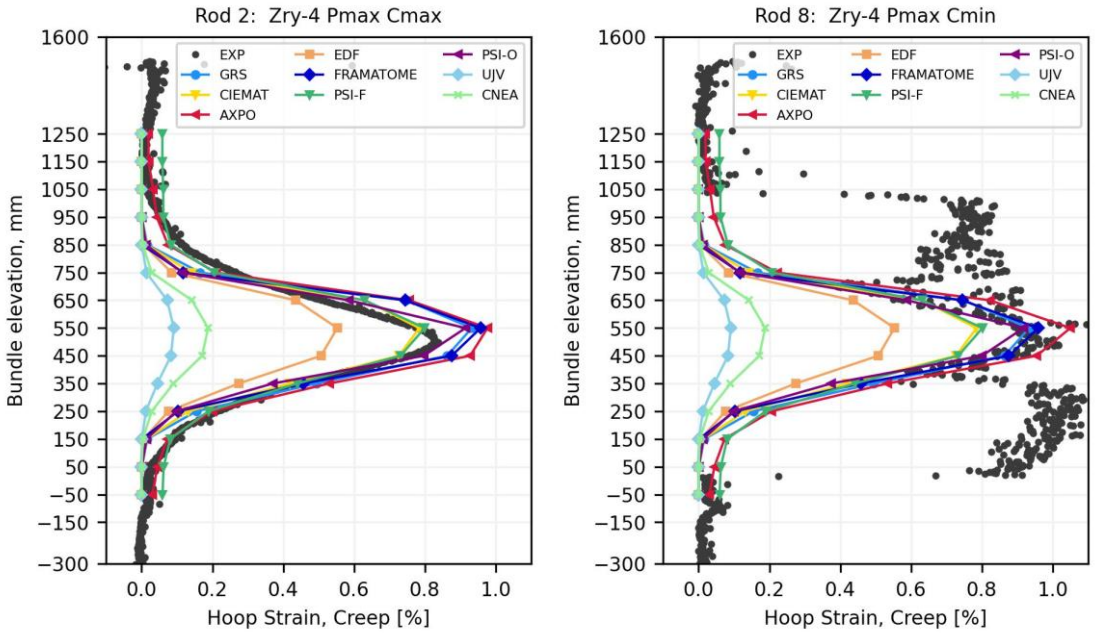

Fig. 3.1 Axial creep profiles. Left: Rod № 2 (Zry-4, P_{max}, C_{max}, internal). Right: Rod № 8 (Zry-4, P_{max}, C_{min}, internal)

The axial distribution of creep deformation reflects the bell-shaped temperature profile, with a maximum value of 0.83 % at a bundle elevation of approximately 500 mm in the rod № 2, see Fig. 3.1. Toward both the lower and upper ends of the rod, the creep strain decreases significantly, approaching near-zero values outside the central zone.

The experimental data for rod № 8 indicate a similar maximum creep strain; however, a pronounced scatter is observed over the entire axial range, which is attributed to pellet–

cladding interaction. During sample preparation for metallographic investigations, the pellets in the central region detached easily, whereas those near the rod ends remained trapped within the cladding.

Fig. 3.2 presents a light optical microscopy image of rod № 8 at a bundle elevation of 950 mm, where the presence of an annular pellet and its center hole is clearly visible. In addition, the profilometry measurements of this rod reveal a distinct pellet pattern, characterized by a periodic drop in the measured diameter approximately every 11 mm, corresponding to the pellet height.

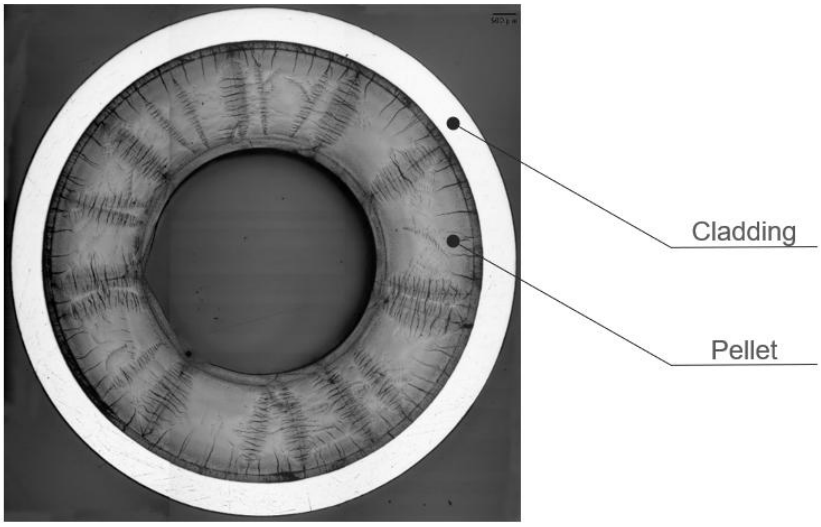

Fig. 3.2 LOM image of rod № 8 (Zry-4, P_{max}, C_{min}, internal) at 950 mm elevation

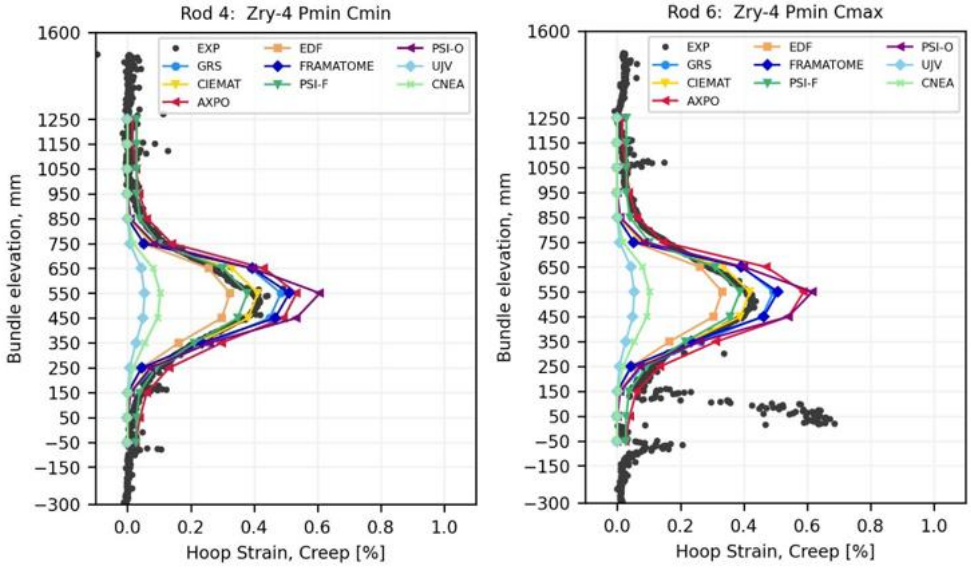

Fig. 3.3 Axial creep profiles. Left: Rod № 4 (Zry-4, P_{min}, C_{min}, internal). Right: Rod № 8 (Zry-4, P_{min}, C_{max}, internal)

Although the quantitative impact of the pellet effect on the measured creep strain cannot be determined precisely, the influence is considered significant. Therefore, rod № 8 is excluded from further evaluation and comparison.

The internal rods № 4 and № 6 pressurized at P_{min} (hoop stresses of approximately 66 MPa) exhibit creep strains roughly half those of rod № 2, with similar values observed for both high and low hydrogen content, as can be seen in Fig. 3.3. Although PCI occurs at the rod ends, the central region shows no pellet pattern, suggesting only a minor influence on creep in that area.

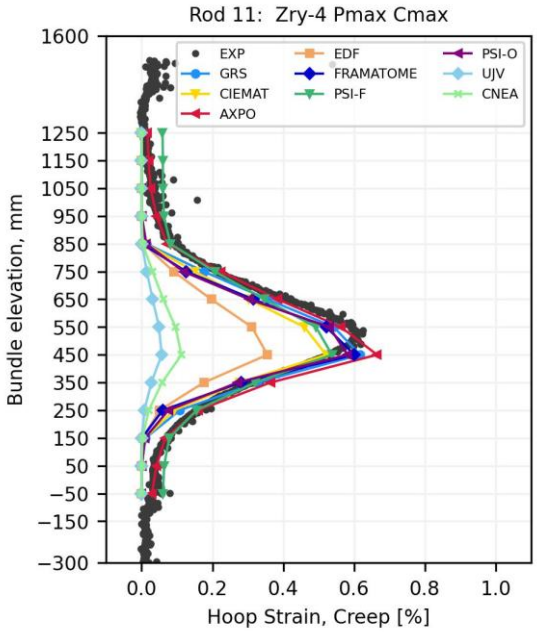

Fig. 3.4 Axial creep profile. Rod № 11 (Zry-4, P_{max}, C_{max}, peripheral)

At the start of the experiment, the maximum temperature in the peripheral rods was about 10 °C lower than in the internal rod ring. The creep profile shown in Fig. 3.4 illustrates the axial distribution of hoop strain for rod № 11. Compared to the internal rod № 2, № 11 located at the bundle periphery exhibits approximately 27 % lower creep deformation, highlighting the influence of temperature on creep.

Data for a second peripheral rod at P_{max} are not available, as rod № 18 remained unpressurized throughout the experiment. Nevertheless, the measurements from this rod can be used as a reference.

Two peripheral Zry-4 rods shown in Fig. 3.5, № 14 and № 17, both at Pmin, exhibit maximum creep strains of 0.27 % and 0.33 %, respectively. These values are 34 % and 23 % lower than those of rods № 4 and № 6, located in the internal ring and having otherwise similar parameters. While most Zry-4 rods show no significant differences in creep between low and high hydrogen content, rod № 17 has 18 % higher maximum creep strains compared to rod № 14, which may also be due to an 8 °C uncertainty in the radial temperature distribution within the bundle. Consistent with the observations for the internal rods, the higher pressurization of rod № 11 compared to № 17 results in approximately 1.9 times greater creep strain.

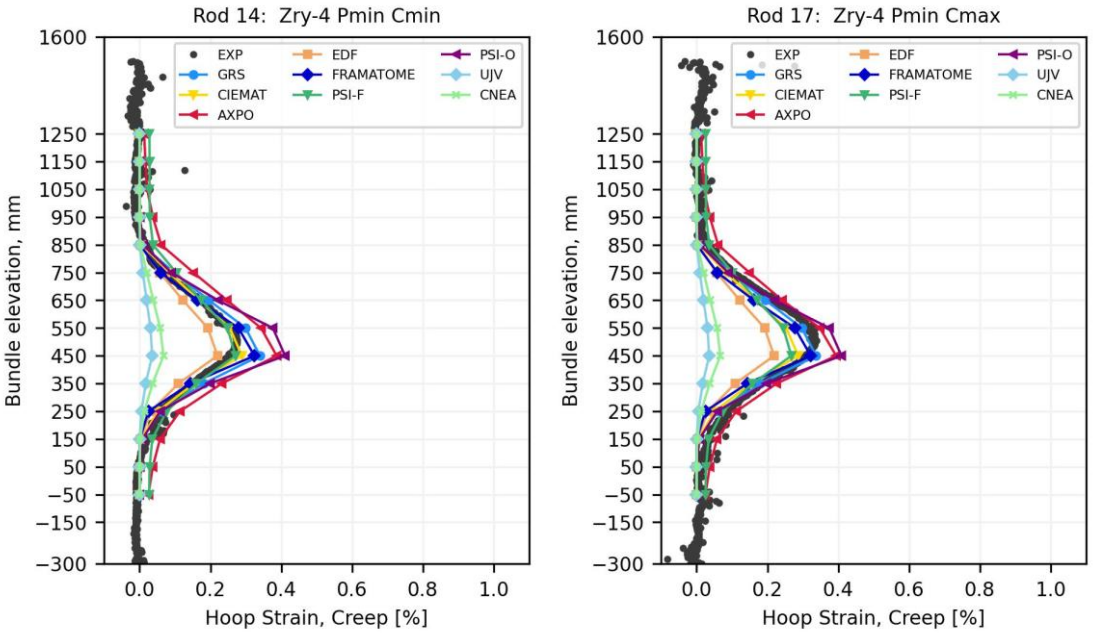

Fig. 3.5 Axial creep profiles. Left: Rod № 14 (Zry-4, P_{min}, C_{min}, peripheral). Right: Rod № 17 (Zry-4, P_{min}, C_{max}, peripheral)

Overall, most of the submitted results showed good agreement with the measured creep values, indicating that the existing codes are generally effective in reproducing the creep strains of Zry-4 claddings during long-term cooling. The bell-shaped axial profiles were generally well reproduced by the models. However, creep strains in the colder rod end regions, where the temperature does not exceed 300 °C, are underestimated by the majority of benchmark participants. This discrepancy is likely related to the limited availability of experimental data in this temperature range for model calibration and validation.

The lower creep values reported by the benchmark participants CNEA and UJV can be attributed to the use of creep models derived for in-reactor conditions, which tend to underestimate creep behavior under dry storage conditions.

DX D4 Cladding

A comparison between the DX D4 rod № 9 and the Zry-4 rod № 6 from the internal rod ring, as well as between the peripheral rod pairs № 20 and № 11 and № 19 and № 14, which were subjected to identical test conditions except for the cladding material, indicates nearly identical creep behavior. Therefore, the approach adopted by most benchmark participants of applying the same creep models to both Zry-4 and DX D4 claddings is well supported by the findings of the bundle experiment.

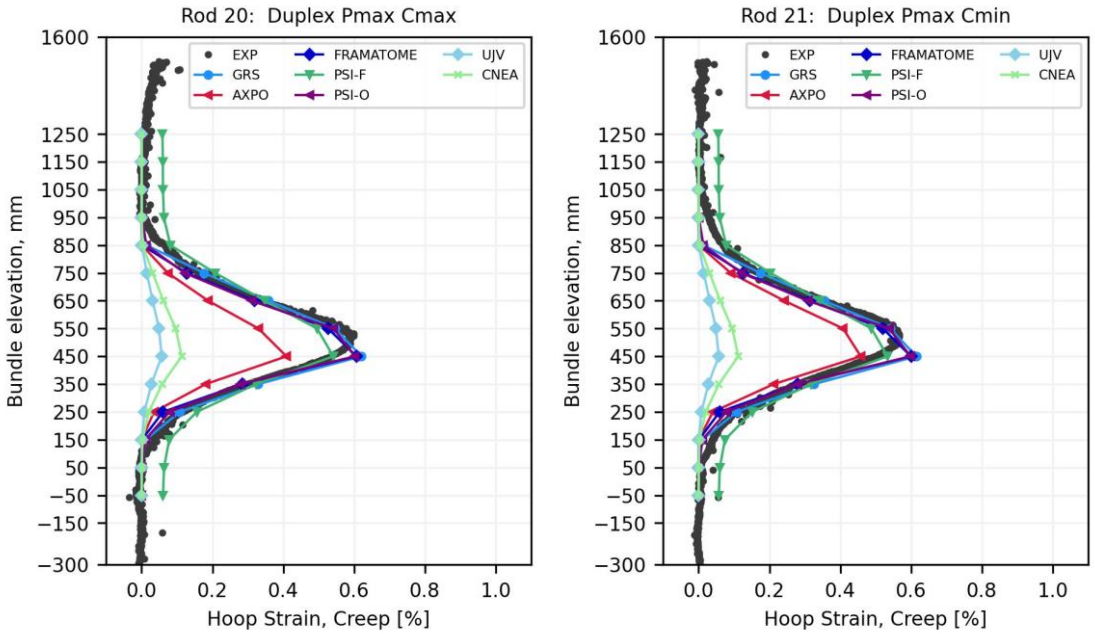

Fig. 3.6 Axial creep profiles. Left: Rod № 20 (DX D4, P_{max}, C_{max}, peripheral). Right: Rod № 17 (DX D4, P_{max}, C_{min}, peripheral)

The comparison of the DX D4 peripheral rods № 20 and № 21 in Fig. 3.6 shows very similar creep behavior for rods with different hydrogen contents. The creep strains of rod № 21 (right in Fig. 3.6), pressurized at Pmax, are approximately twice as high as those measured for rod № 19, pressurized at Pmin (right in Fig. 3.7). These findings are consistent with the trends observed for the Zry-4 rods.

As shown previously, differences in hydrogen content do not significantly influence the creep behavior of Zry-4 and DX D4 rods, which allows for a comparison between the internal rod № 9 and the peripheral rod № 19 despite their different hydrogen levels in Fig. 3.7. For this pair, the 10–15 °C higher temperatures lead to a 41 % increase in creep strain, which is larger than the corresponding differences observed for the Zry-4 rods.

This deviation could be related to the difference in hydrogen content; however, it is more likely attributable to the radial temperature uncertainty within the bundle.

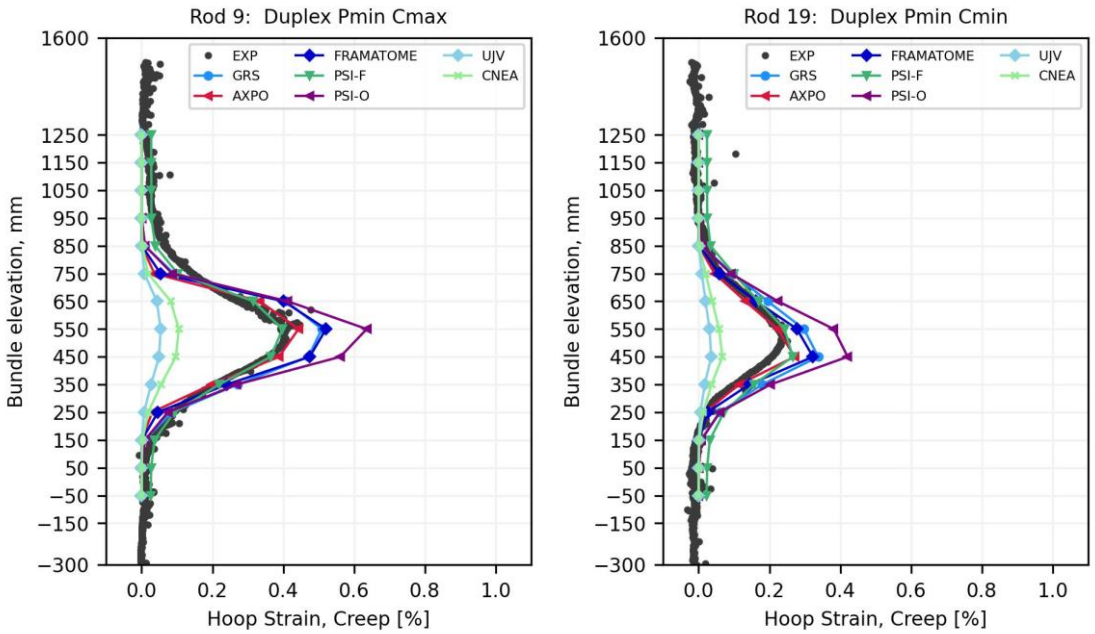

Fig. 3.7 Axial creep profiles. Left: Rod № 9 (DX D4, P_{min}, C_{max}, internal). Right: Rod № 19 (DX D4, P_{min}, C_{min}, peripheral)

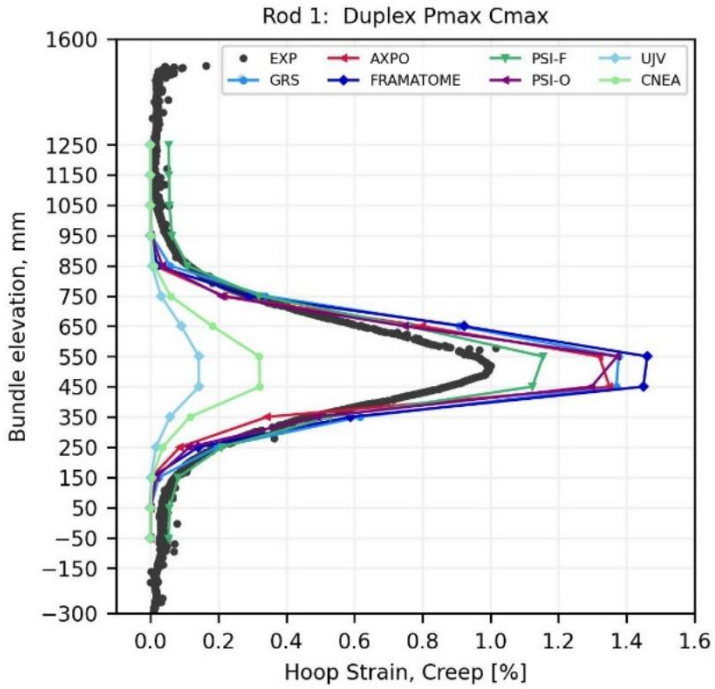

Fig. 3.8 Axial creep profile. Rod № 1 (DX D4, P_{max}, C_{max}, central)

The temperatures in the central rod are up to 30 °C higher than those in the peripheral rods, and correspondingly, the creep deformation of rod №1 is the highest among the Duplex rods, see Fig. 3.8, being approximately 40 % greater than that of rod № 20 (left in Fig. 3.6). This behavior is consistent with the trends observed for the Zry-4 rods.

Overall, the findings from the bundle experiment provide strong support for the approach adopted by most benchmark participants, namely the application of the same creep models to both Zry-4 and DX D4 claddings.

Opt.ZIRLO Cladding

Compared to Zry-4 and DX D4 claddings, the Opt.ZIRLO rods exhibited approximately two to four times higher creep deformation in the bundle test. The largest difference was observed for rods at Cmax and Pmax, Zry-4 rod № 2 (Fig. 3.1, left side) and Opt.ZIRLO rod № 7 (Fig. 3.9), with rod № 7 reaching a maximum creep strain of 3.32 % at the center of the rod, compared to 0.83 % for rod № 2. Consequently, the x-axis for the axial creep plots of Opt.ZIRLO rods was extended to accommodate the higher creep strains.

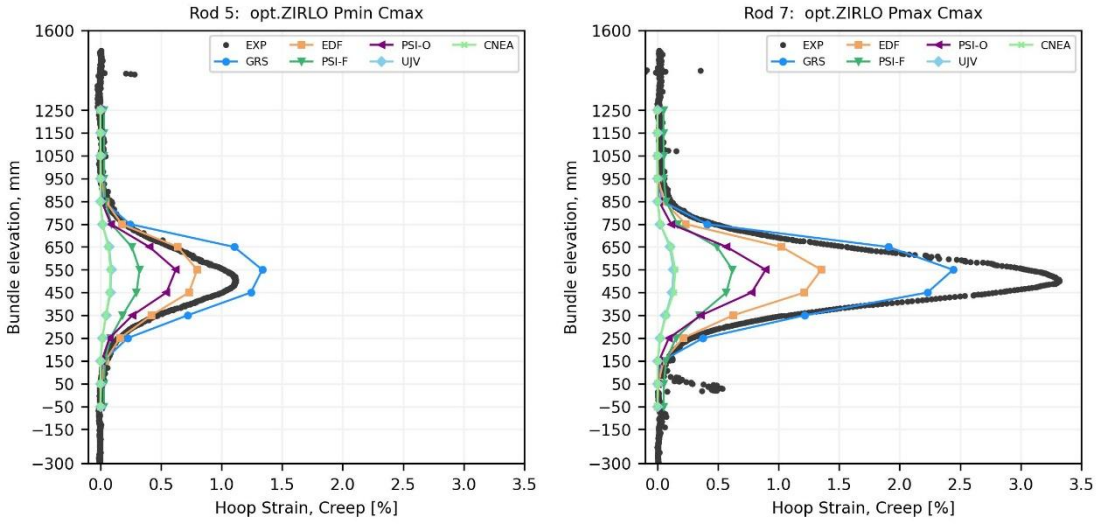

Fig. 3.9 Axial creep profiles. Left: Rod № 5 (Opt.ZIRLO, P_{min}, C_{max}, internal). Right: Rod № 7 (Opt.ZIRLO, P_{max}, C_{max}, internal)

The effect of pressure also appears to be more pronounced for Opt.ZIRLO claddings. For the internal rods shown in Fig. 3.9, the creep strains of rod № 7 at P_{max} are nearly three times higher than those of rod № 5 at P_{min}. For the peripheral rods № 10 and № 16 in Fig. 3.10, this factor is approximately 2.5. In comparison, the corresponding factor for Zry-4 rods was around 2.

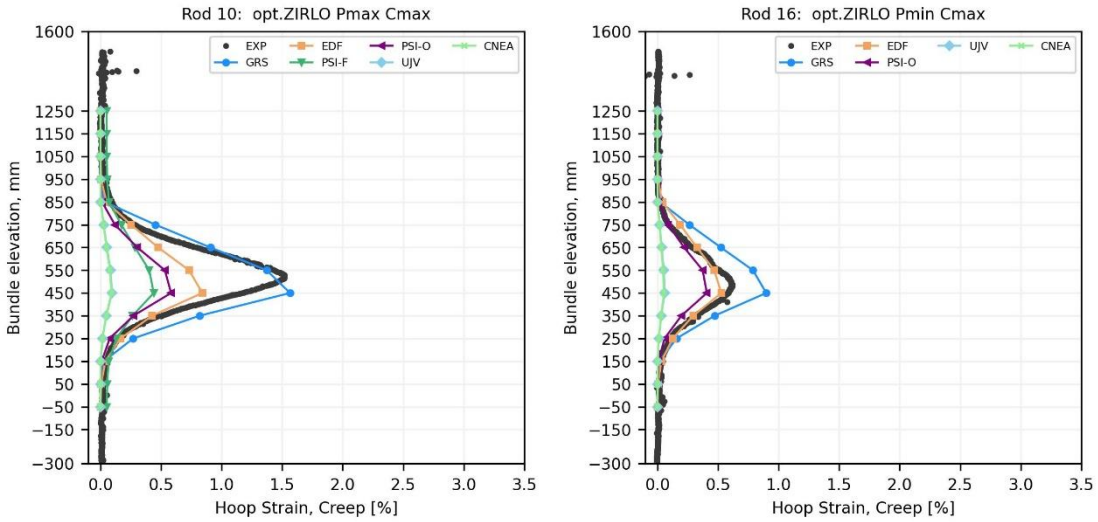

Fig. 3.10 Axial creep profiles. Left: Rod № 10 (Opt.ZIRLO, P_{max}, C_{max}, peripheral). Right: Rod № 16 (Opt.ZIRLO, P_{min}, C_{max}, peripheral)

The 10–15 °C temperature difference between internal and peripheral rods has a more pronounced effect on Opt.ZIRLO claddings compared to Zry-4 rods, where the creep of internal rods did not exceed 1.5 times that of the peripheral rods. For Opt.ZIRLO rods at P_{max}, the maximum creep strain of the internal rod № 7 (Fig. 3.9, right side) is 2.2 times higher than that of the peripheral rod № 10 (Fig. 3.10, left side). At P_{min}, the creep strain of rod № 5 (Fig. 3.9, left side) is 1.8 times greater than that of rod № 16 (Fig. 3.10, right side).

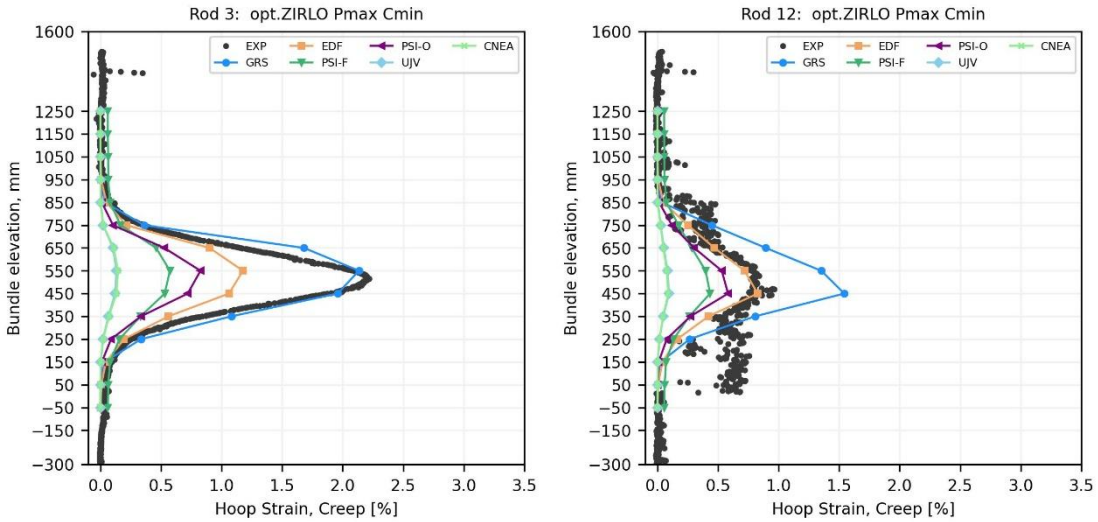

Fig. 3.11 Axial creep profiles. Left: Rod № 3 (Opt.ZIRLO, P_{max}, C_{min}, internal). Right: Rod № 12 (Opt.ZIRLO, P_{max}, C_{min}, peripheral)

The analysis of the temperature difference effects between rods № 3 and № 12, for which the resulting axial creep profiles are shown in Fig. 3.11, is complicated by two factors. First, rod № 3 was not pressurized at the start of the experiment, between days 7 and 10, due to sealing issues, and would therefore be expected to exhibit higher creep if normal pressurization level had been maintained. Second, rod № 12 was affected by pellet-cladding interaction, the impact of which cannot be precisely quantified.

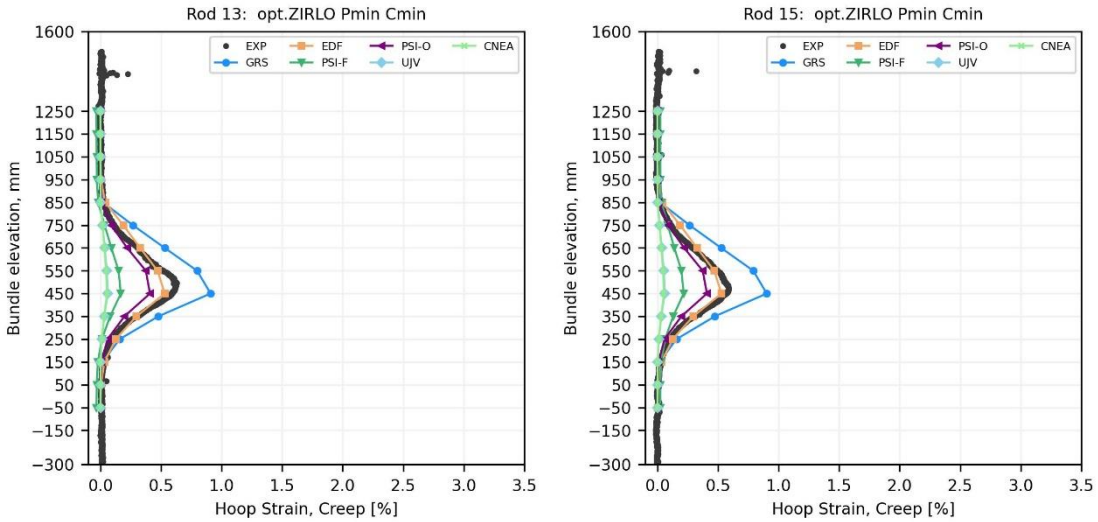

Fig. 3.12 Axial creep profiles. Left: Rod № 13 (Opt.ZIRLO, P_{min}, C_{min}, peripheral). Right: Rod № 15 (Opt.ZIRLO, P_{min}, C_{min}, peripheral)

In the test bundle, two peripheral Opt.ZIRLO rods - № 13 and № 15 in Fig. 3.12 - were subjected to identical boundary conditions P_{min} and C_{min}. As expected, these rods exhibit very similar creep behavior.

The comparison of creep strains between rods № 7 and № 3, as well as between rods № 10 and № 12, suggests that higher hydrogen content may promote creep in Opt.ZIRLO claddings. However, this analysis is complicated by pellet–cladding interaction in rod № 12 and sealing issues in rod № 3, and further experiments are required to confirm this effect before it could be incorporated into the models.

In general, the creep models tend to underestimate the deformation of Opt.ZIRLO cladding, particularly at higher stresses. The differences in creep behavior between Opt.ZIRLO and Zry-4 observed in the experiment indicate that creep models developed for Zry-4 cannot be directly applied to Opt.ZIRLO.

3.2 Hydrogen behavior

This part of the benchmark focuses on hydrogen behavior in the fuel rod cladding during a long-term cooling transient. The discussion begins with an overview of the participating organizations and their modeling approaches, followed by a presentation of the benchmark results and an assessment of their agreement with experimental data, highlighting trends and discrepancies.

3.2.1 Participants and Modeling Approaches

Eight organizations submitted a total of nine contributions for the benchmark addressing hydrogen behavior. The computational tools employed by the participants are summarized below, with the organizations listed in alphabetical order.

AXPO

To simulate hydrogen behavior in Zry-4 and DX D4 claddings, AXPO employed the in-house code HyReL, which models both hydrogen diffusion and hydride precipitation/dissolution. A two-dimensional approach was implemented to capture radial and axial diffusion, allowing for the analysis of duplex and liner claddings.

The Hydrogen Nucleation, Growth, and Dissolution (HNGD) model developed by Lacroix /LAC 19/ was applied for the benchmark calculations. Hydride orientation was determined using the EPRI model /RAS 05/, which was extended with a structural factor accounting for the presence of pre-existing hydrides in the cladding wall.

The following material properties were used in the simulations: hydrogen diffusion coefficient from /ZHA 17/, thermo-diffusion coefficient from /LAC 19/, terminal solid solubility for dissolution (TSSd) from /KEA 67/, and for precipitation (TSSp) from /TOR 14/ for Zry-4. For D4 in DX D4 claddings, the terminal solid solubilities were modeled following the methodology described in /ZEM 21/.

CIEMAT

The hydrogen behavior in Zircaloy-4 claddings was evaluated by CIEMAT using HYDCLAD, an in-house one-dimensional hydrogen migration and precipitation model coupled with FRAPCON-xt /FER 20/. Hydrogen precipitation was simulated using the HNGD approach /PAS 20/, applying dynamic terminal solid solubilities as described in

/PAS 22/. For the benchmark analyses, the Kearns correlation /KEA 67/ was employed for TSSd, while the Zanellato et al. correlation /ZAN 12/ was used for TSSp. Hydride reorientation was modeled following the approach proposed in /DES 14/.

CNEA

The National Atomic Energy Commission of Argentina participated in the benchmark analyses using the in-house DIONISIO fuel performance code and the filtered input data. Hydrogen diffusion, together with hydride precipitation and reorientation, was modeled using the HNGD model /PAS 20/, coupled with the hydride reorientation approach proposed by Kolesnik et al. /KOL 18/. The terminal solid solubilities for precipitation (TSSp) and dissolution (TSSd) were determined using the solubility correlations proposed by Zanellato et al. /ZAN 12/ for Zry-4 and DX D4, and by Kim et al. /KIM 20/ for optimized ZIRLO.

GRS

GRS used the in-house code TESPA-ROD to perform the benchmark calculations. The simulations used the hydrogen dissolution and precipitation model implemented by Boldt/BOL 19/, which accounts for the kinetic effects of hydride growth and nucleation observed experimentally by Lacroix et al. /LAC 18/. Hydride orientation in the code is governed by a hoop stress threshold, as identified by Cinbiz et al. /CIN 15/. The hydrogen diffusion coefficient was taken from Kearns /KEA 72/, while the heat of transport for hydrogen in zirconium was adopted from /UNI 18/. The same modeling approach was applied to all three cladding types.

Framatome

Hydrogen diffusion and hydride formation were simulated using the HYDRA code, developed by Framatome. This two-dimensional model, based on the work of Marino in /MAR 72/ and /MAR 74/, accounts for materials with varying solubility in both the axial and radial directions, making it suitable for the analysis of duplex claddings. As only the total hydride content is available, without differentiation between circumferential and radial hydrides, the Framatome results are presented exclusively in terms of total and dissolved hydrogen concentrations.

KIT

KIT modeled hydride morphology in Zry-4 rods № 2, № 4, № 6, and № 8 using MORPHYD (MORPHology of HYDrides), as described in /KOL 23/ and /ALI 23/. Model parameters governing the tendency of hydrides to reorient were calibrated against experimental data reported in /KIM 15/. The hydrogen diffusion coefficient was adopted from /KEA 72/, and the hydrogen solubility in Zircaloy-4 was taken from /KIM 14/.

PSI

The Paul Scherrer Institute contributed two solutions to the benchmark section dedicated to hydrogen behavior analysis, employing the OFFBEAT and in-house HYPE codes. These are denoted as PSI-O and PSI-H in the figures.

In both approaches, the Hydrogen Nucleation, Growth, and Dissolution (HNGD) model /PAS 20/ was employed to describe hydride dissolution and precipitation phenomena. Hydride reorientation was modeled following the methodology proposed by Desquines et al. /DES 14/. The same hydrogen diffusion coefficient from Kearns /KEA 72/ and the heat of transport value determined by Kang /KAN 23/ were applied to all three cladding materials. In contrast, the terminal solid solubility for dissolution (TSSd) and precipitation (TSSp) were defined as material-specific parameters: for Zry-4 and the DX D4 substrate, data from Kammenzind /KAM 96/ were used; for optimized ZIRLO, values from Kim /KIM 20/ were adopted; and for the DX D4 liner, parameters were derived from experimental data reported by Gong et al. /GON 19/.

SNU

Seoul National University participated in the benchmark using the GIFT code, an in-house light water reactor fuel performance analysis tool developed at SNU. For the Zry-4 and optimized ZIRLO claddings, the transient precipitation behavior of hydrogen was simulated with the HNGD model /PAS 20/, and hydride reorientation was modeled following the methodology outlined in /JO 25/.

3.2.2 Benchmark results

This section presents the results of the second part of the first phase of the benchmark, dedicated to the investigation of hydrogen behavior following a long-term cooling transient. The experimental dataset used as a reference for comparison with the simulation results comprises hot vacuum gas extraction (HVGE) measurements performed at six axial positions along each fuel rod, light optical microscopy (LOM) images, and radial hydride fraction (RHF) values derived from the image analysis conducted by Kolesnik /KOL 26/. The estimation of the uncertainty associated with the hydride morphology metrics, kindly provided by Mikhail Kolesnik, is given in Appendix C.

Potential discrepancies associated with the initial hydrogen content, as discussed in Section 2.2.1, must to be taken into account when comparing experimental results with the hydrogen behavior predicted by the blind benchmark simulations. Errors in the assumed initial hydrogen concentration alter the transient precipitation kinetics and the subsequent hydride reorientation behavior. Consequently, for rods in which the hydrogen content used in the simulations deviates significantly from the values measured by hot vacuum gas extraction, accurately predicting the radial hydride fraction becomes highly challenging, making this the dominant contributor to the overall error.

In addition, pellet - cladding interaction (PCI), observed in a limited number of rods, introduces another source of discrepancy in the experiment - simulation comparison. Although confined to specific cases, these effects can locally influence the material response and are therefore addressed separately in the discussion of the affected rods.

Zry-4 Cladding

Zry-4 rod № 2 provides an appropriate starting point for the discussion of hydrogen-related results, as the initially estimated hydrogen content is in very good agreement with the post-test measurements obtained by hot-vacuum gas extraction. This rod was tested under maximum pressure conditions (hoop stress of approximately 93 MPa) with a target hydrogen concentration of 300 wppm, and was not affected by pellet–cladding interaction. This rod belongs to the internal rod group, for which the peak temperature of 392 °C occurs at the beginning of the experiment, near the rod’s mid-length, approximately at a bundle elevation between 450 mm and 550 mm. This region corresponds to zones 6 and 7 in the simulation domain discretization.

The initial hydrogen concentrations assumed in the calculations (dotted lines in Fig. 3.13, left) exhibit slight axial variability and are in good overall agreement with the hot-vacuum gas-extraction measurements (black diamonds in Fig. 3.13, left). The initial dissolved hydrogen profiles presented in Fig. 3.13 were extracted at t = 1.5 d, following the completion of the heating transient, at which point all calculations had converged to the initial steady-state condition, see Fig. 3.14.

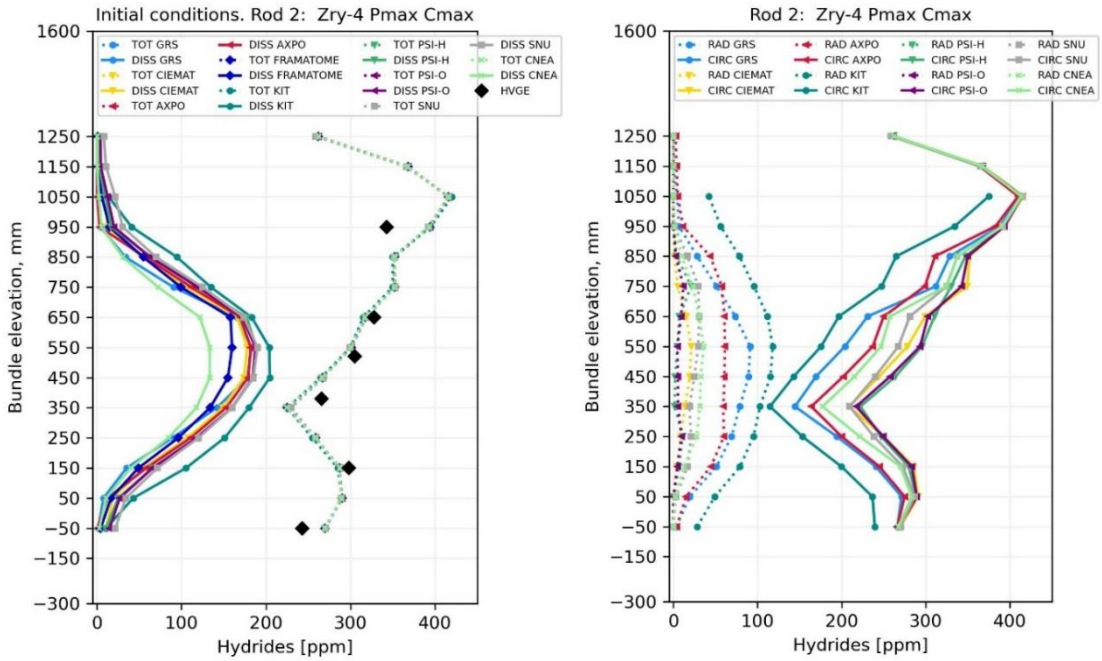

Fig. 3.13 Axial profiles in rod № 2 (initial dissolved and total hydrogen vs. HVGE, left) and final radial/circumferential hydride distributions (right)

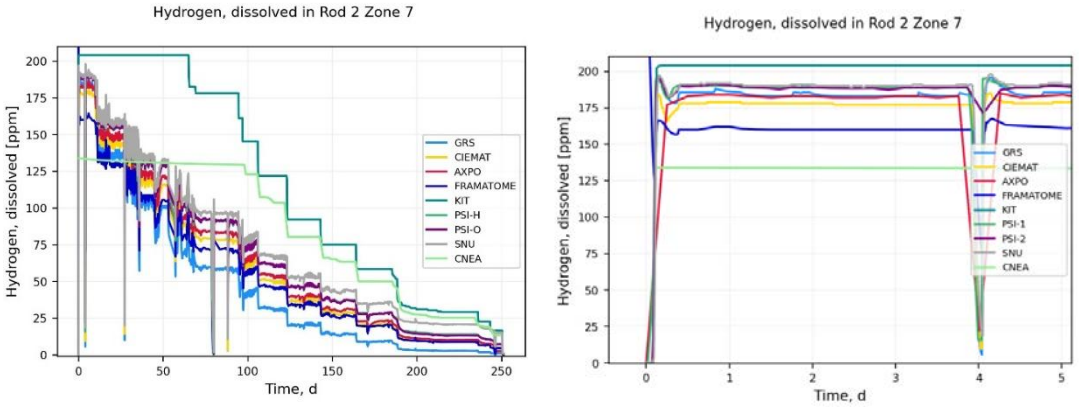

Fig. 3.14 Time evolution of dissolved hydrogen in Zone 7 of Rod № 2. Left: full experimental duration; right: first five days

The solid lines in Fig. 3.13 (left) denote the initial dissolved hydrogen concentration. Its axial distribution follows the bell-shaped temperature profile along the rod, reaching a

maximum of about 185 ppm in most simulation cases. The residual hydrogen that is not dissolved at the start of the experiment is assumed to exist as circumferentially oriented hydrides, in agreement with observations from the pre-test samples analyzed before the bundle experiment. Because the initial hydrogen content varies along the axial length of the rod, the amount of undissolved circumferential hydrides at the beginning of the experiment – and, consequently, at its end – also exhibits axial variation. The computed hydride distribution at the end of the experiment is presented on the right-hand side of Fig. 3.13; radial hydrides are indicated by dotted lines, whereas circumferential hydrides are shown as solid lines.

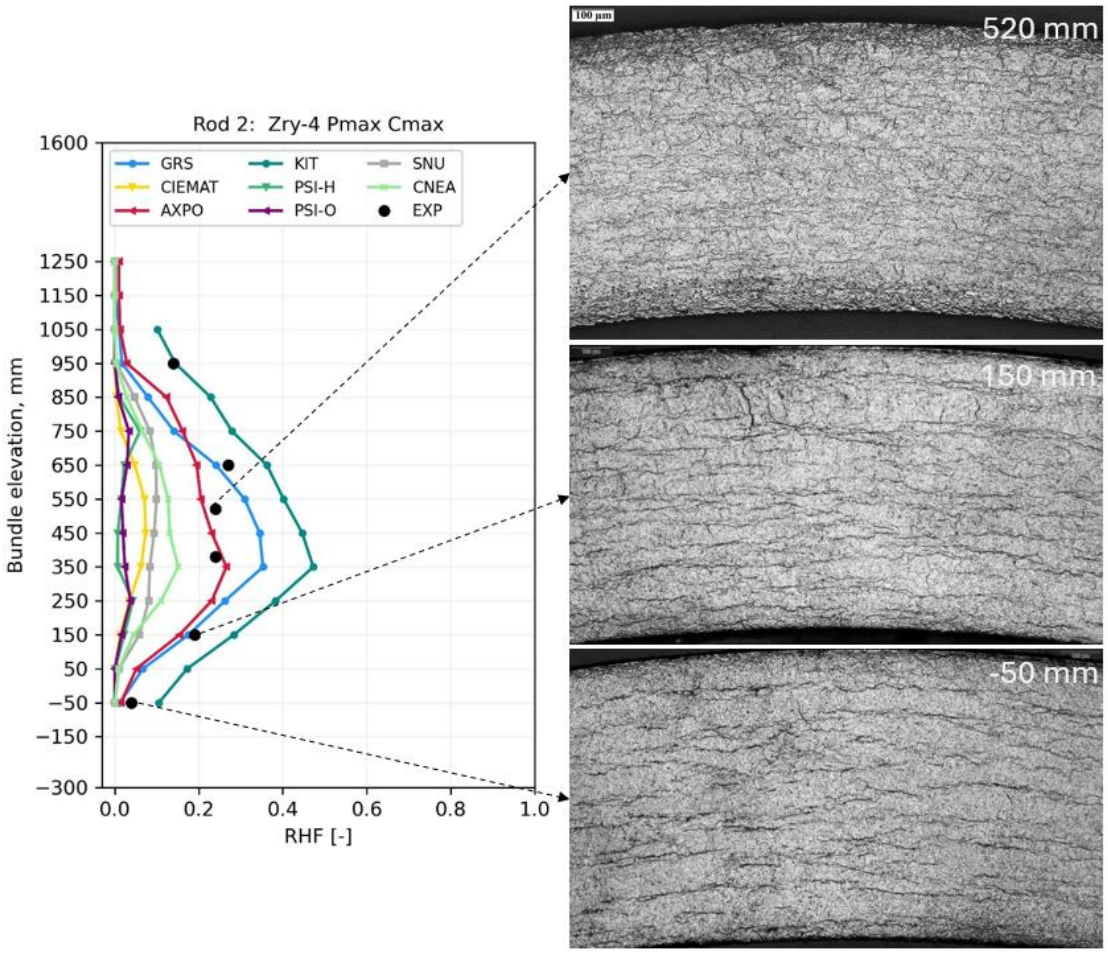

Fig. 3.15 Rod № 2: Radial hydride fraction axial profile vs. post-test metallography

In the post-test analysis, the radial hydride fractions (RHF) were quantified from LOM images. The measured RHF values (black dots in Fig. 3.15) are compared with the calculated results (colored lines in Fig. 3.15). At −50 mm, in the colder region where temperatures remain below 200 °C, hydrides are long and oriented circumferentially. At 520 mm, the hottest region, hydrides are smaller and oriented in both radial and circumferential directions.

While the metallographic images reveal that the majority of hydrides are oriented circumferentially with a presence of approximately 20 % radial hydrides, the simulations predict a broader range of RHF values, spanning from zero up to over 40 %.

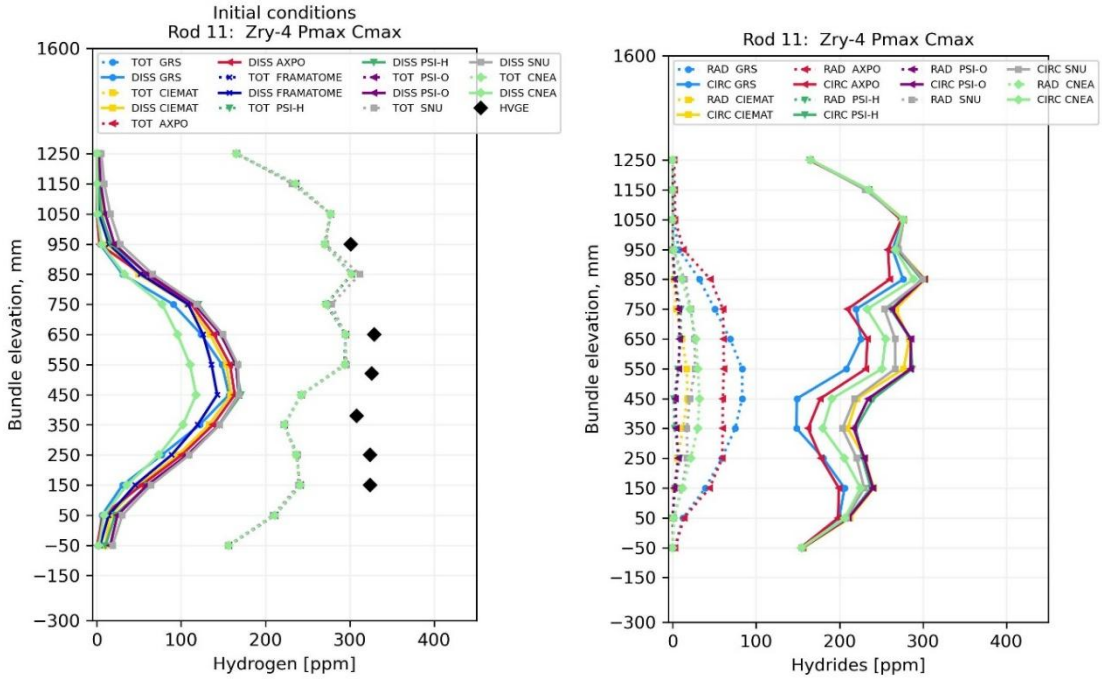

Fig. 3.16 Axial profiles in rod № 11 (initial dissolved and total hydrogen vs. HVGE, left) and final radial/circumferential hydride distributions (right)

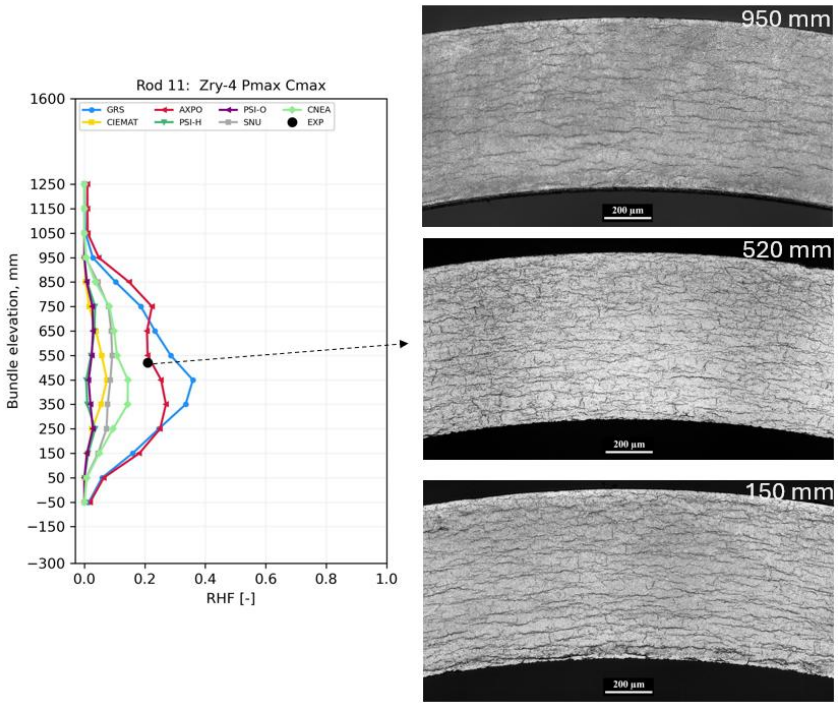

Fig. 3.17 Rod № 11: Radial hydride fraction axial profile vs. post-test metallography

Rod № 11 was subjected to conditions similar to Rod № 2; however, slightly less hydrogen is expected to dissolve due to its location at the bundle periphery, where temperatures are 10–15 °C lower.

Hot vacuum gas extraction results in Fig. 3.16 indicate that the initial hydrogen concentrations used in the simulations were underestimated, especially in the lower cladding region, complicating comparison with the experimental data.

Similar to Rod № 2, Rod № 11 exhibits approximately 20 % radial hydrides. LOM images in Fig. 3.17 indicate that at 950 mm, where the maximum temperature is about 200 °C and only a negligible amount of hydrogen is dissolved, hydrides remain predominantly circumferentially oriented. At 150 mm, where the maximum temperature reaches approximately 300 °C and about 50 ppm of hydrogen is dissolved, radial hydrides are already observed. Their fraction further increases towards the central region of the rod.

For both Zry-4 rods № 2 and № 11 at P_{max} and C_{max}, the GRS and KIT results overpredict the experimental RHF values, whereas the AXPO calculations show very good agreement with the measurements. The remaining simulations generally underpredict the radial hydride fraction.

Rod № 8 is the last Zry-4 rod pressurized to P_{max}. It belongs to the internal rod group and, unlike the previous two rods, has a lower initial hydrogen concentration. As shown in Fig. 3.18, all hydrogen is dissolved at the beginning of the simulation. However, the actual initial hydrogen concentration appears to be higher than originally estimated. As previously discussed in Section 3.1.2 in the context of the creep results, Rod № 8 was affected by PCI.

The radial hydride fraction extracted from LOM images exceeds 60 %, as shown in Fig. 3.19. These high values can be associated with the absence of pre-existing hydrides and the relatively high hoop stresses; however, pellet–cladding interaction was likely a significant contributing factor to the observed hydride reorientation. Further analysis of additional Zry-4 rods at similar test conditions is required to draw definitive conclusions. Simulations again indicate a wide range of RHF values, spanning from 0 % to nearly 80 %.

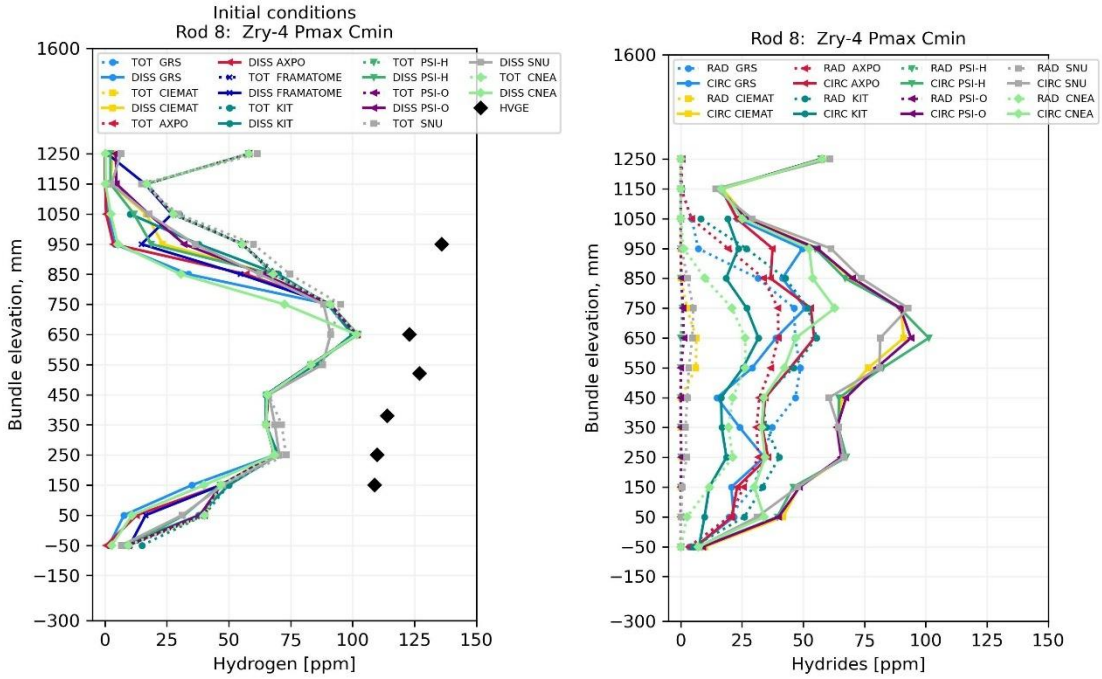

Fig. 3.18 Axial profiles in Rod № 8 (initial dissolved and total hydrogen vs. HVGE, left) and final radial/circumferential hydride distributions (right)

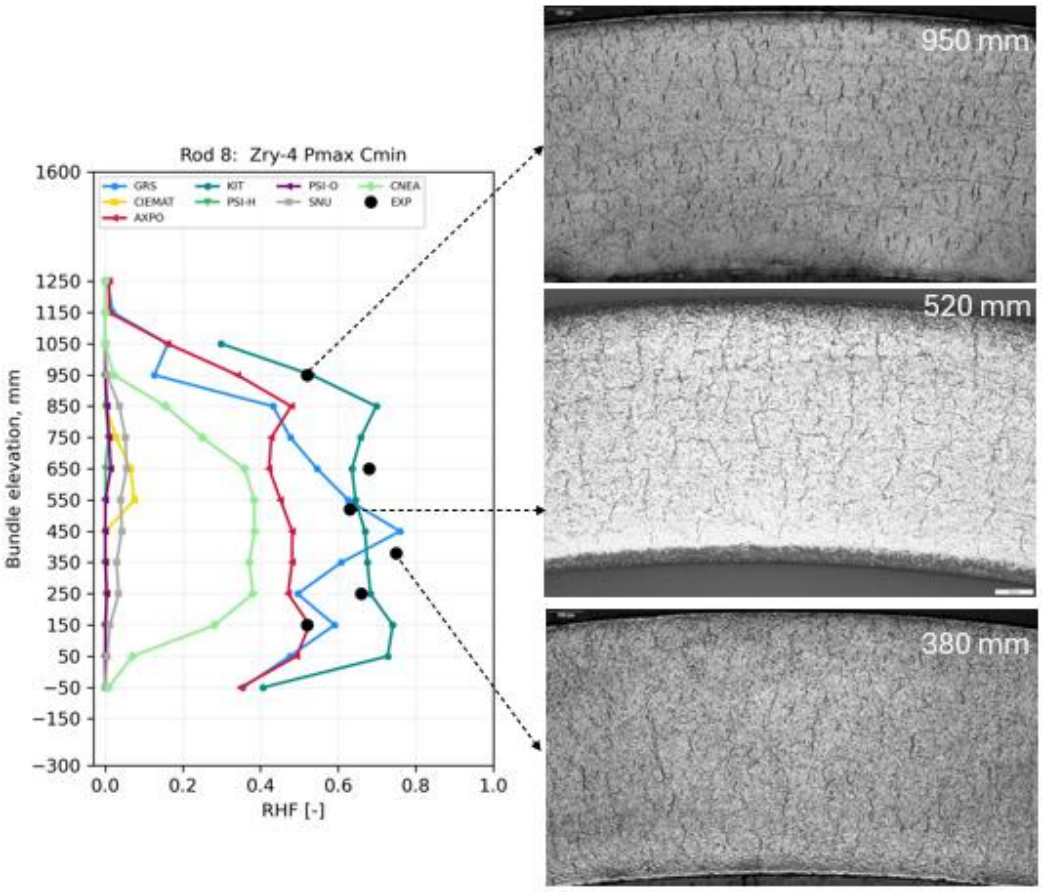

Fig. 3.19 Rod № 8: Radial hydride fraction axial profile vs. post-test metallography

The axial position of 950 mm corresponds to a relatively cold region, where the temperature at the beginning of the cooling experiment was approximately 200 °C and reached a short-term maximum of about 240 °C due to a temperature overshoot caused by mistaken manual control. Under these conditions, only a very small amount of hydrogen would be expected to dissolve and subsequently reprecipitate as radial hydrides. Nevertheless, the LOM image at 950 mm in Fig. 3.19 demonstrates a high degree of hydride reorientation, suggesting that locally increased hoop stresses were present.

The remaining Zry-4 rods №s 6, 17, 4, and 14, were all pressurized to P_{min}, resulting in a hoop stress of approximately 66 MPa. Rods № 6 and № 17 had a target hydrogen concentration of 300 ppm, while rods 4 and 14 had 100 ppm. As shown in Fig. 3.21, Fig. 3.23, Fig. 3.25, and Fig. 3.27, the initially estimated hydrogen content was lower than the values eventually measured, which affects the comparability of the simulated results with the experimental data.

At low pressure and low hydrogen concentration, most participants (GRS, CIEMAT, PSI-H, PSI-0, SNU) predict an almost complete absence of radial hydrides. As a result, the corresponding curves in Fig. 3.25 and Fig. 3.27 largely overlap, making them difficult to distinguish.

Rods № 6 and № 17 exhibit the lowest RHF among the Zry-4 rods, with measured values not exceeding 10 % (see Fig. 3.21 and Fig. 3.23). At lower hydrogen concentrations, the RHF increases modestly to approximately 10-20% (see Fig. 3.25 and Fig. 3.27), though it remains slightly lower than the RHF observed in the Rods № 2 and № 11 at Pmax and Cmax (see Fig. 3.15 and Fig. 3.17).

The AXPO and KIT results overestimate the fraction of radial hydrides at Pmin. In contrast, the majority of codes (GRS, CIEMAT, PSI-H, PSI-O, and SNU) predict negligible radial hydride formation under these low-pressure conditions. The CNEA results are in close agreement with the experimental findings, indicating a radial hydride fraction in the range of 10–20 %.

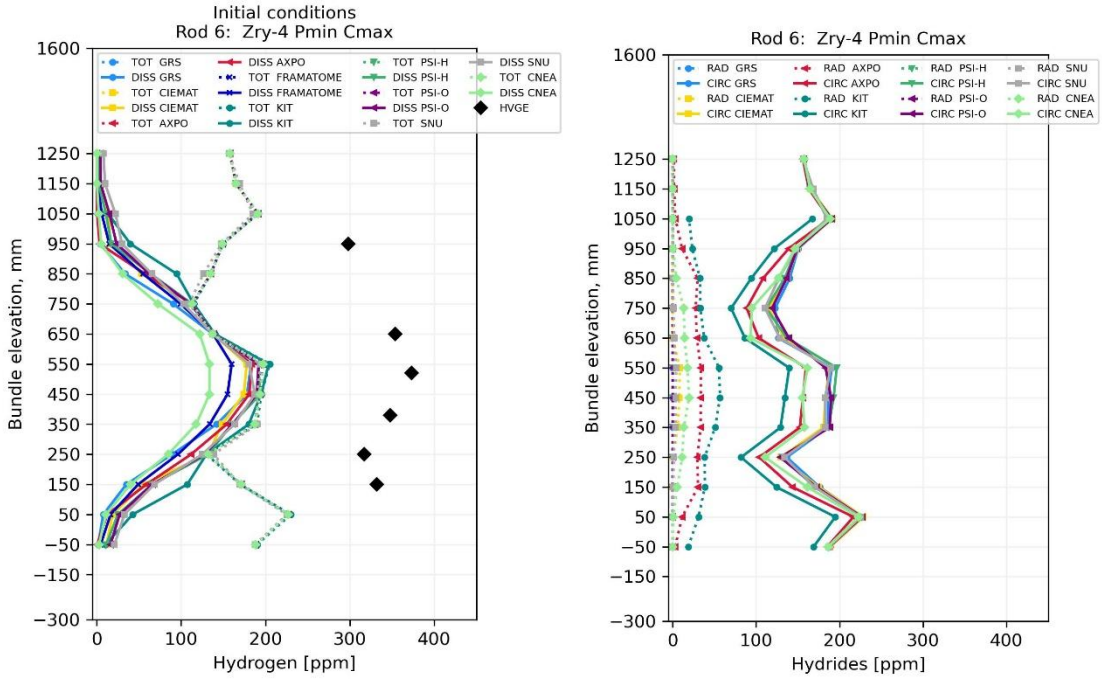

Fig. 3.20 Axial profiles in rod № 6 (initial dissolved and total hydrogen vs. HVGE, left) and final radial/circumferential hydride distributions (right)

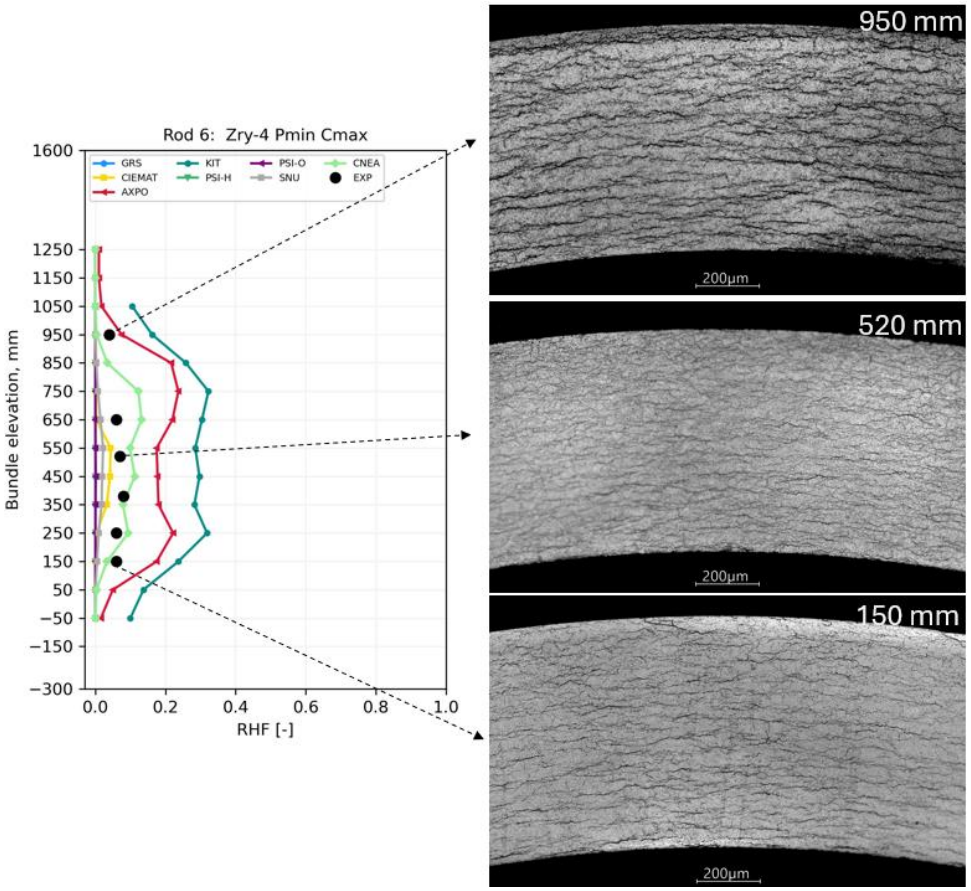

Fig. 3.21 Rod № 6: Radial hydride fraction axial profile vs. post-test metallography

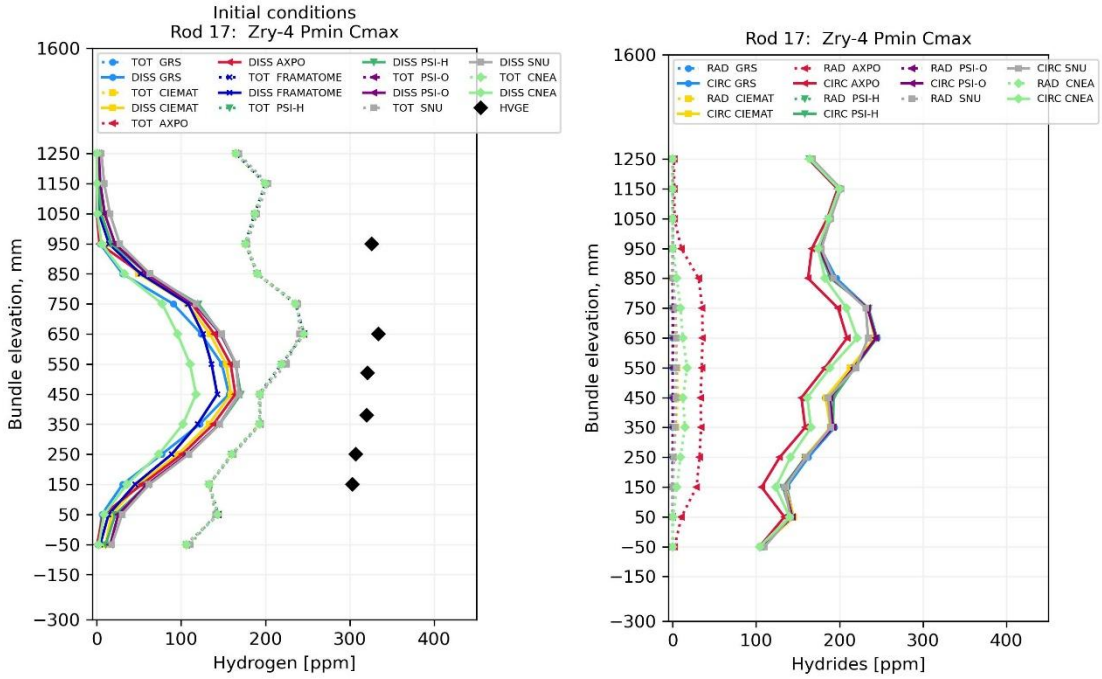

Fig. 3.22 Axial profiles in rod № 17 (initial dissolved and total hydrogen vs. HVGE, left) and final radial/circumferential hydride distributions (right)

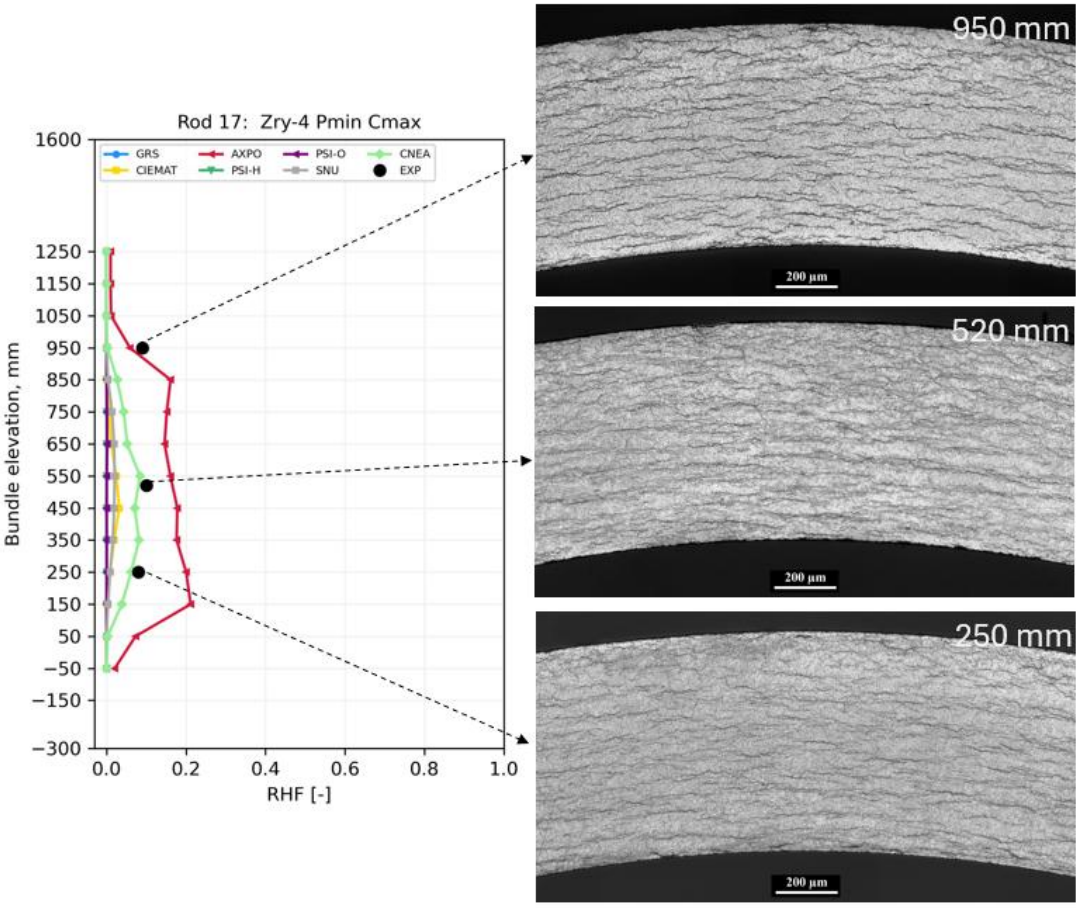

Fig. 3.23 Rod № 17: Radial hydride fraction axial profile vs. post-test metallography

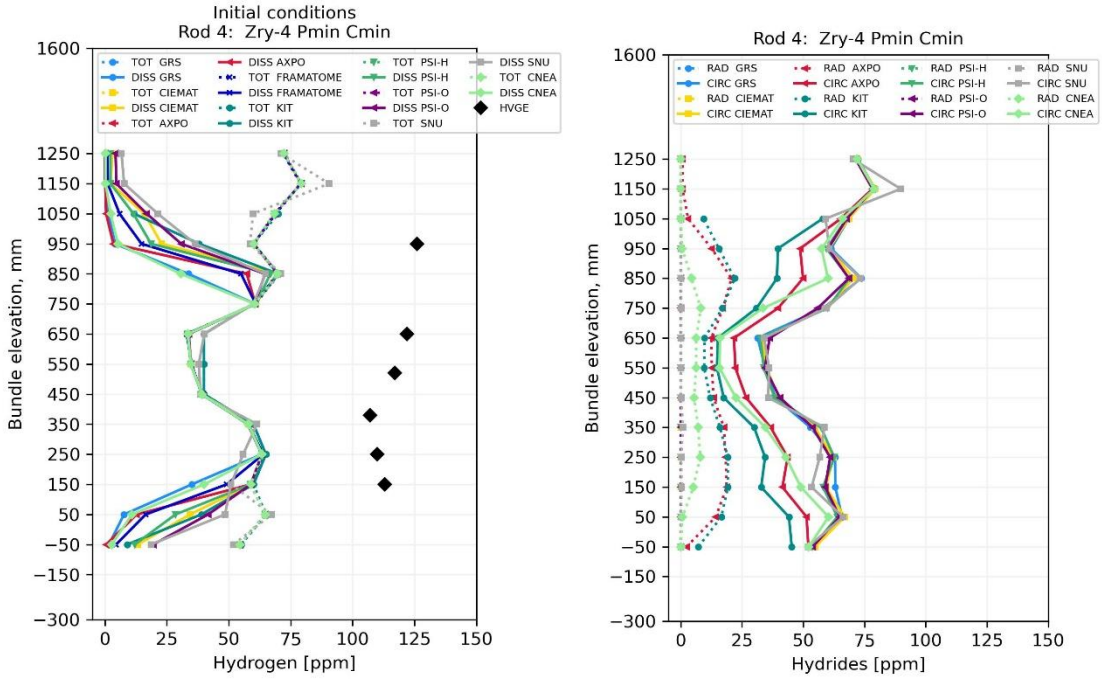

Fig. 3.24 Axial profiles in rod № 4 (initial dissolved and total hydrogen vs. HVGE, left) and final radial/circumferential hydride distributions (right)

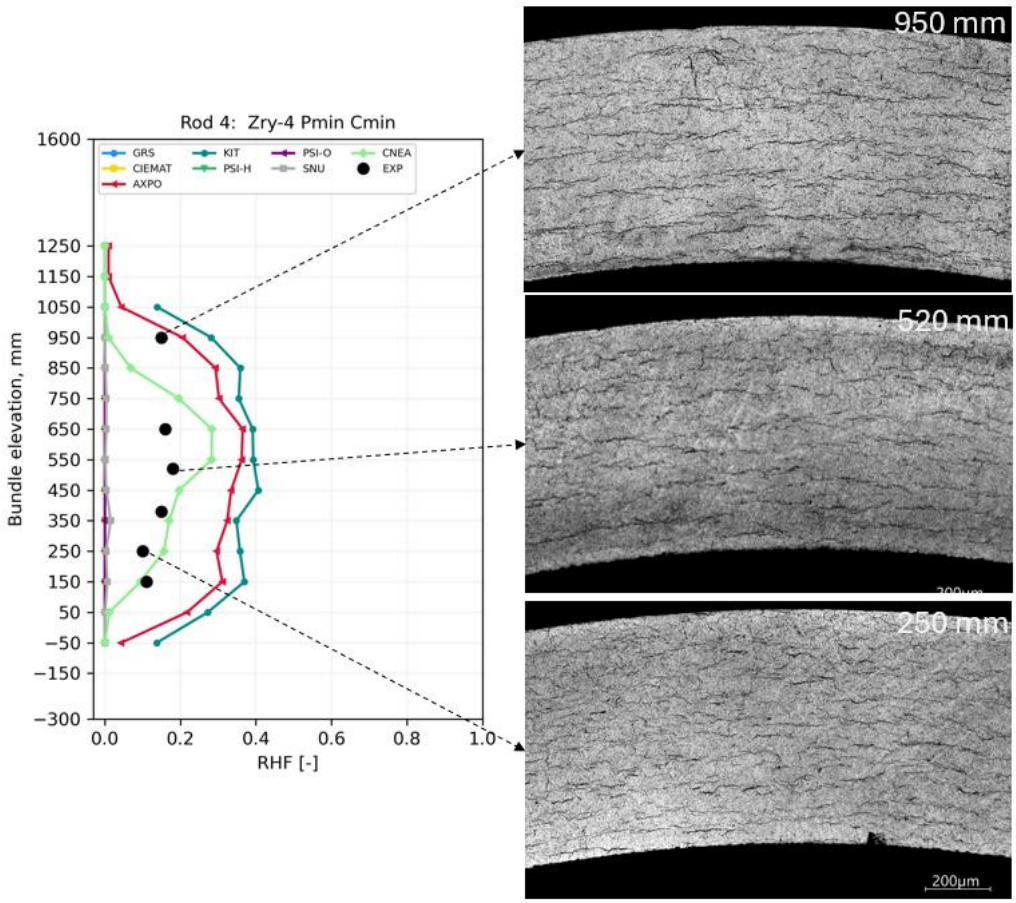

Fig. 3.25 Rod № 4: Radial hydride fraction axial profile vs. post-test metallography

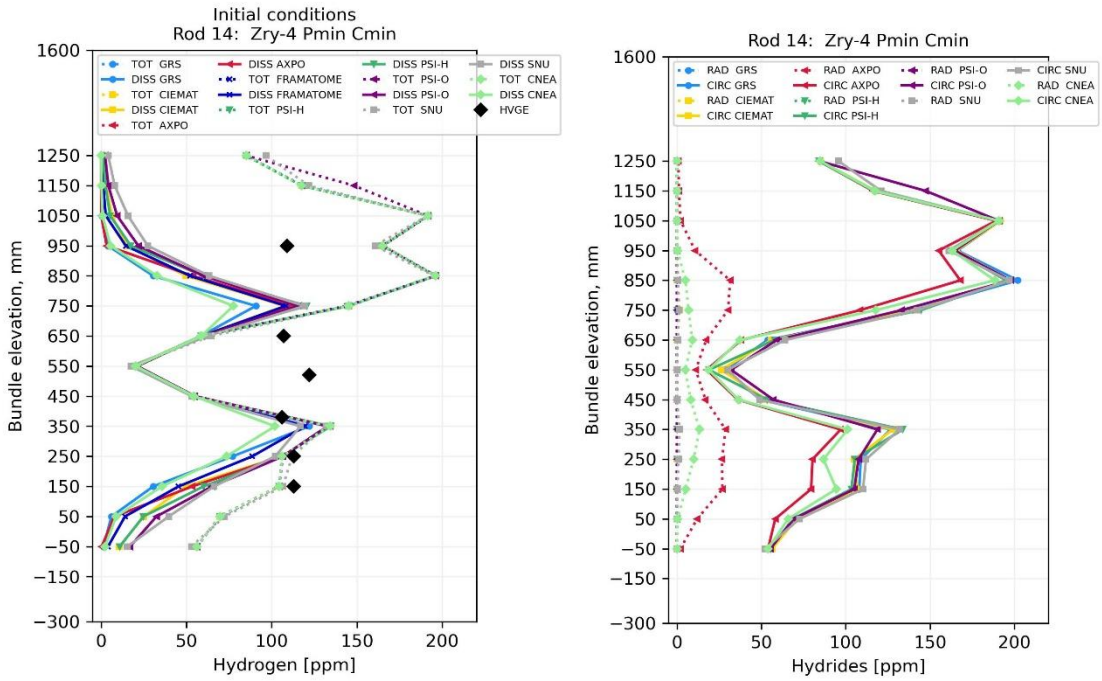

Fig. 3.26 Axial profiles in rod № 14 (initial dissolved and total hydrogen vs. HVGE, left) and final radial/circumferential hydride distributions (right)

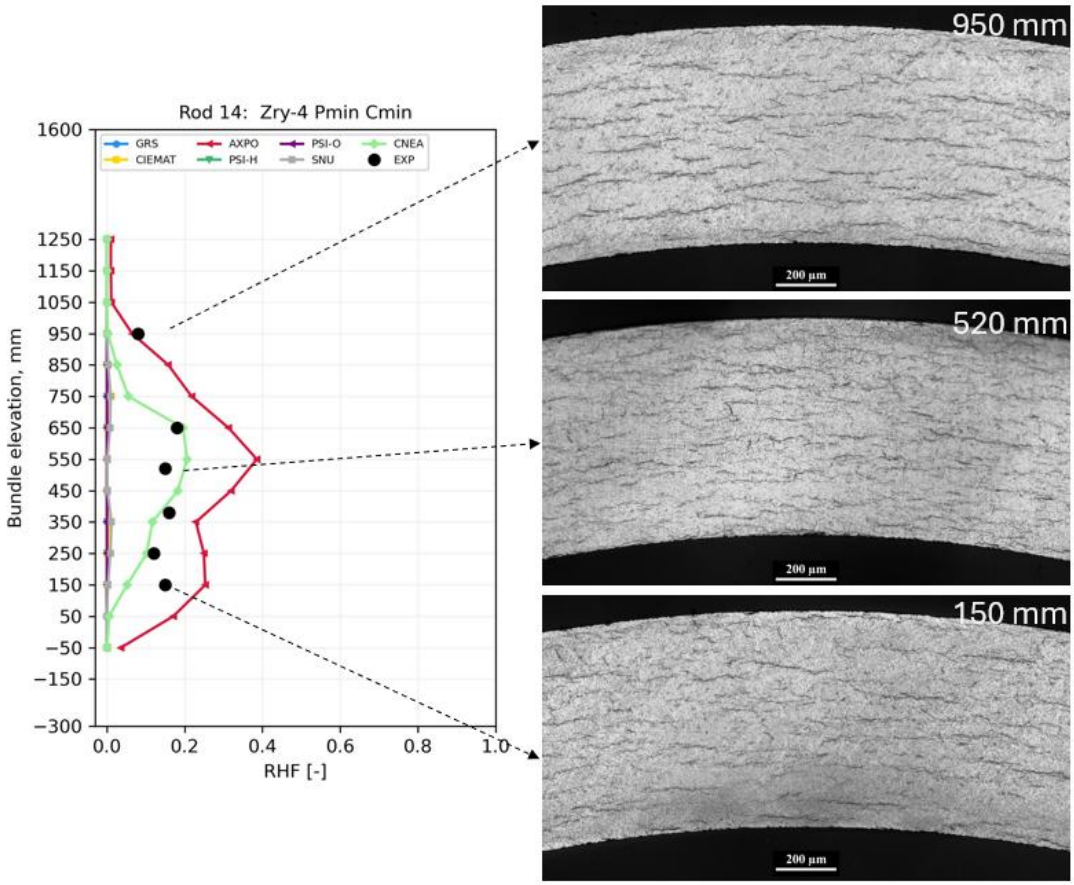

Fig. 3.27 Rod № 14: Radial hydride fraction axial profile vs. post-test metallography

The radial hydride fraction is plotted as a function of the initial temperature in Fig. 3.28. Data for rods with a target hydrogen concentration of 100 ppm are presented in the left panel, whereas the corresponding results for 300 ppm are shown in the right panel. Only the axial planes that were experimentally analyzed are included in this evaluation. Experimental results are shown in black, while colored symbols indicate simulated results. Diamonds represent the rods affected by PCI. Filled symbols correspond to rods at P_{max}, and unfilled symbols to rods at P_{min}.

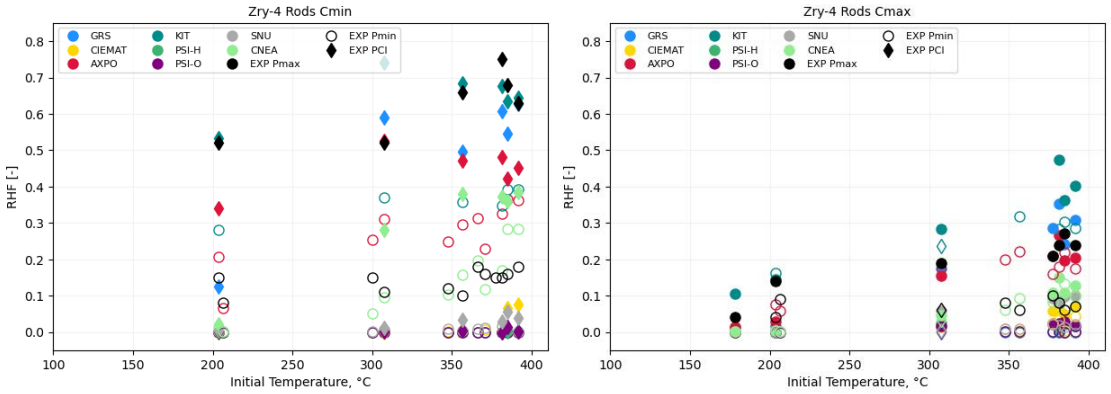

Fig. 3.28 Zry-4 claddings: RHF vs. initial temperature. Left: C_{min}; Right: C_{max}

Comparing the left and right panels of Fig. 3.28, experiments indicate higher RHF at lower hydrogen concentrations, a trend that the simulations qualitatively reproduce. Higher starting temperatures enable greater hydrogen dissolution and potential reorientation, a trend that is also reproduced to some extent by the models. It should be noted, however, that comparison at C_{min} is limited due to large discrepancies between the initial and measured hydrogen concentrations. Since at low pressure and low hydrogen concentration most participants predict an almost complete absence of radial hydrides, the corresponding data points on the left side of Fig. 3.28 overlap.

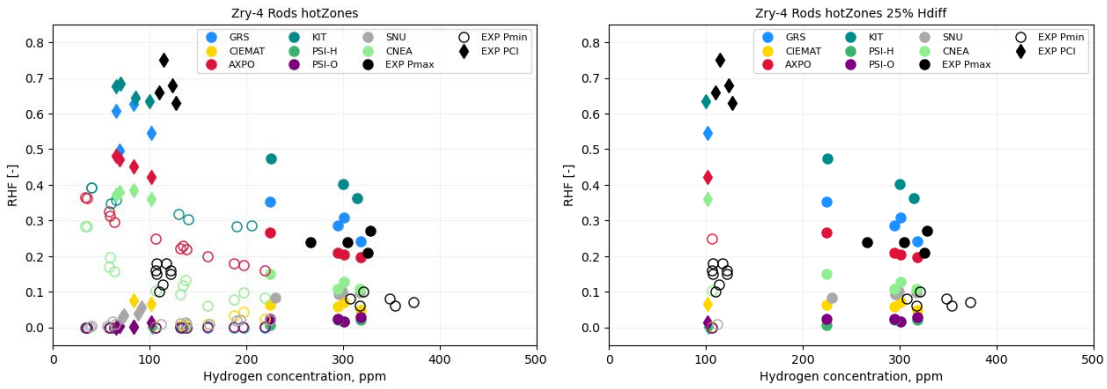

Fig. 3.29 Zry-4 claddings: RHF vs. initial hydrogen concentration, initial temperature> 350°C. Left: all results; Right: $\left|C_{H,\,HVGE} - C_{H,\,ini}\right| < 25\%\ of C_{H,\,target}$.

To analyze the effect of hydrogen content on radial hydride formation, the RHF is plotted as a function of hydrogen concentration for the hottest region, where temperatures exceeded 350 °C, in Fig. 3.29. While the left side of Fig. 3.29 shows all simulated results, the right side includes only simulations for which the discrepancy between estimated hydrogen content and the concentration measured by hot-vacuum gas extraction did not exceed 25 % of the target. The simulations indicate a negative correlation between RHF and increasing initial hydrogen concentration, a trend observed in the experimental results.

DX D4 cladding

While the creep behavior of Zry-4 and DX D4 claddings demonstrates similar characteristics, the hydrogen behavior follows a different trend. A radial resolution analysis of the duplex cladding, including the liner, was not requested within the scope of the benchmark. AXPO and Framatome performed explicit modeling of the liner, while the remaining participants adopted an approach analogous to that used for Zry-4. Framatome reported averaged values for the liner and bulk material over axial cladding sections. Consequently, the hydride results presented below for DX D4 refer only to the substrate of the duplex cladding; for Framatome, they represent averages of the base material and the liner.

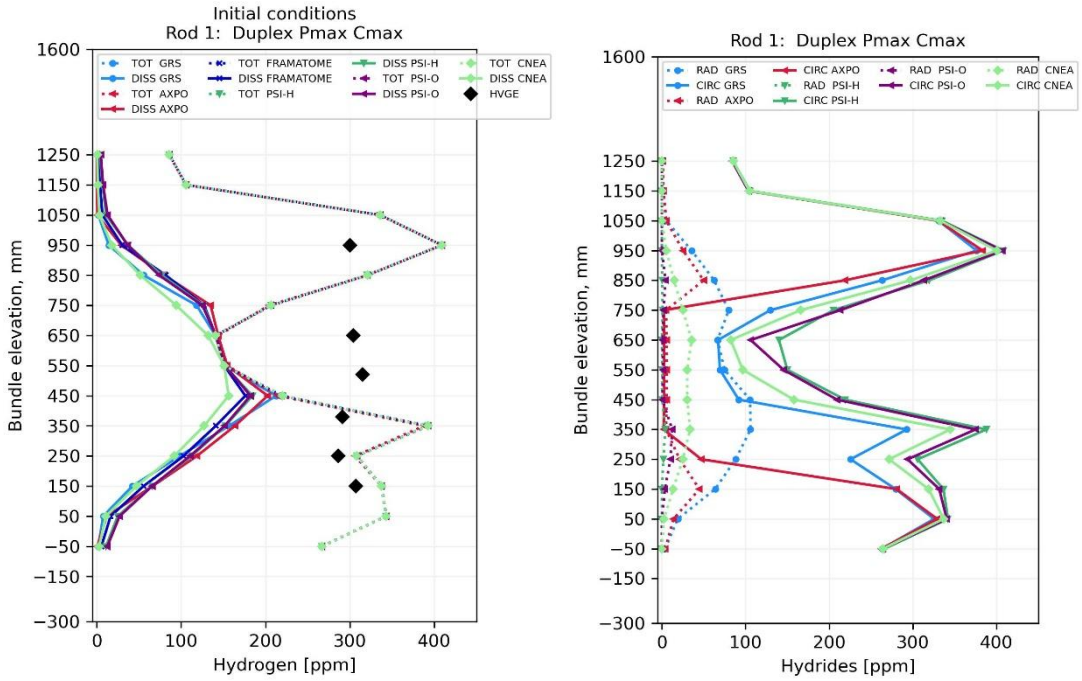

Fig. 3.30 Axial profiles in rod № 1 (initial dissolved and total hydrogen vs. HVGE, left) and final radial/circumferential hydride distributions (right)

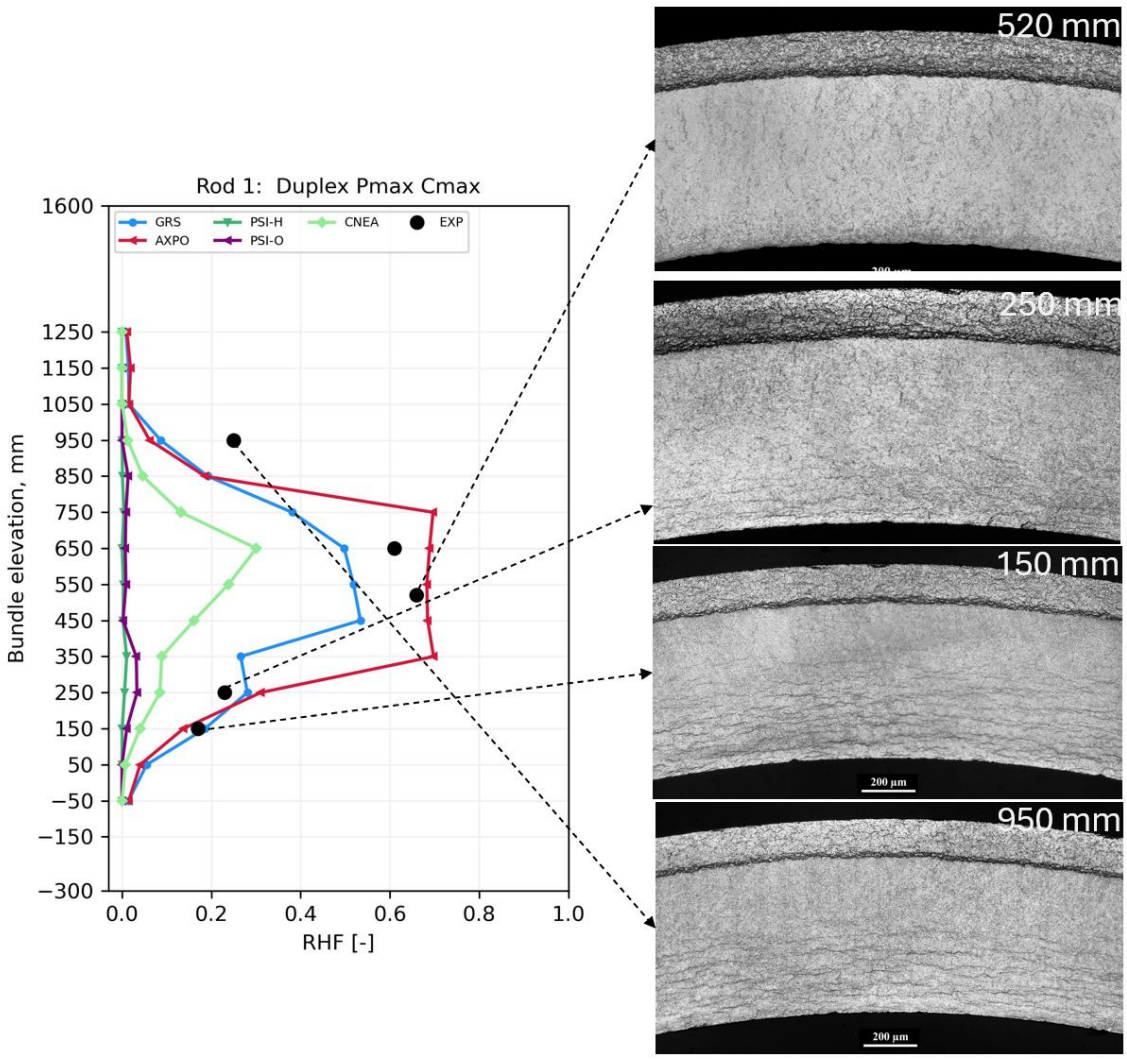

Fig. 3.31 Rod № 1: Radial hydride fraction axial profile vs. post-test metallography

The temperatures of the central rod № 1 are the highest within the bundle, reaching 405 °C at its mid-height. This rod was pressurized at P_{max} with a target hydrogen concentration of 300 ppm. While the estimated hydrogen profile indicated a strong variation, decreasing to approximately 150 ppm at the center, post-test measurements revealed a nearly uniform hydrogen distribution with values close to 300 ppm, as shown in Fig. 3.30. This difference should be taken into account when interpreting the results.

The LOM images in Fig. 3.31 reveal substantial hydrogen migration into the liner and the presence of radially oriented hydrides in the substrate. The hydride distribution across the cladding thickness is non-uniform, being dense and mainly circumferential at the pellet side, and more sparse and predominantly radial in the vicinity of the liner. The depleted zone expands with increasing temperature. It should be noted, however, that the

RHF plotted on the left side of Fig. 3.31 represents an integral measure averaged over the full substrate thickness.

Simulations show a broad spread in predicted RHF, similar to Zry-4 under the same conditions, while the experiment indicates RHF values approximately three times higher than for pure Zry-4 claddings. As shown on the right of Fig. 3.30, AXPO calculations indicate that both circumferential and radial hydrides in the central region are nearly absent. This suggests that almost all hydrogen has migrated into the liner, with only a few ppm remaining in the substrate. A similar distribution in the central region was predicted by Framatome. However, LOM images indicate a slightly higher hydrogen content remaining in the bulk material.

Similar behavior is observed for the peripheral Rod № 20, which was also at P_{max} and Cmax, see Fig. 3.32 and Fig. 3.33. Slightly lower hydrogen dissolution in this rod is expected due to the reduced temperatures at the bundle periphery. The quality of the metallography, however, limits the analysis of this rod.

The peripheral rod № 21 was pressurized to P_{max} with a hydrogen content of approximately 100 ppm, as shown in Fig. 3.34. LOM image analysis indicates an RHF in the central region slightly exceeding 60 %, comparable to the values observed for rods № 1 and № 20, as demonstrated in Fig. 3.35. The remaining hydrogen content in the bulk is minimal compared to the 300 ppm samples.

Both DX D4 rods with lower hoop stresses of approximately 66 MPa - internal rod № 9 and peripheral rod № 19, with high and low hydrogen content, respectively - showed substantially fewer radial hydrides than rods № 1, № 20, and № 21 at the higher pressure.

RHF values in the rod №9 with 300 ppm hydrogen were generally close to or below 20 % (see Fig. 3.37), decreasing to approximately 12 % in Rod № 19, where the hydrogen content was around 100 ppm (see Fig. 3.39).

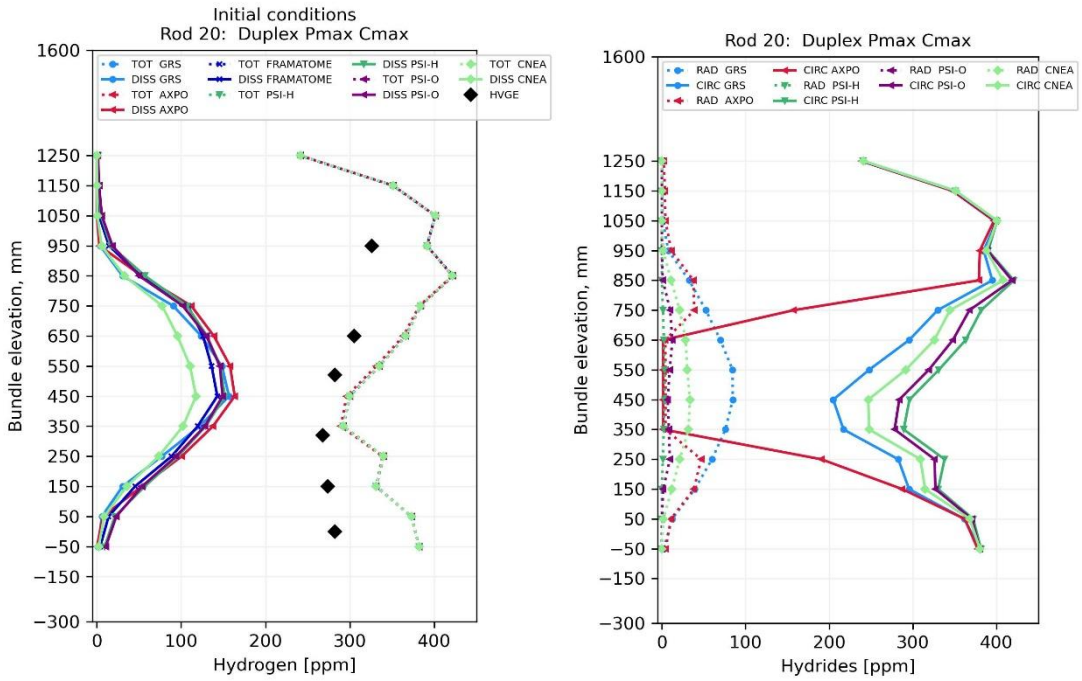

Fig. 3.32 Axial profiles in rod № 20 (initial dissolved and total hydrogen vs. HVGE, left) and final radial/circumferential hydride distributions (right)

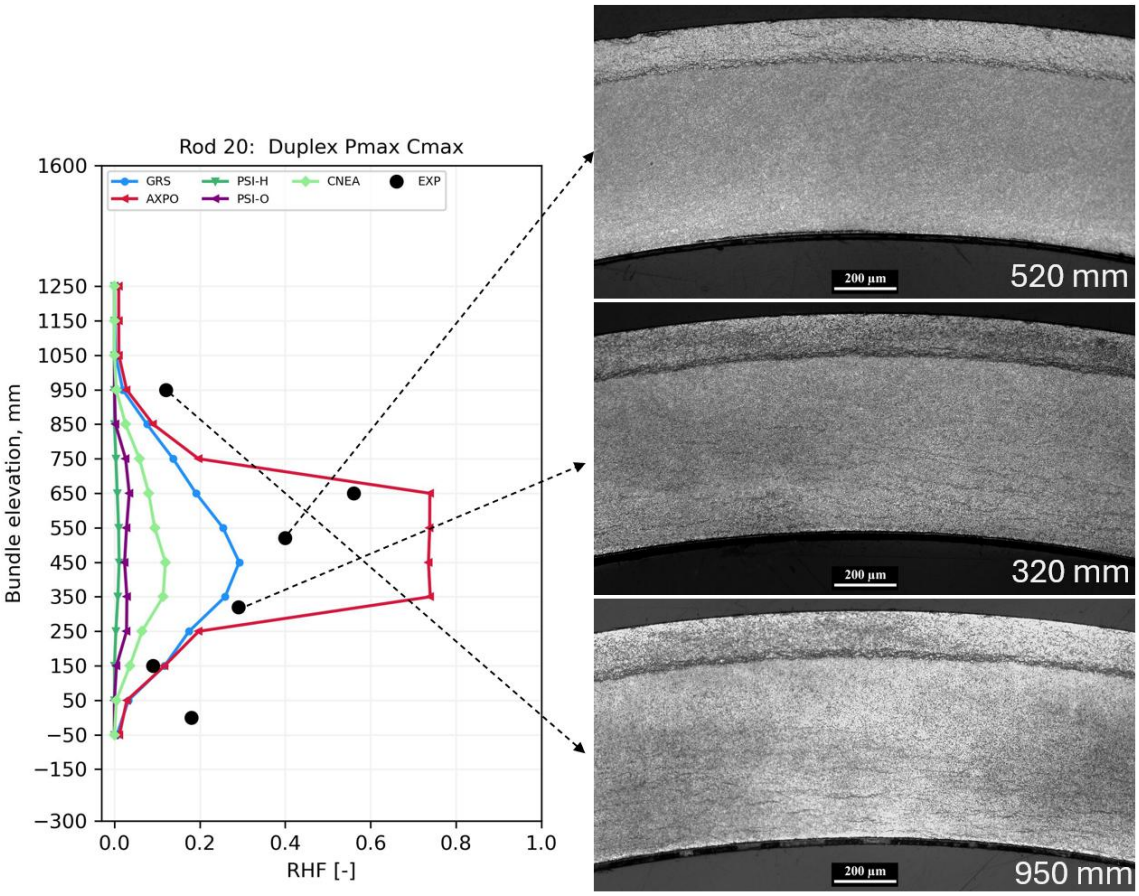

Fig. 3.33 Rod № 20: Radial hydride fraction axial profile vs. post-test metallography

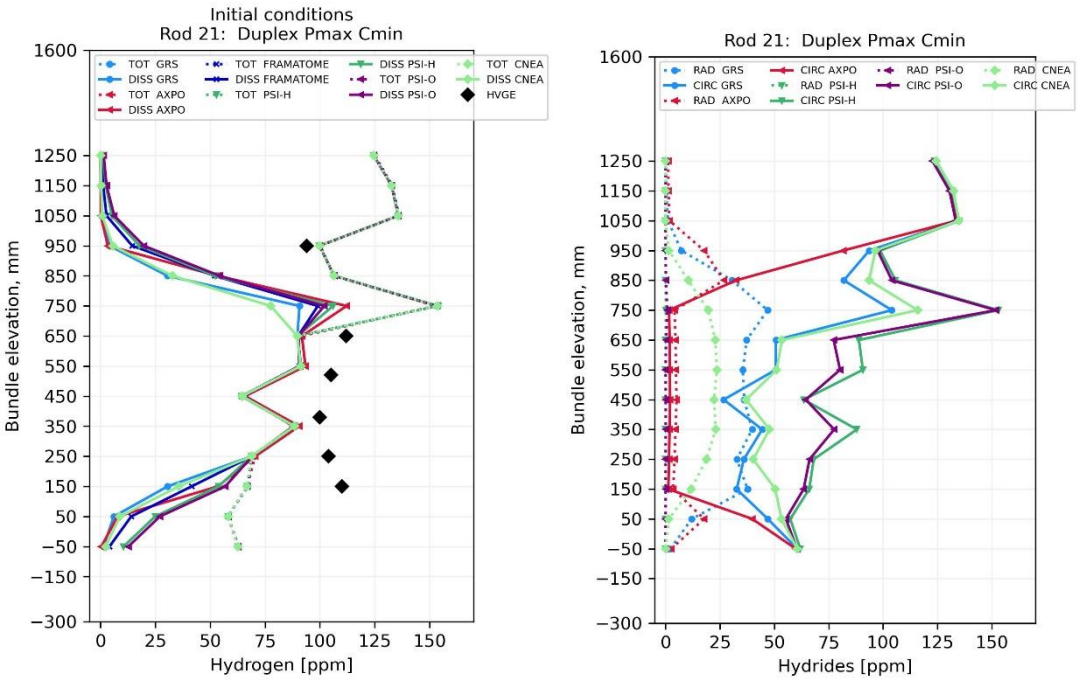

Fig. 3.34 Axial profiles in rod № 21 (initial dissolved and total hydrogen vs. HVGE, left) and final radial/circumferential hydride distributions (right)

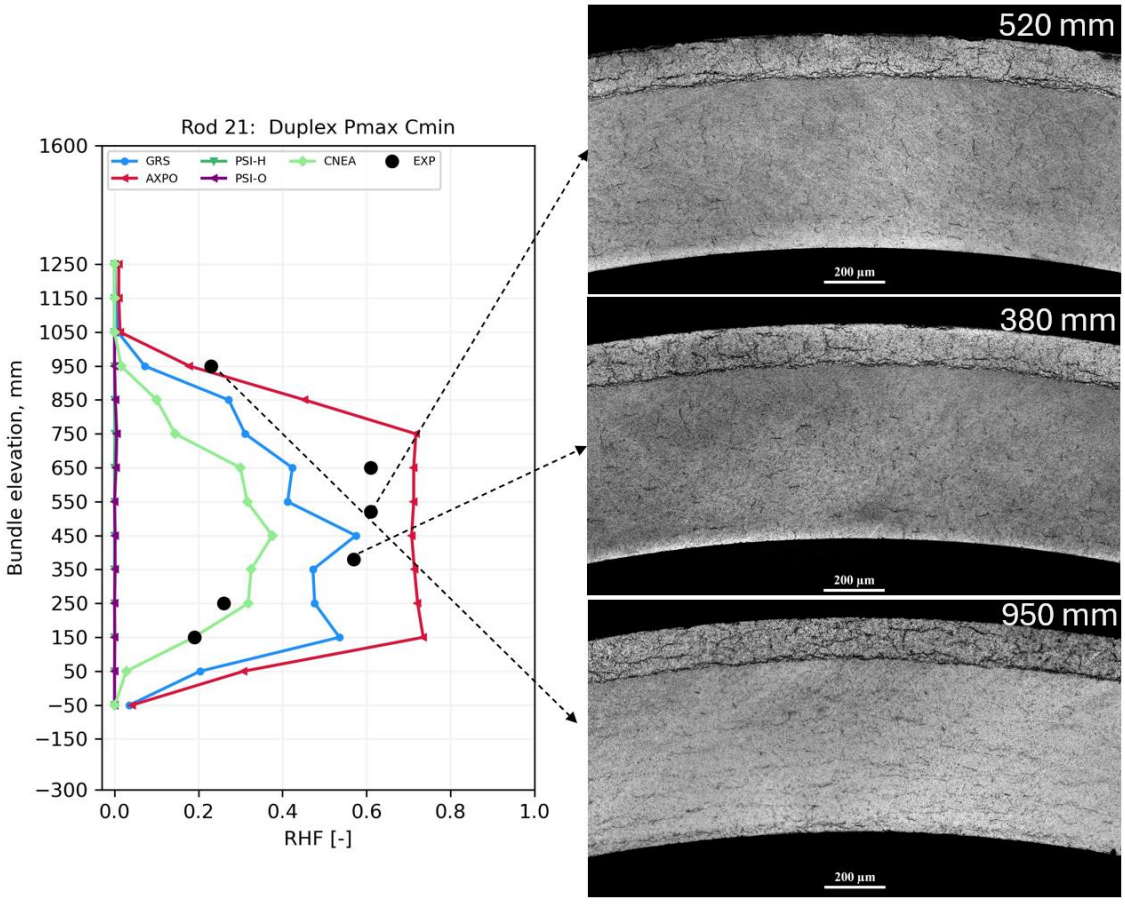

Fig. 3.35 Rod № 21: Radial hydride fraction axial profile vs. post-test metallography

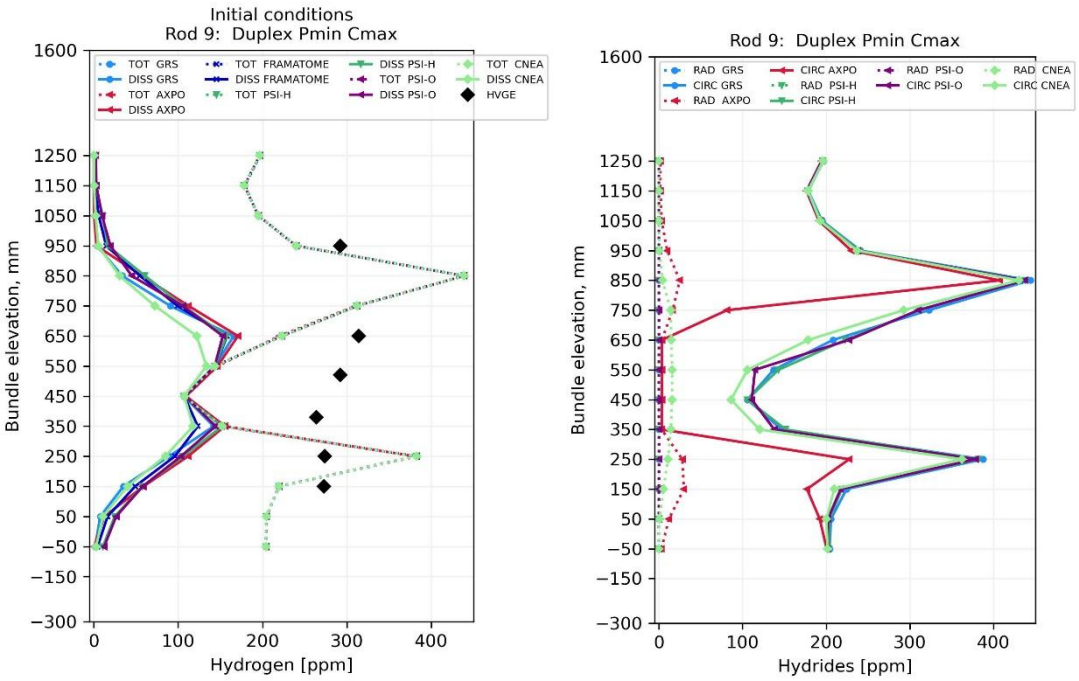

Fig. 3.36 Axial profiles in rod № 9 (initial dissolved and total hydrogen vs. HVGE, left) and final radial/circumferential hydride distributions (right)

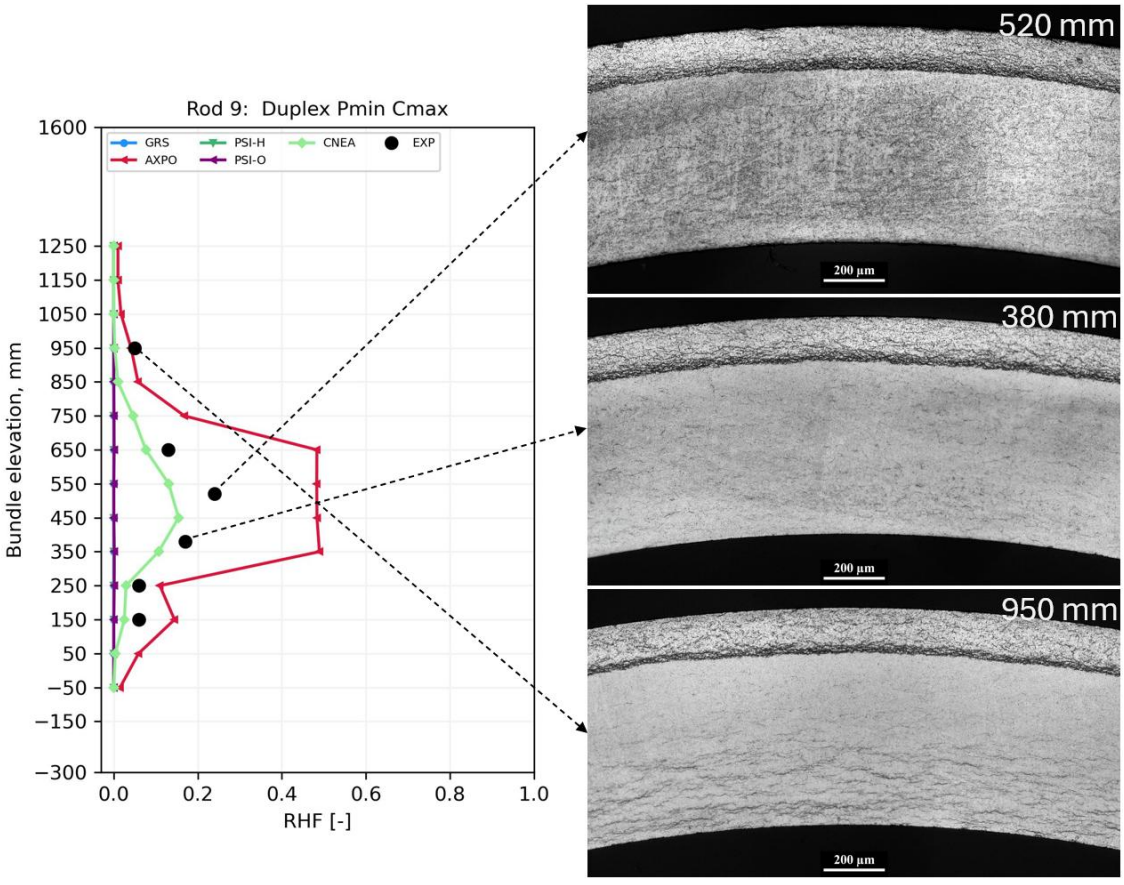

Fig. 3.37 Rod № 9: Radial hydride fraction axial profile vs. post-test metallography

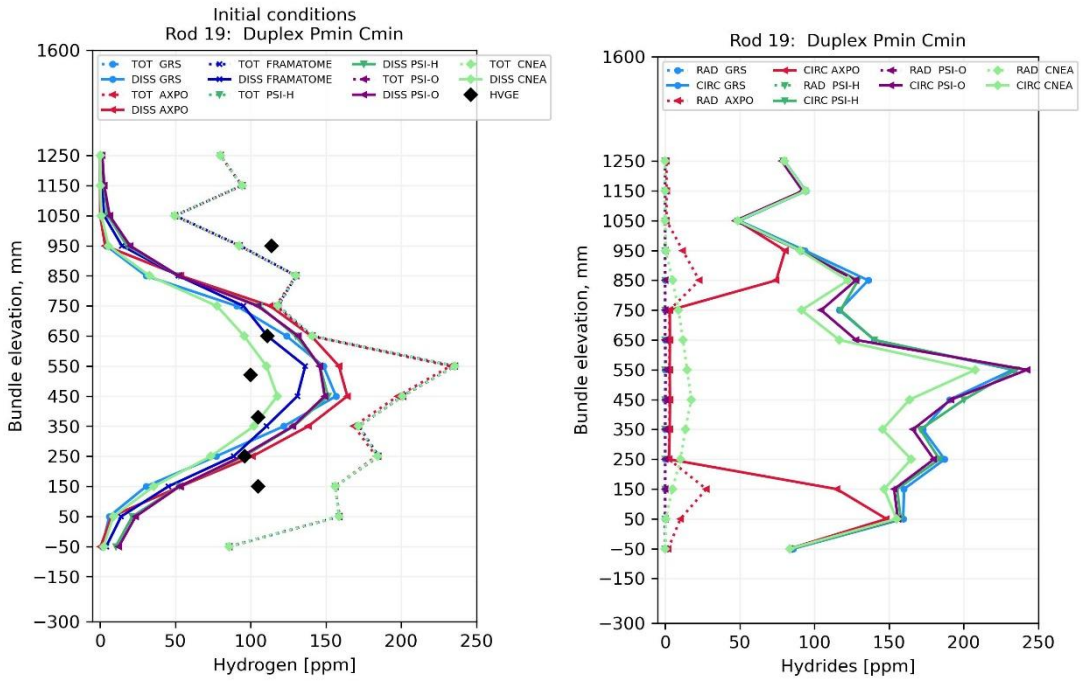

Fig. 3.38 Axial profiles in rod № 9 (initial dissolved and total hydrogen vs. HVGE, left) and final radial/circumferential hydride distributions (right)

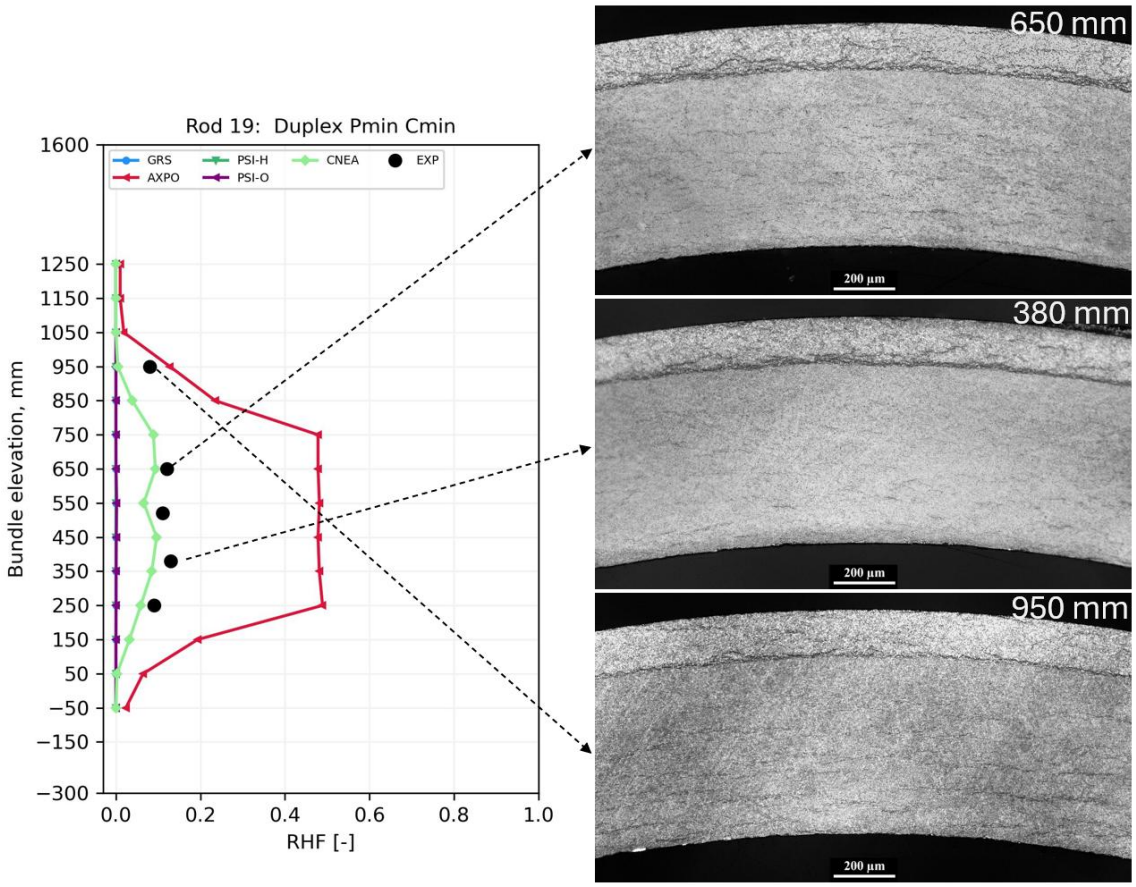

Fig. 3.39 Rod № 19: Radial hydride fraction axial profile vs. post-test metallography

Fig. 3.40 and Fig. 3.41 summarize all the data for DX D4 and show a structure similar to that previously discussed for Zry-4 claddings (see Fig. 3.28 and Fig. 3.29). Unlike in the Zry-4 claddings, the amount of radial hydrides in the bulk of the duplex claddings does not decrease with increasing hydrogen concentration, as can be seen by comparing the left and right sides of Fig. 3.40.

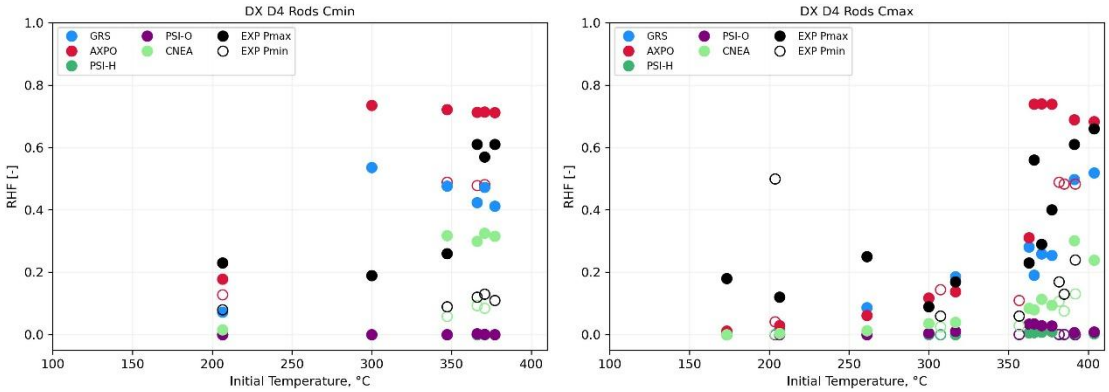

Fig. 3.40 DX D4 claddings: RHF vs. initial temperature. Left: C_{min}; Right: C_{max}

At P_{max}, DX D4 exhibits approximately three times higher fractions of radial hydrides than Zry-4, whereas at P_{min}, the radial hydride fraction for both cladding types remains within 10–20 %, see Fig. 3.41.

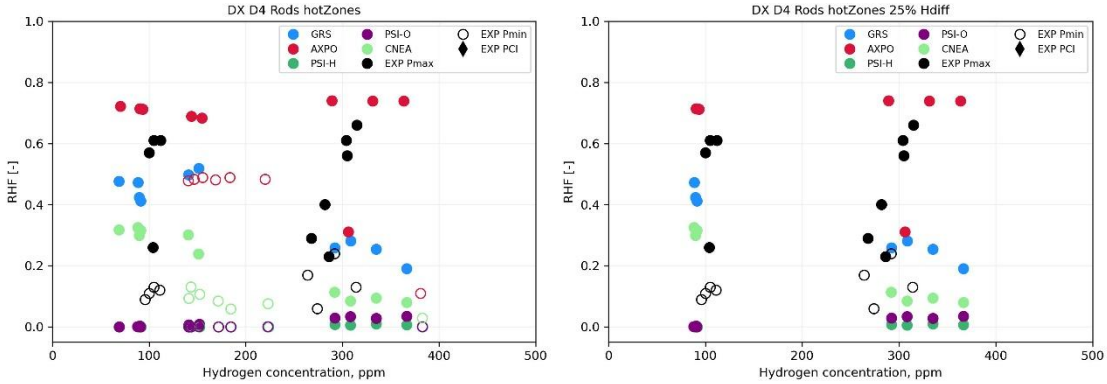

Fig. 3.41 DX D4 claddings: RHF vs. initial hydrogen concentration, initial temperature> 350 °C. Left: all results; Right: $\left|C_{H,\,HVGE} - C_{H,\,ini}\right| < 25\%\ of C_{H,\,target}$

The non-uniform hydride distribution across the duplex cladding thickness makes an integral consideration of the bulk material overly simplified, highlighting the need for a more detailed radial description. Benchmark calculations further demonstrate that modeling both the liner and the bulk is essential for accurately predicting the behavior of duplex claddings.

Opt.ZIRLO Cladding

Compared to Zry-4 and DX D4 claddings, Opt.ZIRLO claddings show a significantly lower fraction of radial hydrides. The highest radial hydride fraction (19 %) was observed in the central region of the internal rod № 3, pressurized at P_{max}, with a local hydrogen concentration of approximately 125 ppm, as shown in Fig. 3.43.

The peripheral rod № 12 was subjected to similar test conditions. However, the rod № 12 experienced approximately 2.8 times less creep deformation than rod №3 due to the lower temperatures at the bundle periphery relative to the internal rod ring. At the same axial position, the measured RHF in rod № 12 was approximately half of that observed in rod № 3 (see Fig. 3.45).

As discussed in Section 3.1.2, rod № 12 experienced PCI, especially in the lower portion of the rod. At the 150 mm elevation (Fig. 3.45), this effect is evident, with most hydrides exhibiting radial orientation.

Opt.ZIRLO rods № 7 and № 10, both at P_{max} with higher hydrogen content, exhibit even lower RHF values, not exceeding 8 % (see Fig. 3.47 and Fig. 3.49). The radial hydrides observed at the 150 mm and 950 mm elevations of Rod № 7 may be associated with PCI, as profilometry measurements in these regions indicate noticeable scatter.

Optimized ZIRLO claddings subjected to lower hoop stresses of 66 MPa exhibit a nearly complete absence of radial hydrides, regardless of their position within the bundle or their initial hydrogen content (see Fig. 3.51, Fig. 3.53, Fig. 3.55, Fig. 3.57).

The general modeling approach for Opt.ZIRLO was to use the same framework as for Zry-4, with adjusted terminal solid solubility values specific to Opt.ZIRLO, which are slightly higher than those of Zry-4. As a result, simulations yield very similar predictions for Zry-4 and Optimized ZIRLO rods under identical test conditions.

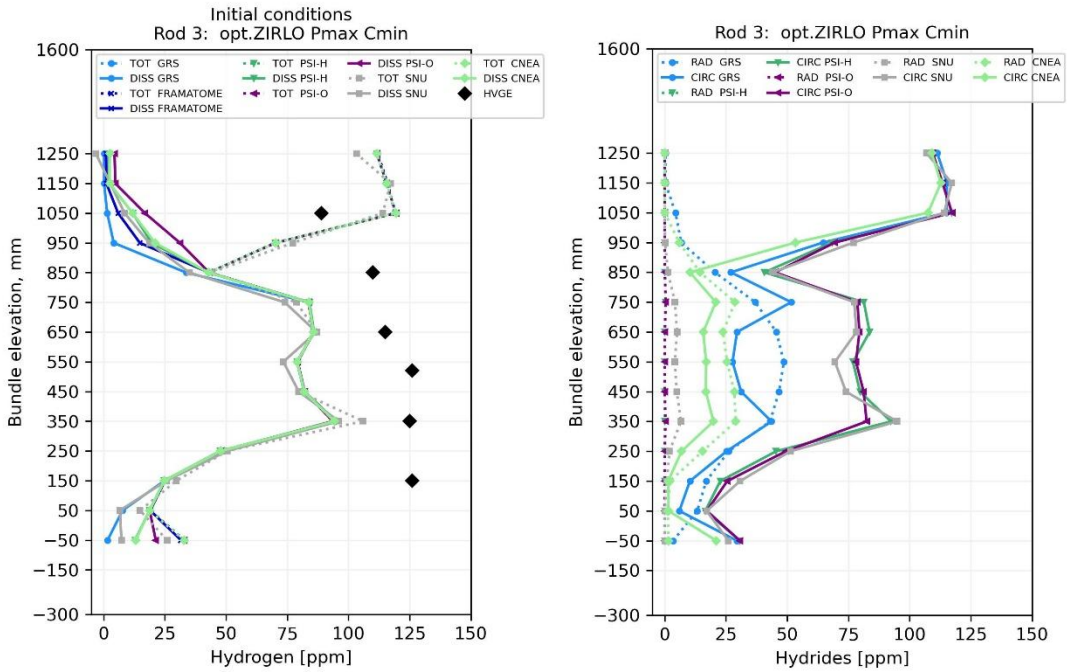

Fig. 3.42 Axial profiles in rod 3 (initial dissolved and total hydrogen vs. HVGE, left) and final radial/circumferential hydride distributions (right)

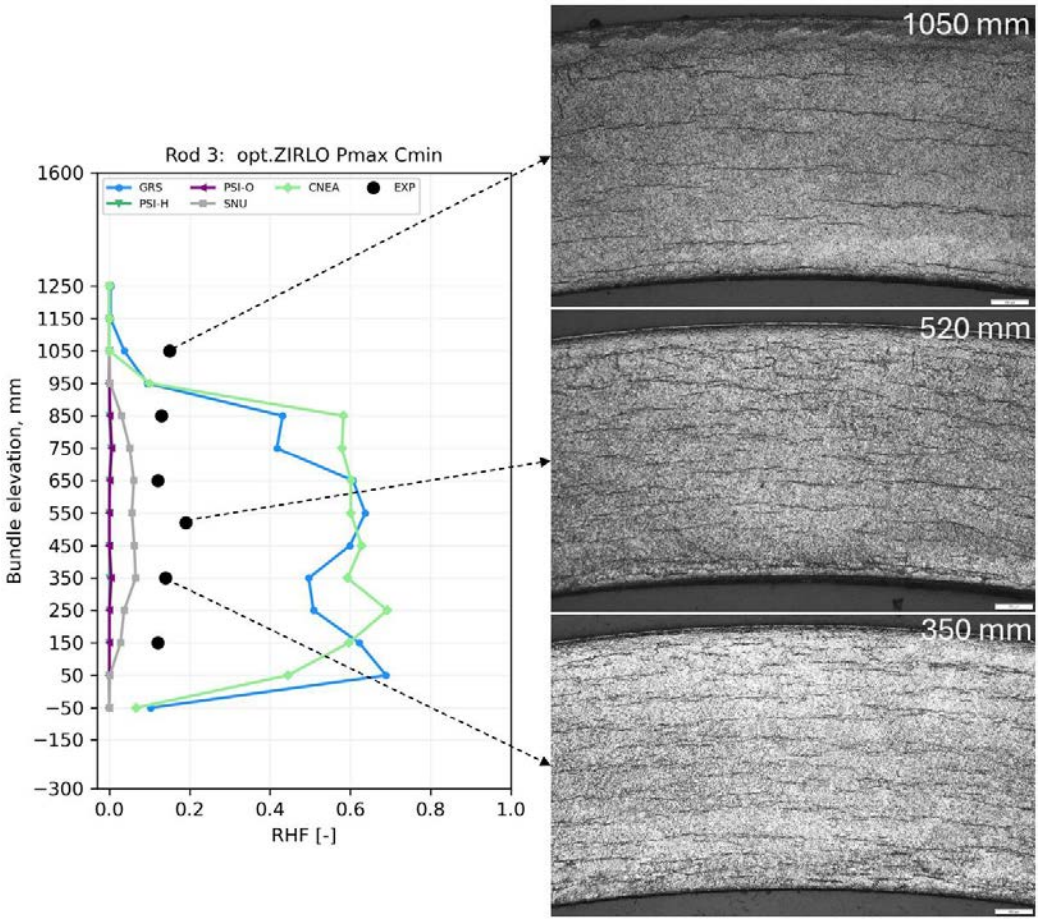

Fig. 3.43 Rod № 3: Radial hydride fraction axial profile vs. post-test metallography

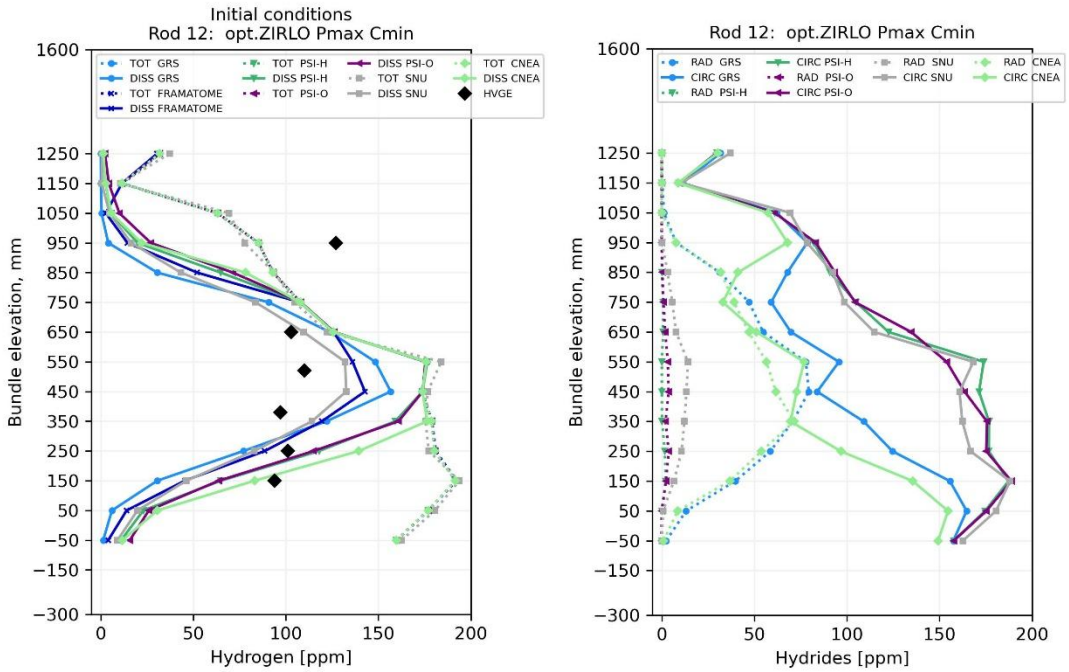

Fig. 3.44 Axial profiles in rod № 12 (initial dissolved and total hydrogen vs. HVGE, left) and final radial/circumferential hydride distributions (right)

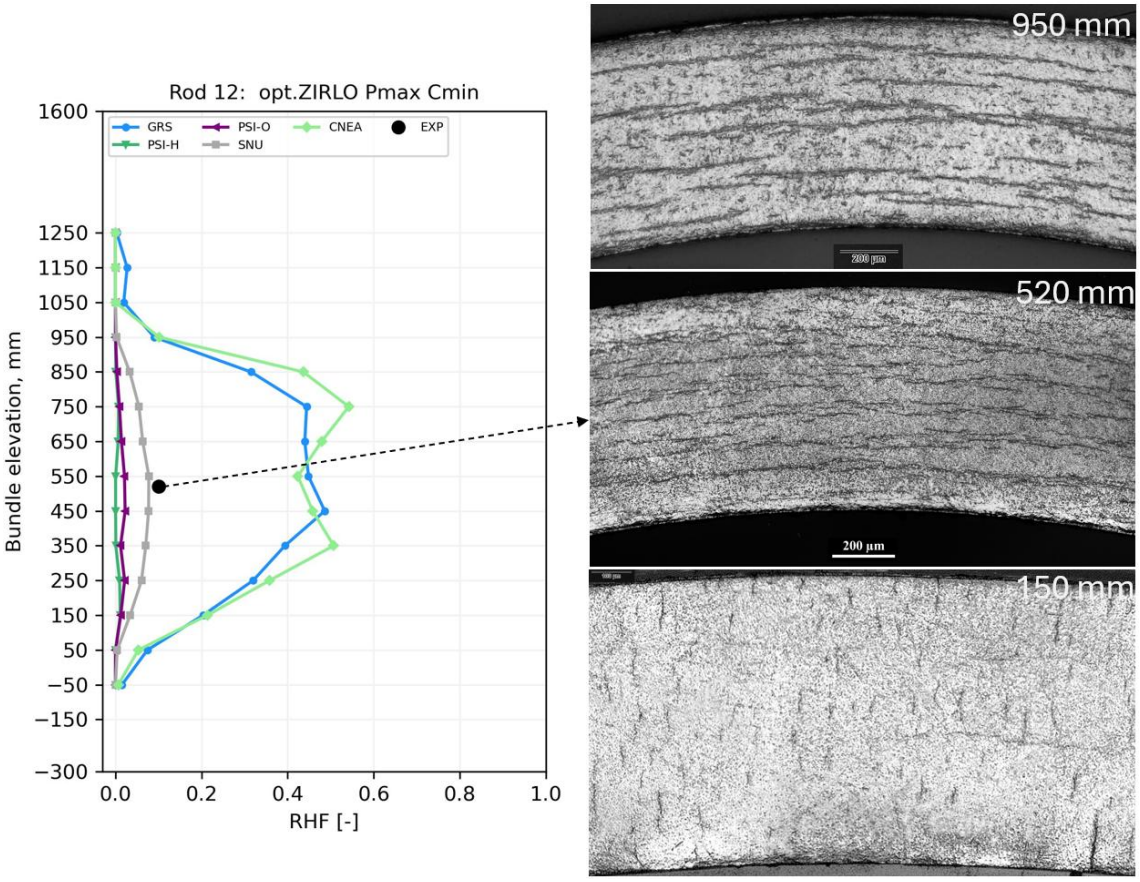

Fig. 3.45 Rod № 12: Radial hydride fraction axial profile vs. post-test metallography

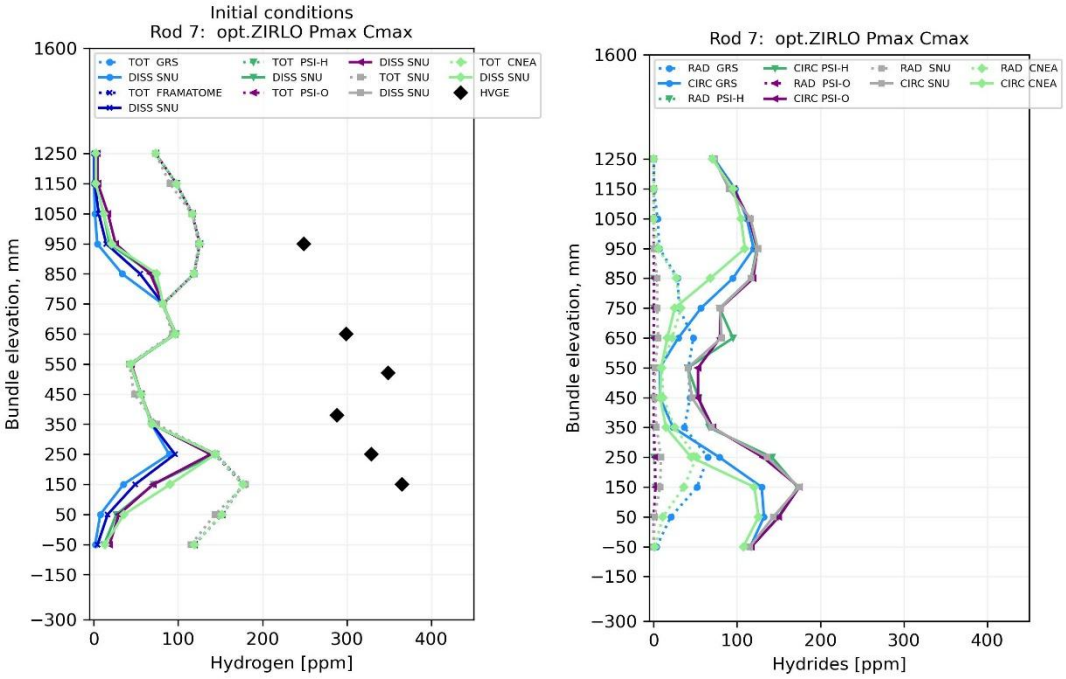

Fig. 3.46 Axial profiles in rod № 7 (initial dissolved and total hydrogen vs. HVGE, left) and final radial/circumferential hydride distributions (right)

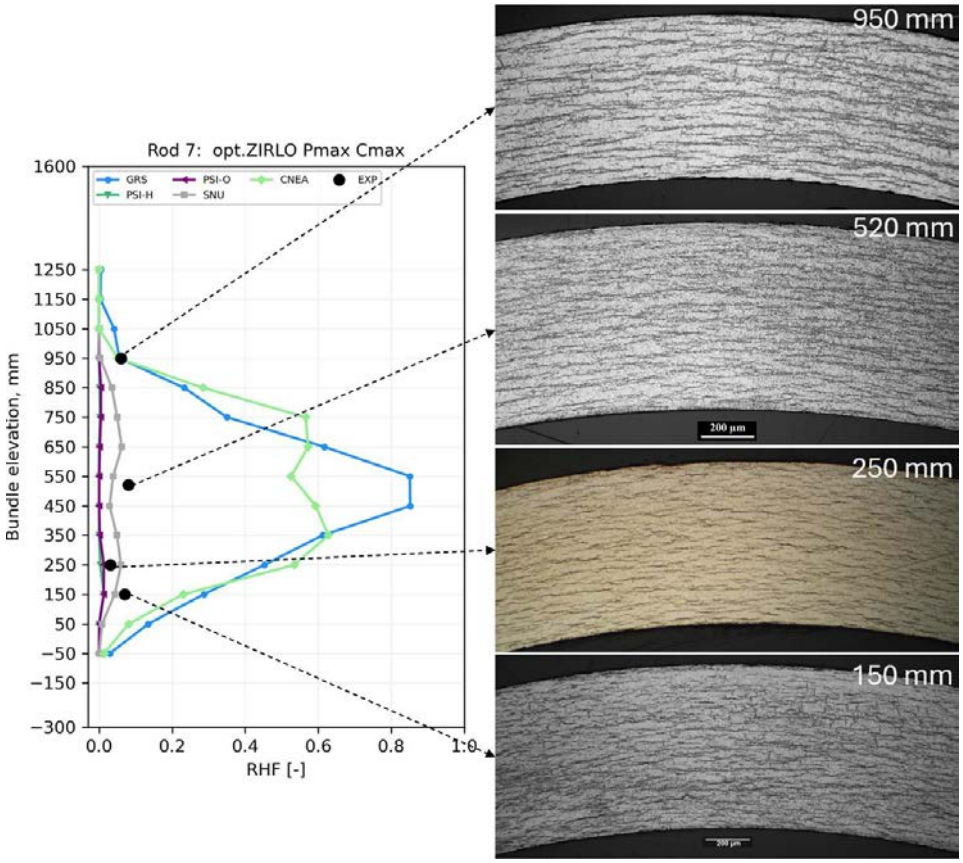

Fig. 3.47 Rod № 7: Radial hydride fraction axial profile vs. post-test metallography

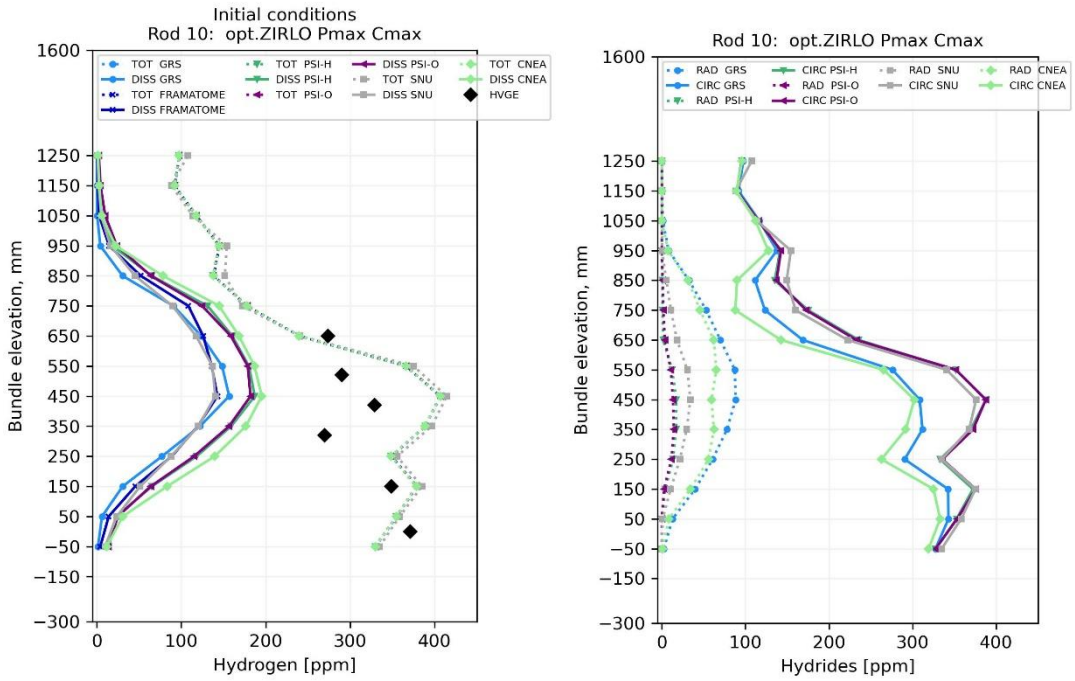

Fig. 3.48 Axial profiles in rod № 10 (initial dissolved and total hydrogen vs. HVGE, left) and final radial/circumferential hydride distributions (right)

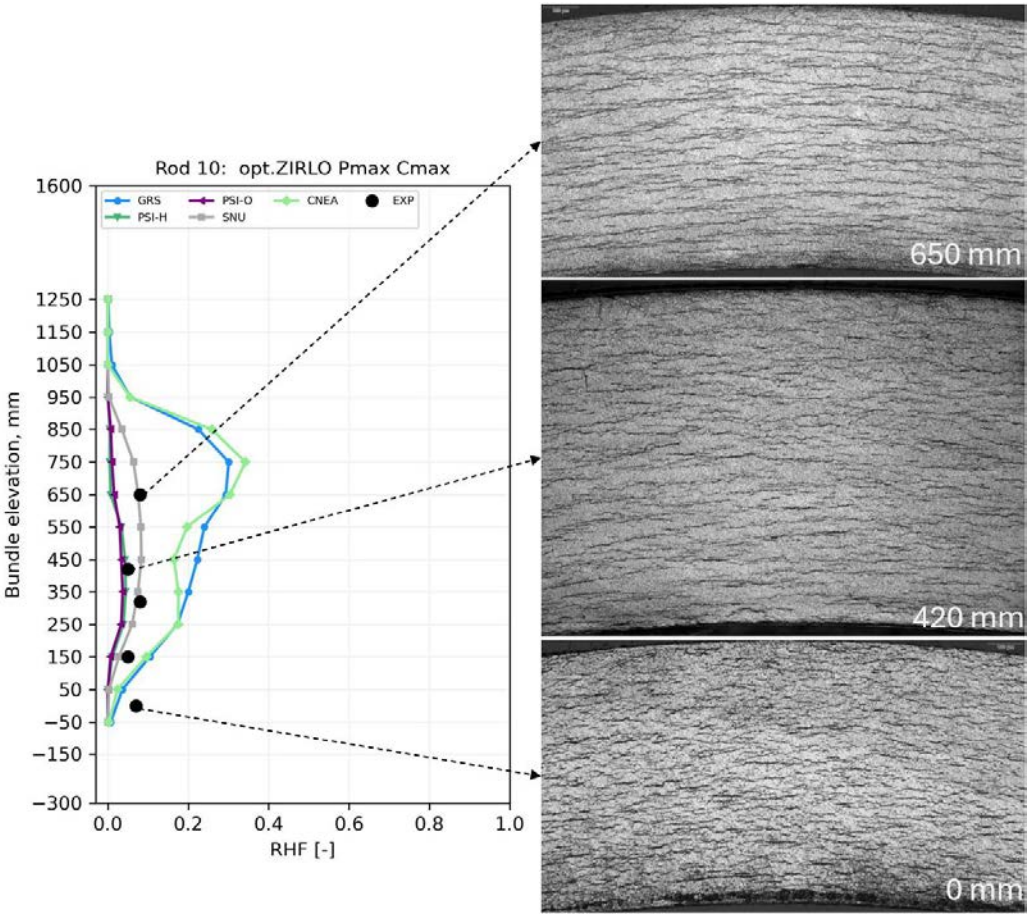

Fig. 3.49 Rod № 10: Radial hydride fraction axial profile vs. post-test metallography

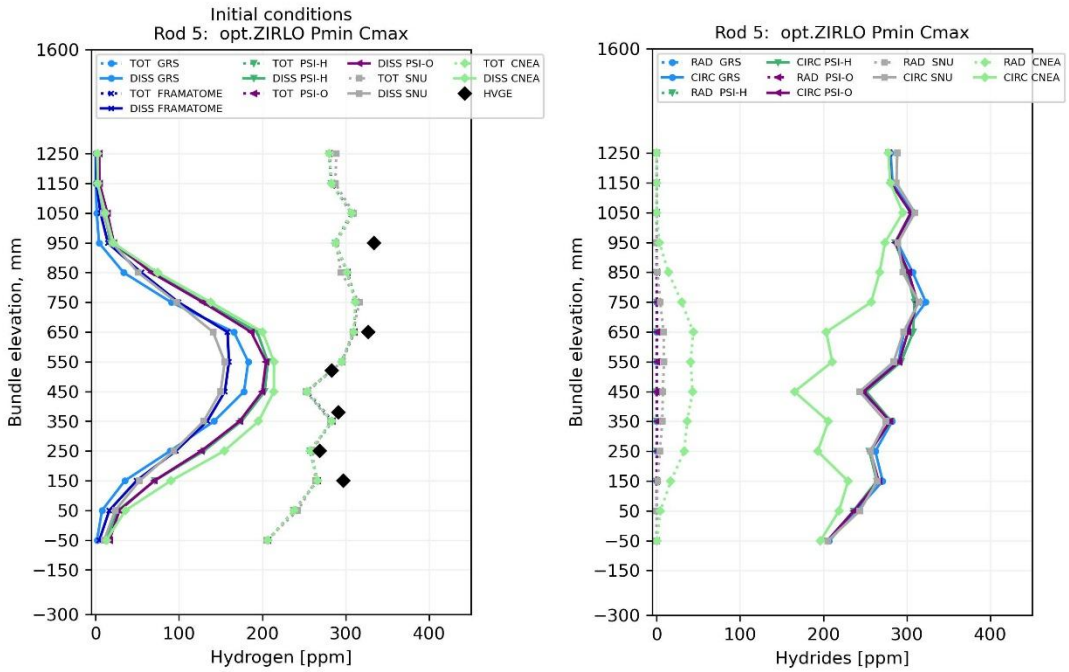

Fig. 3.50 Axial profiles in rod № 5 (initial dissolved and total hydrogen vs. HVGE, left) and final radial/circumferential hydride distributions (right)

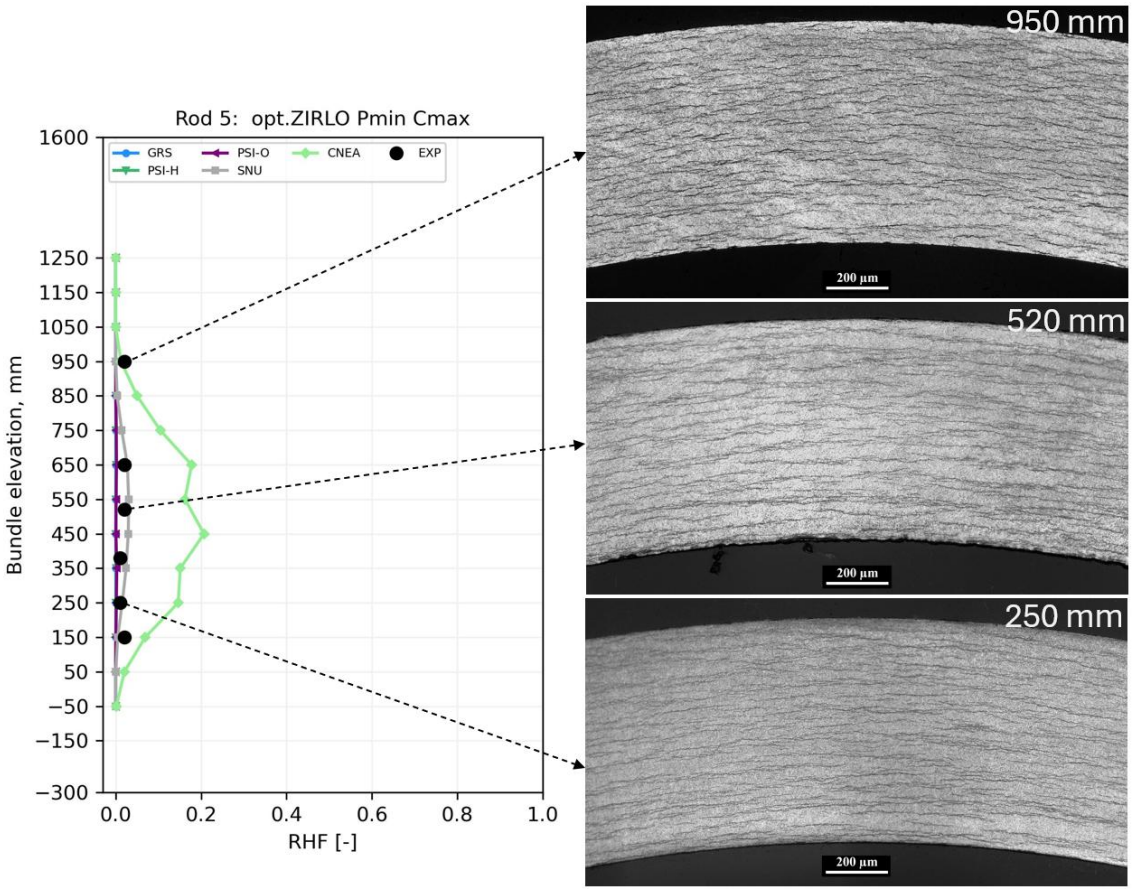

Fig. 3.51 Rod № 5: Radial hydride fraction axial profile vs. post-test metallography

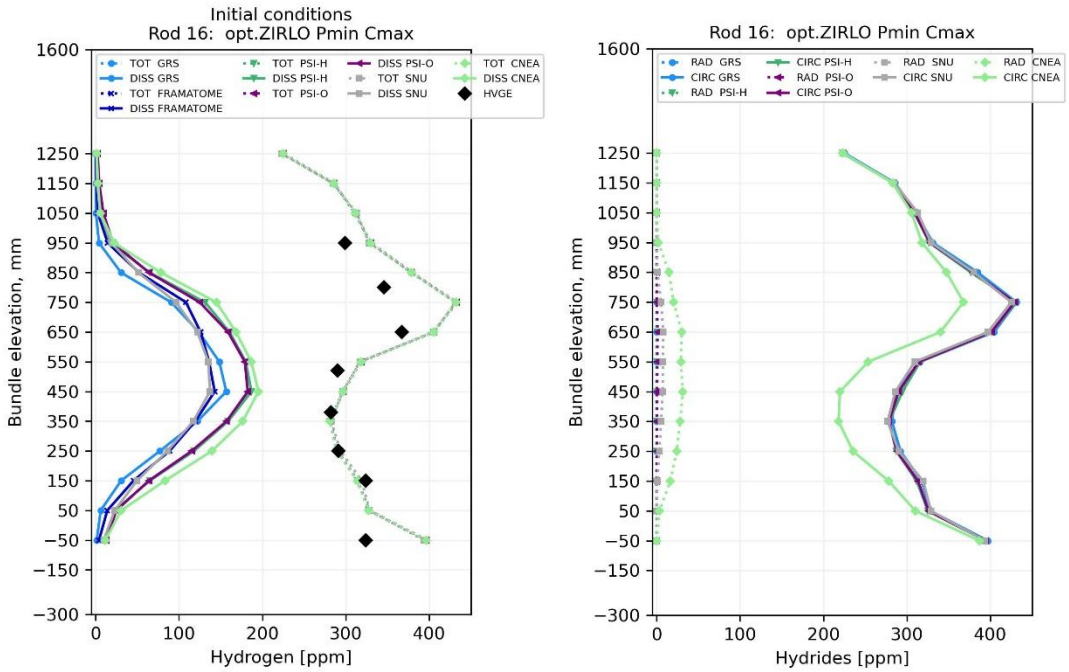

Fig. 3.52 Axial profiles in rod № 16 (initial dissolved and total hydrogen vs. HVGE, left) and final radial/circumferential hydride distributions (right)

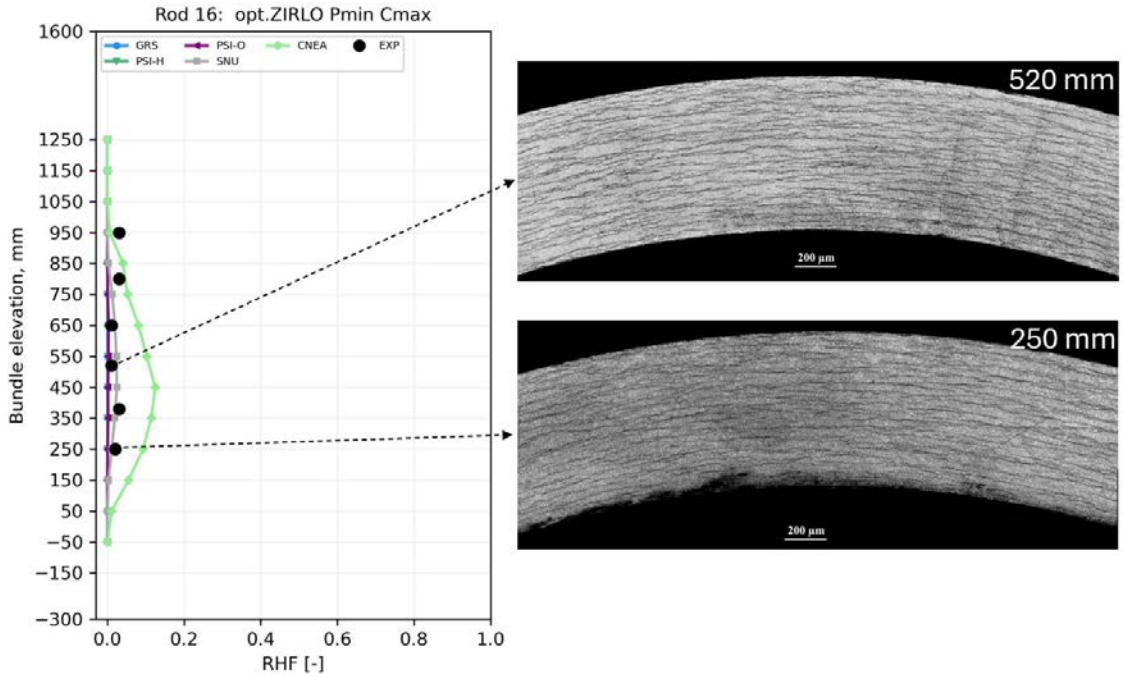

Fig. 3.53 Rod № 16: Radial hydride fraction axial profile vs. post-test metallography

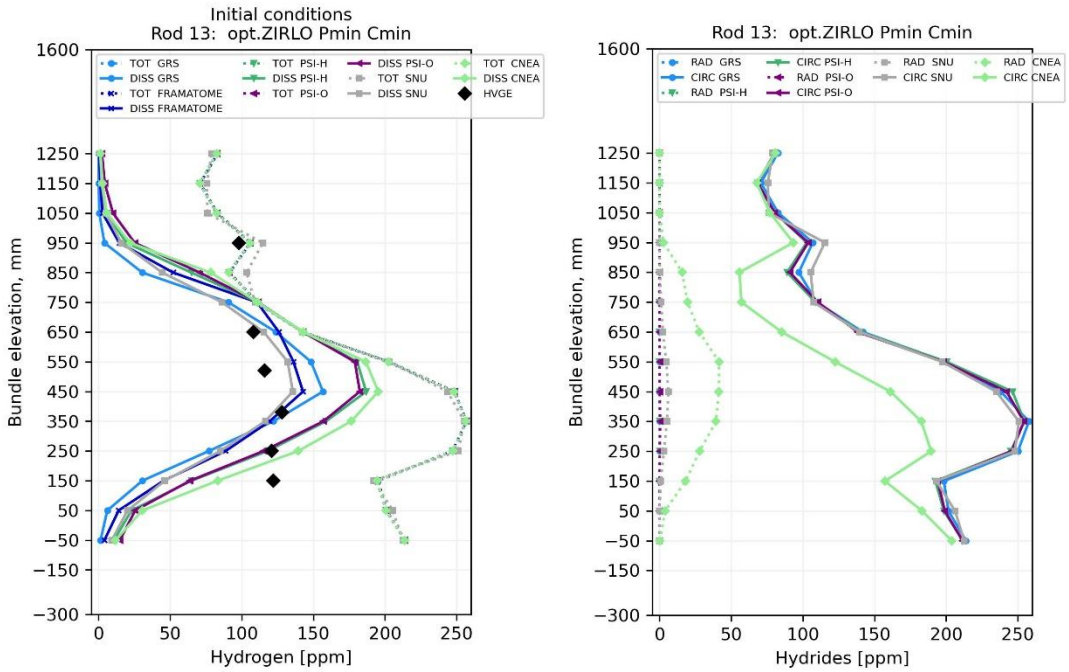

Fig. 3.54 Axial profiles in rod № 13 (initial dissolved and total hydrogen vs. HVGE, left) and final radial/circumferential hydride distributions (right)

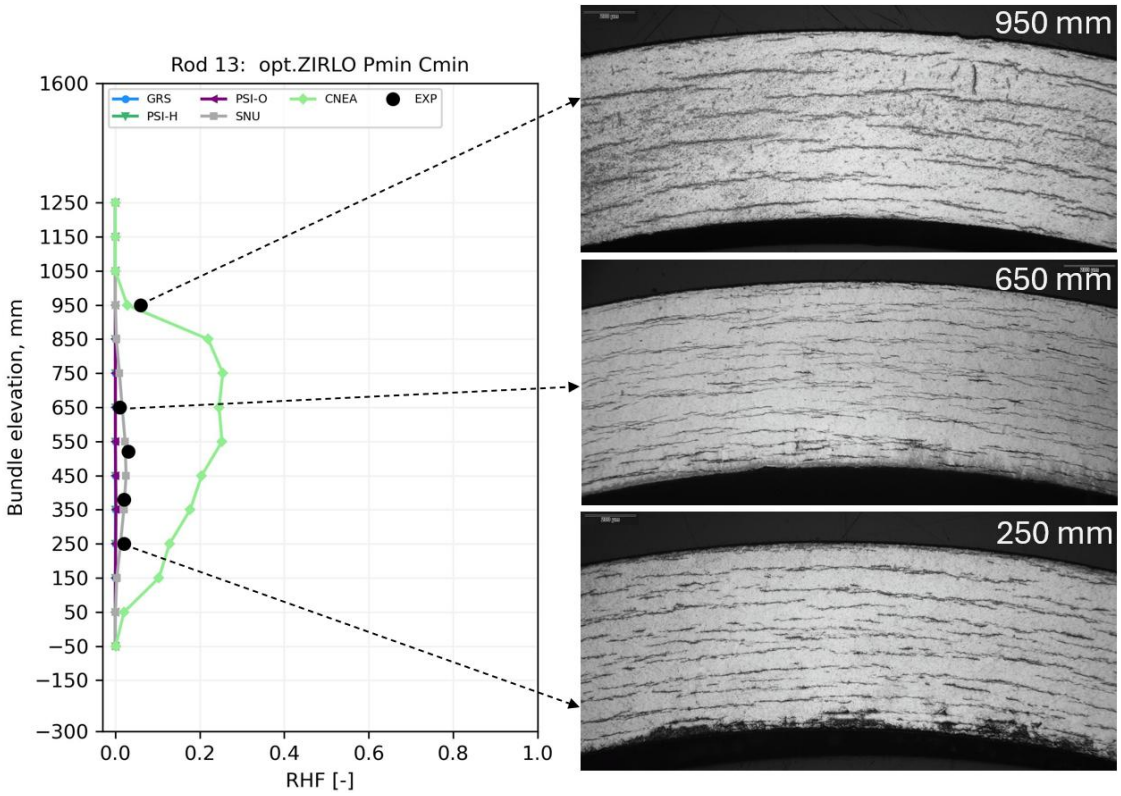

Fig. 3.55 Rod № 13: Radial hydride fraction axial profile vs. post-test metallography

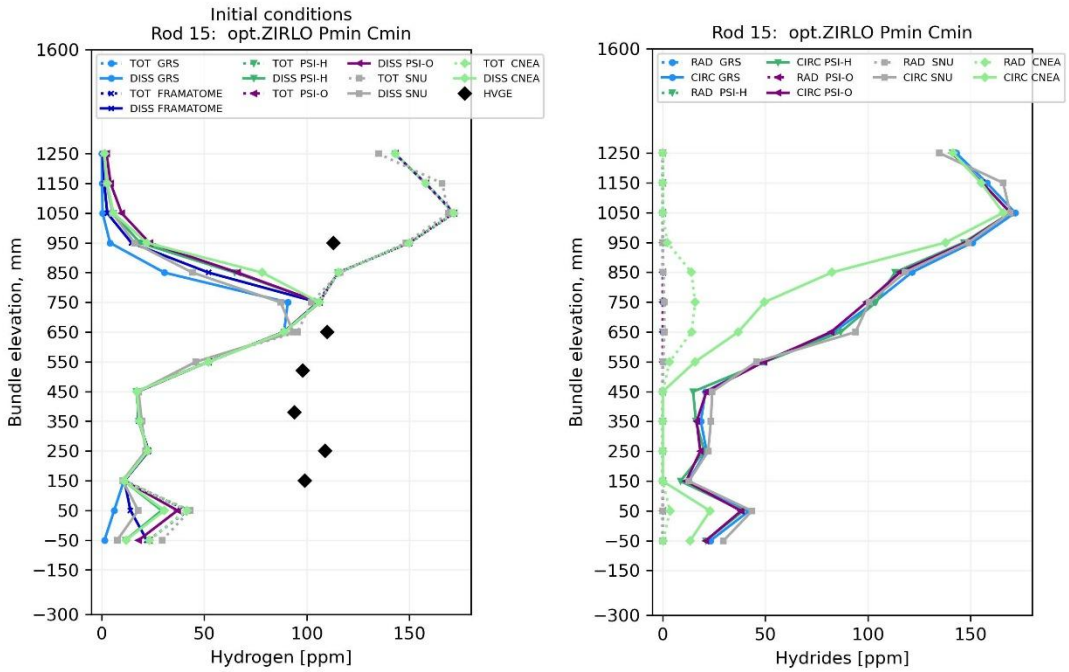

Fig. 3.56 Axial profiles in rod № 15 (initial dissolved and total hydrogen vs. HVGE, left) and final radial/circumferential hydride distributions (right)

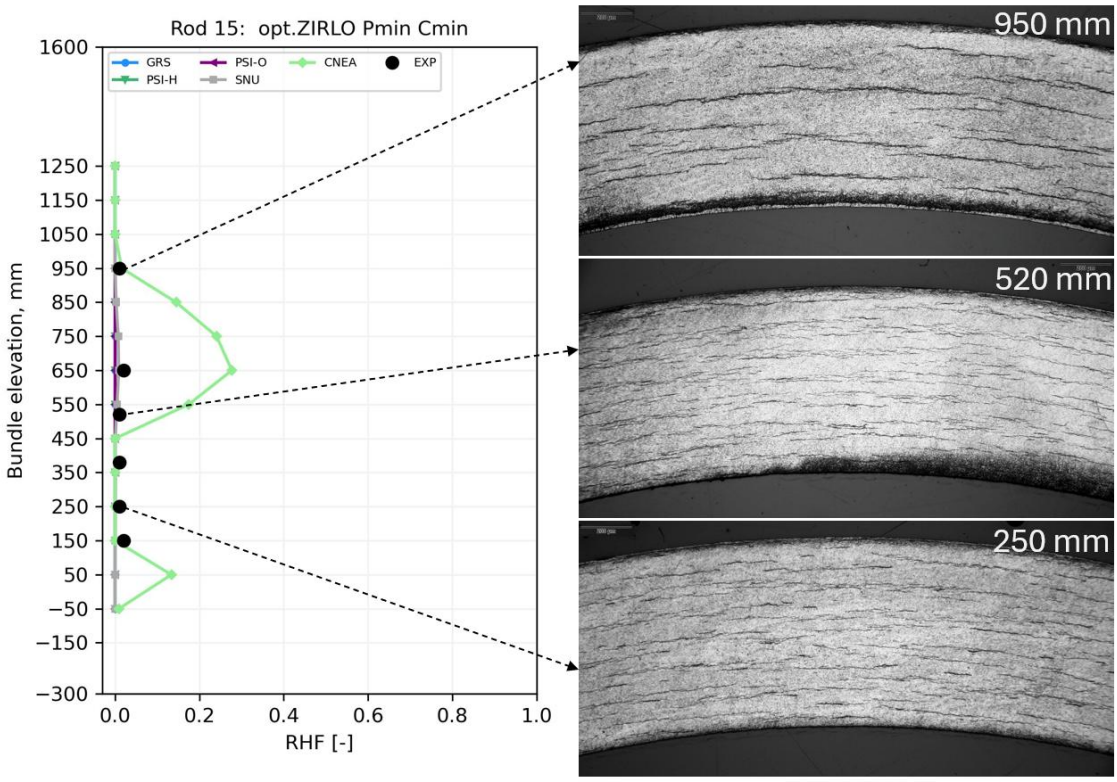

Fig. 3.57 Rod № 15: Radial hydride fraction axial profile vs. post-test metallography

The structure of the summary plots was previously described in the discussion of the Zry-4 cladding results. The radial hydride fraction plotted in Fig. 3.58 as a function of initial temperature indicates higher RHF for Opt.ZIRLO claddings with 100 ppm hydrogen compared to those with 300 ppm. However, this trend applies only to rods at P_{max}, as the RHF is nearly zero for all rods subjected to P_{min}.

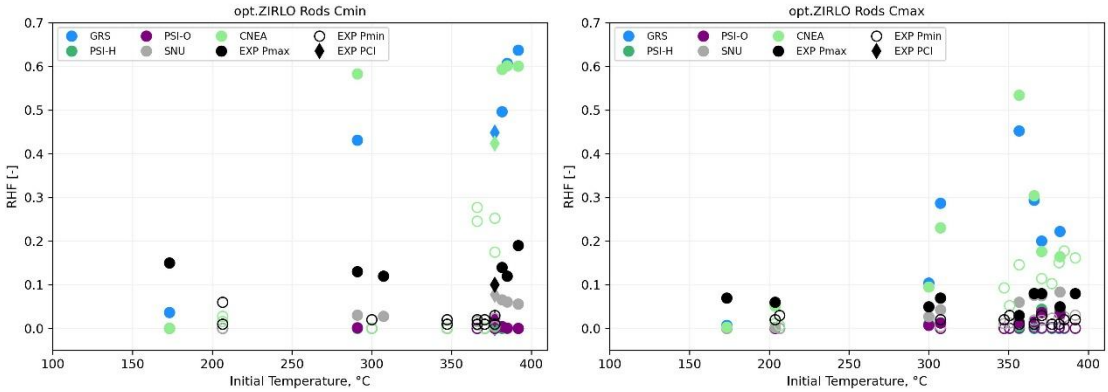

Fig. 3.58 Opt.ZIRLO claddings: RHF vs. initial temperature. Left: C_{min}; Right: C_{max}

The discrepancy between the estimated and measured hydrogen content was most pronounced for Opt.ZIRLO compared to the other cladding materials. This deviation substantially complicates a direct comparison between simulation results and experimental data. Applying a relative tolerance of ± 25 % with respect to the target hydrogen concentration, as done for Zry-4 and DX-D4, would result in the exclusion of nearly all simulated data points. Consequently, the acceptance band was expanded to ± 30 %. As shown in Fig. 3.59, some simulations indicate a decreasing trend in RHF with increasing hydrogen concentration; however, this behavior is captured only qualitatively rather than quantitatively.

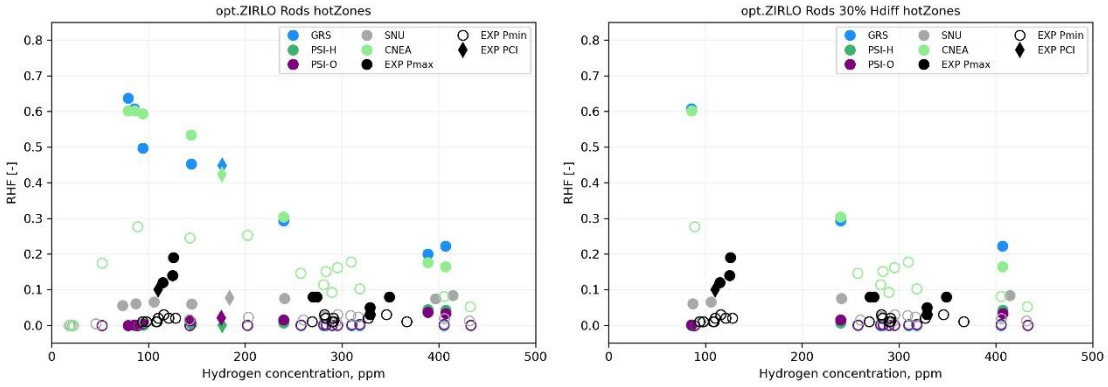

Fig. 3.59 Opt.ZIRLO claddings: RHF vs. initial hydrogen concentration, initial temperature> 350°C. Left: all results; Right: $\left|C_{H,\,HVGE} - C_{H,\,ini}\right| < 30\%\ of C_{H,\,target}$.

4 Conclusions

The benchmark activities conducted within the framework of the SPIZWURZ bundle test provided a comprehensive evaluation of current modeling approaches for creep and hydrogen behavior implemented in existing fuel performance codes. The blind phase, conducted without access to the final experimental data, enabled an unbiased assessment of the predictive capabilities of the participating models. Eleven contributions were submitted by ten participating organizations from seven countries for evaluation and comparison.

As shown in Section 3.1.2, the existing modeling approaches demonstrate a solid capability to predict the creep deformation of unirradiated Zry-4 and DX D4 claddings under dry-storage relevant conditions with sufficient accuracy. However, the comparison clearly indicates that models validated for Zry-4 cannot be directly transferred to other cladding materials without modification. The creep response is significantly influenced by material-specific mechanical properties, requiring proper parameterization and, where necessary, model extensions. For example, accurate predictions for Opt.ZIRLO require adjustments to reflect its overall stronger creep behavior and its higher sensitivity to variations in temperature and pressure.

Concerning hydrogen behavior, a clear material dependence was observed, as outlined in Section 3.2.2. Under comparable conditions, Opt.ZIRLO exhibited practically no radially oriented hydrides, whereas Zry-4 showed a greater tendency toward radial hydride formation. Furthermore, DX D4 showed behavior different from that of Zry-4 claddings, underlining the need to explicitly model both the bulk material and the liner region in order to adequately address the non-uniform hydrogen distribution across the cladding wall thickness.

The simulation approaches were able to qualitatively reproduce certain experimental trends in hydrogen behavior as shown in Section 3.2.2. However, the comparison with experimental results was notably complicated by discrepancies between the estimated hydrogen concentrations used in the simulations and the hydrogen contents measured after the experiment.

Overall, further refinement and enhancement of the modeling approaches are required to improve their predictive capabilities and ensure better alignment with experimental observations. This work will be continued in further benchmark activities.

References

/ALI 23/ Aliev, T., Kolesnik, M.: Evolution of an approach to the modeling of zirconium hydrides morphology based on Monte-Carlo method in 3D representation. Letters on Materials, Vol. 13, No. 2, pp. 143–148, DOI 10.22226/2410-3535-2023-2-143-148, 2023.

/AND 20/ Andersson, B., Anghel, C., Jinnestrand, M.: Dry storage of spent nuclear fuel. Proceedings of 13. International conference on WWER fuel performance, modelling and experimental support, pp. 426–433, 2020.

/BOL 19/ Boldt, F.: Implementation of Hydrogen Solid Solubility Data and Precipitation Threshold Stresses in the Fuel Rod Code TESPA-ROD. Nuclear Engineering and Radiation Science, DOI 10.1115/1.4042118, 2019.

/BOU 05/ Bouffioux, P.: Transportation and Interim Storage of PWR's Spent Fuel. Ed.: Électricité de France (EDF), HT25-C2005-192/PBF, 2005.

/CAP 12/ Cappelaere, C., Limon, R., Duguay, C., Pinte, G., Le Breton, M., Bouffioux, P., Chabretou, V., Miquet, A.: Thermal Creep Model for CWSR Zircaloy-4 Cladding Taking into Account the Annealing of the Irradiation Hardening. Nuclear Technology, Vol. 177, No. 2, pp. 257–272, DOI 10.13182/NT12-A13370, 2012.

/CIN 15/ Cinbiz, N. M., Koss, D. A., Motta, A. T.: The Effect of Stress Biaxiality on Hydride Reorientation Threshold Stress. TopFuel Conference: Zurich, Switzerland, 2015.

/DES 14/ Desquines, J., Drouan, D., Billone, M., Puls, M. P., March, P., Fourgeaud, S., Getrey, C., Elbaz, V., Philippe, M.: Influence of temperature and hydrogen content on stress-induced radial hydride precipitation in Zircaloy-4 cladding. Journal of Nuclear Materials, Vol. 453, No. 1-3, pp. 131–150, DOI 10.1016/j.jnucmat.2014.06.049, 2014.

/EL 24/ El Abdi, A., Jonnet. J., Ambard, A., Ton That, M., Costa, Davide, Idoux L.: SICRAC, a creep simulation tool for the justification of irradiated fuel rod integrity in back-end conditions. Proceedings of TopFuel 2024, 2024.

/FER 11/ Feria, F., Herranz, L. E.: Creep assessment of Zry-4 cladded high burnup fuel under dry storage. Progress in Nuclear Energy, Vol. 53, No. 4, pp. 395–400, DOI 10.1016/j.pnucene.2011.01.012, 2011.

/FER 15/ Feria, F., Herranz, L. E., Penalva, J.: On the way to enabling FRAPCON-3 to model spent fuel under dry storage conditions: The thermal evolution. Annals of Nuclear Energy, Vol. 85, pp. 995–1002, DOI 10.1016/j.anucene.2015.07.017, 2015.

/FER 20/ Feria, F., Aguado, C., Herranz, L. E.: Extension of FRAPCON-xt to hydride radial reorientation in dry storage. Annals of Nuclear Energy, Vol. 145, pp. 107559, DOI 10.1016/j.anucene.2020.107559, 2020.

/GEE 15/ Geelhood, K. J., Luscher, W. G., Raynaud, P. A., Porter, I. E.: FRAPCON-4.0, A Computer Code for the Calculation of Steady-State, Thermal-Mechanical Behavior of Oxide Fuel Rods for High Burnup. Pacific Northwest National Laboratory (PNNL), 2015.

/GON 19/ Gong, W., Trtik, P., Colldeweih, A. W., Duarte, L. I., Grosse, M., Lehmann, E., Bertsch, J.: Hydrogen diffusion and precipitation in duplex zirconium nuclear fuel cladding quantified by high-resolution neutron imaging. Journal of Nuclear Materials, Vol. 526, pp. 151757, DOI 10.1016/j.jnucmat.2019.151757, 2019.

/GRO 25/ Große, M., Herm, M., Kilger, R., Kolesnik, M., Rezchikova, A., Rössger, C., Stuckert, J., Weick, S.: Investigations of the Cladding Behavior under Conditions Simulating Long-Term Dry Storage of Spent Fuel. 21st International Symposium on Zirconium in the Nuclear Industry, April 2025.

/JO 25/ Jo, C., Woo, D., Lee, Y.: Development of an advanced hydride reorientation model for Zircaloy cladding and its experimental validation. Journal of Nuclear Materials, Vol. 603, pp. 155445, DOI 10.1016/j.jnucmat.2024.155445, 2025.

/KAM 96/ Kammenzind, B. F., Franklin, D. G., Peters, H. R., Duffin, W. J.: Hydrogen pickup and redistribution in alpha annealed Zry-4, WAPD-T-304. Ed.: American Society for Testing and Materials (ASTM), Zirconium in the nuclear industry: Eleventh international symposium, No. 244661, 1996.

/KAN 23/ Kang, S., Huang, P.-H., Petrov, V., Manera, A., Ahn, T., Kammenzind, B., Motta, A. T.: Determination of the hydrogen heat of transport in Zircaloy-4. Journal of Nuclear Materials, Vol. 573, pp. 154122, DOI 10.1016/j.jnucmat.2022.154122, 2023.

/KEA 67/ Kearns, J. J.: Terminal Solubility and Partitioning of Hydrogen in the Alpha Phase of Zirconium, Zircaloy-2 and Zircaloy-4. Journal of Nuclear Materials, Vol. 22, pp. 292–303, DOI 10.1016/0022-3115(67)90047-5, 1967.

/KEA 72/ Kearns, J.: Diffusion coefficient of hydrogen in alpha zirconium, Zircaloy-2 and Zircaloy-4. Journal of Nuclear Materials, Vol. 43, No. 3, pp. 330–338, DOI 10.1016/0022-3115(72)90065-7, 1972.

/KIM 14/ Kim, J.-S., Kim, Y.-S.: Effect of thermal history on the terminal solid solubility of hydrogen in Zircaloy-4. International Journal of Hydrogen Energy, Vol. 39, No. 29, pp. 16442–16449, DOI 10.1016/j.ijhydene.2014.08.018, 2014.

/KIM 15/ Kim, Y.-J., Kook, D.-H., Kim, T.-H., Kim, J.-S.: Stress and temperature-dependent hydride reorientation of Zircaloy-4 cladding and its effect on the ductility degradation. Journal of Nuclear Science and Technology, Vol. 52, No. 5, pp. 717–727, DOI 10.1080/00223131.2014.978829, 2015.

/KIM 20/ Kim, J.-S., Kim, T.-H., Kim, K., Kim, Y.-S.: Terminal solid solubility of hydrogen of optimized-Zirlo and its effects on hydride reorientation mechanisms under dry storage conditions. Nuclear Engineering and Technology, Vol. 52, No. 8, pp. 1742–1748, DOI 10.1016/j.net.2020.01.022, 2020.

/KOL 18/ Kolesnik, M., Aliev, T., Likhanskii, V.: Modeling of hydrogen behavior in spent fuel claddings during dry storage. Journal of Nuclear Materials, Vol. 508, pp. 567–573, DOI 10.1016/j.jnucmat.2018.06.012, 2018.

/KOL 23/ Kolesnik, M. Y., Aliev, T. N.: Evaluating the Spatial and Size Distributions of Flat Precipitates in Diffusion-Controlled Precipitation Processes. Physics of Metals and Metallography, Vol. 124, No. 13, pp. 1414–1425, DOI 10.1134/S0031918X22602074, 2023.

/KOL 26/ Kolesnik, M., Stuckert, J., Grosse, M., Weick, S.: Hydride morphology in zirconium cladding tubes after the SPIZWURZ bundle test. Part I: analysis of experimental data. Journal of Nuclear Materials, Vol. 619, pp. 156250, DOI 10.1016/j.jnucmat.2025.156250, 2026.

/LAC 18/ Lacroix, E., Motta, A. T., Almer, J. D.: Experimental Determination of Zirconium Hydride Precipitation and Dissolution in Zirconium Alloy. Journal of Nuclear Materials, No. 509, pp. 162–167, DOI 10.1016/j.jnucmat.2018.06.038, 2018.

/LAC 19/ Lacroix, E.: Modeling zirconium hydride precipitation and dissolution in zirconium alloys, Dissertation. Pennsylvania State University (PSU), 2019.

/LAS 92/ Lassmann, K.: TRANSURANUS: a fuel rod analysis code ready for use. Journal of Nuclear Materials, Vol. 188, pp. 295–302, DOI 10.1016/0022-3115(92)90487-6, 1992.

/LIM 96/ Limbäck, M., Andersson, T.: A Model for Analysis of the Effect of Final Annealing on the In- and Out-of-Reactor Creep Behavior of Zircaloy Cladding. In: Bradley, E. R., Sabol, G. P. (Eds.): Zirconium in the Nuclear Industry: Eleventh International Symposium. pp. 448–468, ISBN 0-8031-2406-6, DOI 10.1520/STP16185S, ASTM International100 Barr Harbor Drive, PO Box C700, West Conshohocken, PA 19428-2959, 1996.

/MAL 12/ Mallipudi, V., Valance, S., Bertsch, J.: Meso-scale analysis of the creep behavior of hydrogenated Zircaloy-4. Mechanics of Materials, Vol. 51, pp. 15–28, DOI 10.1016/j.mechmat.2012.03.003, 2012.

/MAR 72/ Marino, G. P.: A Numerical Calculation of the Redistribution of an Interstitial Solute in a Thermal Gradient. Nuclear Science and Engineering, Vol. 49, No. 1, pp. 93–98, DOI 10.13182/NSE72-A22530, 1972.

/MAR 74/ Marino, G. P.: HYDIZ: A 2-dimensonal computer program for migration of interstitial solutes of finite solubility in a thermal gradient. Bettis Atomic Power Lab., Pittsburgh, PA (USA): United States, 1974.

/PAS 20/ Passelaigue, F., Lacroix, E., Pastore, G., Motta, A. T.: Implementation and Validation of the Hydride Nucleation-Growth-Dissolution (HNGD) model in BISON. Journal of Nuclear Materials, DOI 10.1016/j.jnucmat.2020.152683, 2020.

/PAS 22/ Passelaigue, F., Simon, P.-C. A., Motta, A. T.: Predicting the hydride rim by improving the solubility limits in the Hydride Nucleation-Growth-Dissolution (HNGD) model. Journal of Nuclear Materials, Vol. 558, pp. 153363, DOI 10.1016/j.jnucmat.2021.153363, 2022.

/RAS 05/ Rashid, J., Machiels, A.: Hydride Precipitation in Spent Fuel Cladding during Storage. The 10th International Conference on Environmental Remediation and Radioactive Waste Management, 2005.

/REZ 24/ Rezchikova, A., Stuckert, J.: SPIZWURZ Benchmark Phase 1: Blind Benchmark Specification. Gesellschaft für Anlagen- und Reaktorsicherheit (GRS), 3. ed., 2024.

/SAB 94/ Sabol, G. P., Comstock, R. J., Weiner, R. A., Larouere, P., Stanutz, R. N.: In-Reactor Corrosion Performance of ZIRLO™ and Zircaloy-4. In: Garde, A. M., Bradley, E. R. (Eds.): Zirconium in the Nuclear Industry: Tenth International Symposium. pp. 724–744, ISBN 0-8031-2011-7, DOI 10.1520/STP15217S, ASTM International100 Barr Harbor Drive, PO Box C700, West Conshohocken, PA 19428-2959, 1994.

/SAP 25/ Sappl, J., Rezchikova, A., Kilger, R.: Capabilities, Recent Developments, and Validation Status of the TESPA-ROD Fuel Performance Code for Nuclear Reactor Safety Analysis. In: American Nuclear Society (ANS) (Ed.): Nuclear Reactor Fuel Performance Conference (TopFuel) 2025. TopFuel 2025, Nashville, Tennessee, USA, 5. - 9. October 2025, 2025.

/SCO 20/ Scolaro, A., Clifford, I., Fiorina, C., Pautz, A.: The OFFBEAT multi-dimensional fuel behavior solver. Nuclear Engineering and Design, Vol. 358, pp. 110416, DOI 10.1016/j.nucengdes.2019.110416, 2020.

/SIM 21/ Simon, P.-C. A., Frank, C., Chen, L.-Q., Daymond, M. R., Tonks, M. R., Motta, A. T.: Quantifying the effect of hydride microstructure on zirconium alloys embrittlement using image analysis. Journal of Nuclear Materials, Vol. 547, pp. 152817, DOI 10.1016/j.jnucmat.2021.152817, 2021.

/SPI 97/ Spilker, H., Peehs, M., Dyck, H.-P., Kaspar, G., Nissen, K.: Spent LWR fuel dry storage in large transport and storage casks after extended burnup. Journal of Nuclear Materials, Vol. 250, No. 1, pp. 63–74, DOI 10.1016/S0022-3115(97)00209-2, 1997.

/STE 25/ Steinbrück, M. (Ed.): 30th International Quench Workshop. Karlsruhe Institute of Technology (KIT), Karlsruhe, 16. - 18. December 2025, 2025.

/STU 23/ Stuckert, J., Rössger, C., Moch, J., Grosse, M., Weick, S.: Hydrogenation of claddings in the new developed HOKI oven and performance of the long-term bundle test under dry storage conditions in the framework of the SPIZWURZ project. DOI 10.5445/IR/1000168767, Karlsruher Institut für Technologie (KIT), 2023.

/SUB 22/ Subcommittee B10.02 on Zirconium and Hafnium: Standard Specification for Wrought Zirconium Alloy Seamless Tubes for Nuclear Reactor Fuel Cladding. B811-13(2022)e1, DOI 10.1520/B0811-13R22E01, ASTM International: West Conshohocken, PA, 2022.

/TOR 14/ Torres, E., Desquines, J., Baietto, M.-C., Coret, M., Wehling, F., Blat-Trieix, M., Ambard, A.: Adsorption and diffusion of hydrogen in Zircaloy-4. Fontevraud 8- Contribution of materials investigations and operating experience to LWR’s safety, performance and reliability, 2014.

/UNI 18/ United States Department of Energy: Three Dimensional Fuel Pin Model Validation by Prediction of Hydrogen Distribution in Cladding and Comparison With Experiment. DOE Nuclear Energy University Program (NEUP), Project No. 13-5180, 2018.

/YAG 15/ Yagnik, S.: Fuel Analysis and Licensing Code: FALCON MOD01: Verification and Validation. Electric Power Research Institute (EPRI), No. 1011308, 2015.

/ZAN 12/ Zanellato, O., Preuss, M., Buffiere, J.-Y., Ribeiro, F., Steuwer, A., Desquines, J., Andrieux, J., Krebs, B.: Synchrotron diffraction study of dissolution and precipitation kinetics of hydrides in Zircaloy-4. Journal of Nuclear Materials, Vol. 420, No. 1-3, pp. 537–547, DOI 10.1016/j.jnucmat.2011.11.009, 2012.

/ZEM 21/ Zemek, M. e. A.: Effects of the liner on ductility of claddings after dry storage. Proceedings of TopFuel 2021, 2021.

/ZHA 17/ Zhang, Y., Jiang, C., Bai, X.: Anisotropic hydrogen diffusion in α-Zr and Zircaloy predicted by accelerated kinetic Monte Carlo simulations. Scientific reports, Vol. 7, pp. 41033, DOI 10.1038/srep41033, 2017.

List of Figures

List of Tables

A SPIZWURZ Bundle Test: Cladding Temperature Recordings

The cladding temperature recordings during the experiment for rods № 1, № 5, and № 14 are presented in Fig. A. 1 - Fig. A. 3, respectively, for each axial zone. The original unfiltered experimental data are shown on the left, and the filtered temperature data are shown on the right.

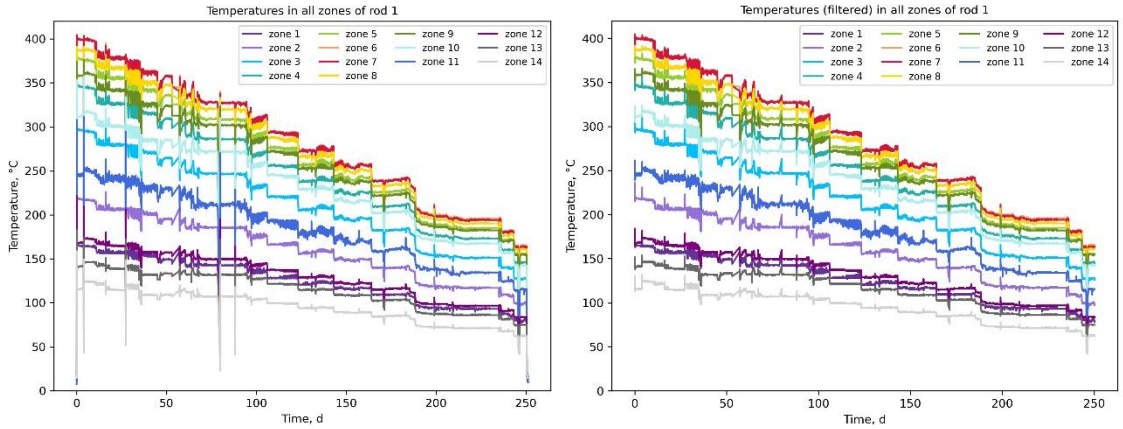

Fig. A. 1 Temperature recordings in Rod № 1: raw (left) vs. filtered (right)

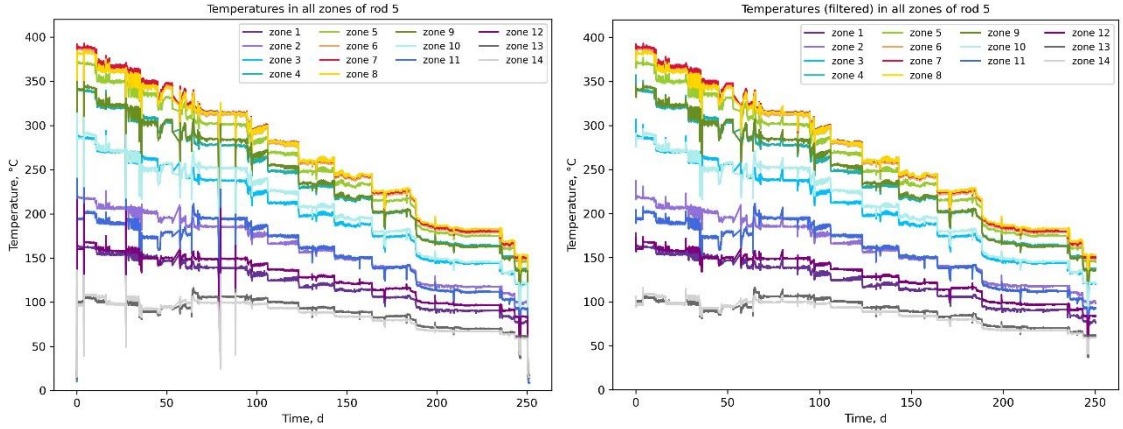

Fig. A. 2 Temperature recordings in Rod № 5: raw (left) vs. filtered (right)

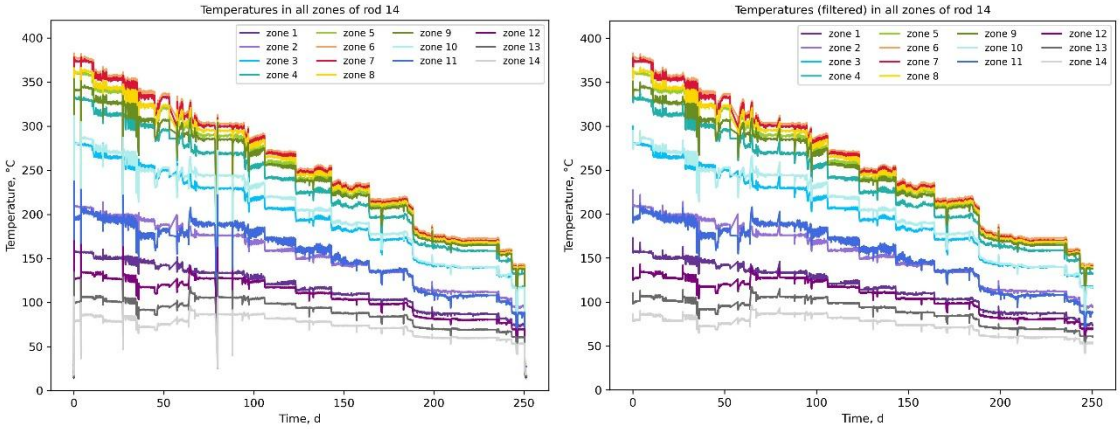

Fig. A. 3 Temperature recordings in Rod № 14: raw (left) vs. filtered (right)

B SPIZWURZ Bundle Test: Hydrogen Concentration in Claddings

The axial hydrogen distribution profiles for all bundle rods except rod N18 are shown in Figures Fig. B. 1–Fig. B. 10. The initial (pre-test) hydrogen concentrations, estimated from the diameter increase caused by hydrogen loading, are represented by light blue dots. The post-experimental measurements obtained by hot vacuum gas extraction are indicated by dark blue diamonds (HVGE). For the benchmark calculation, the initial hydrogen concentration is based on the zone-averaged estimated values, shown as a solid blue line.

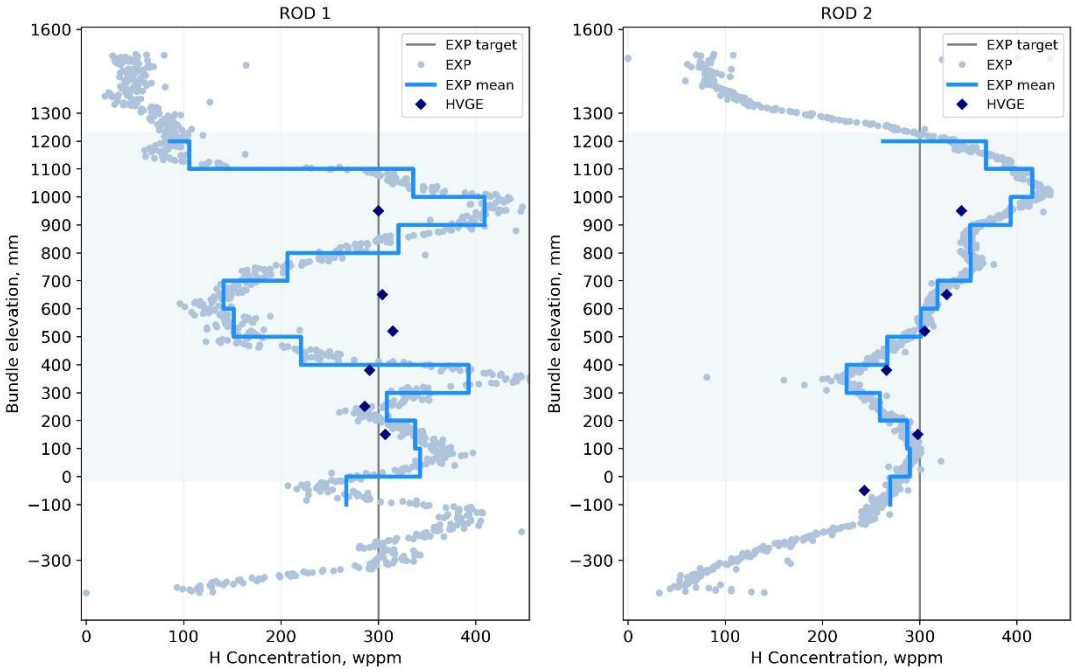

Fig. B. 1 Axial hydrogen distribution in rods № 1 (left) and № 2 (right): estimates vs. HVGE

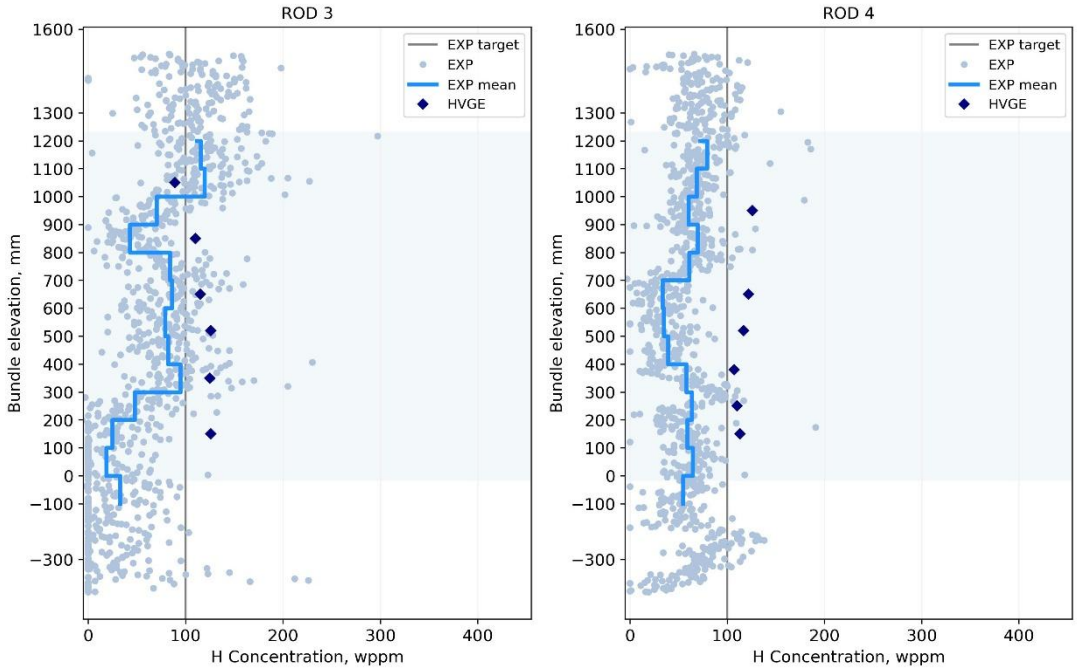

Fig. B. 2 Axial hydrogen distribution in rods № 3 (left) and № 4 (right): estimates vs. HVGE

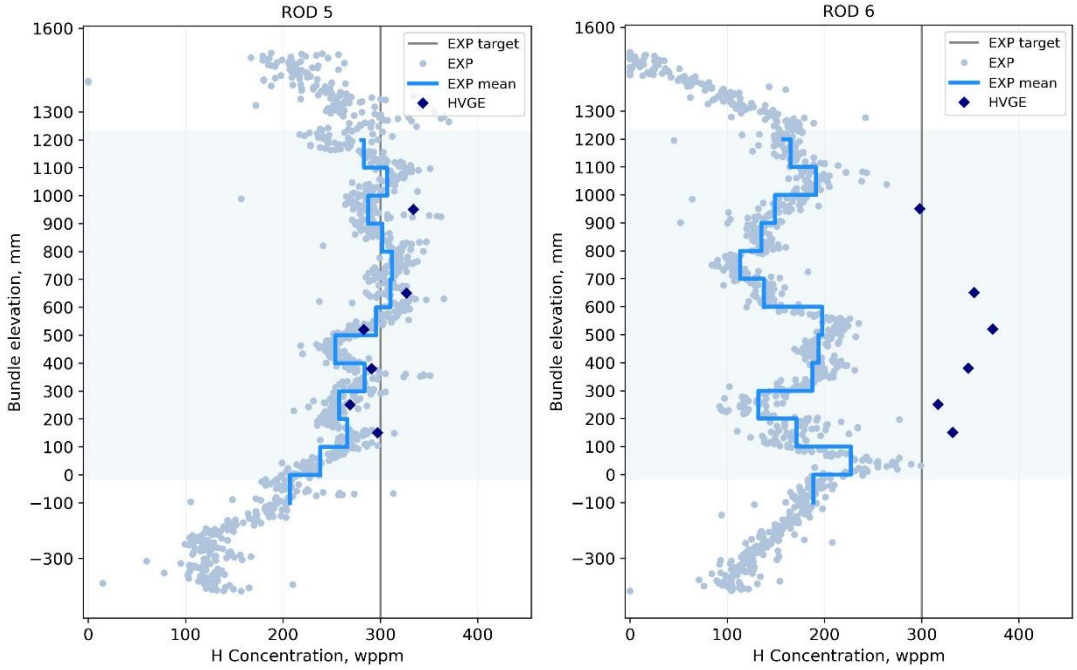

Fig. B. 3 Axial hydrogen distribution in rods № 5 (left) and № 6 (right): estimates vs. HVGE

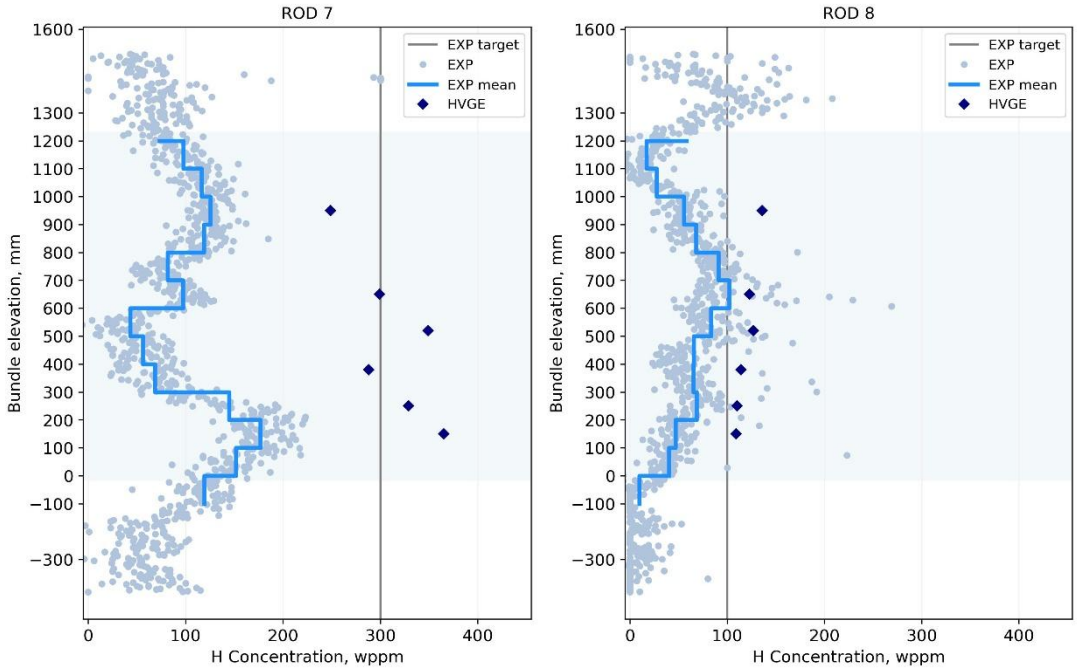

Fig. B. 4 Axial hydrogen distribution in rods № 7 (left) and № 8 (right): estimates vs. HVGE

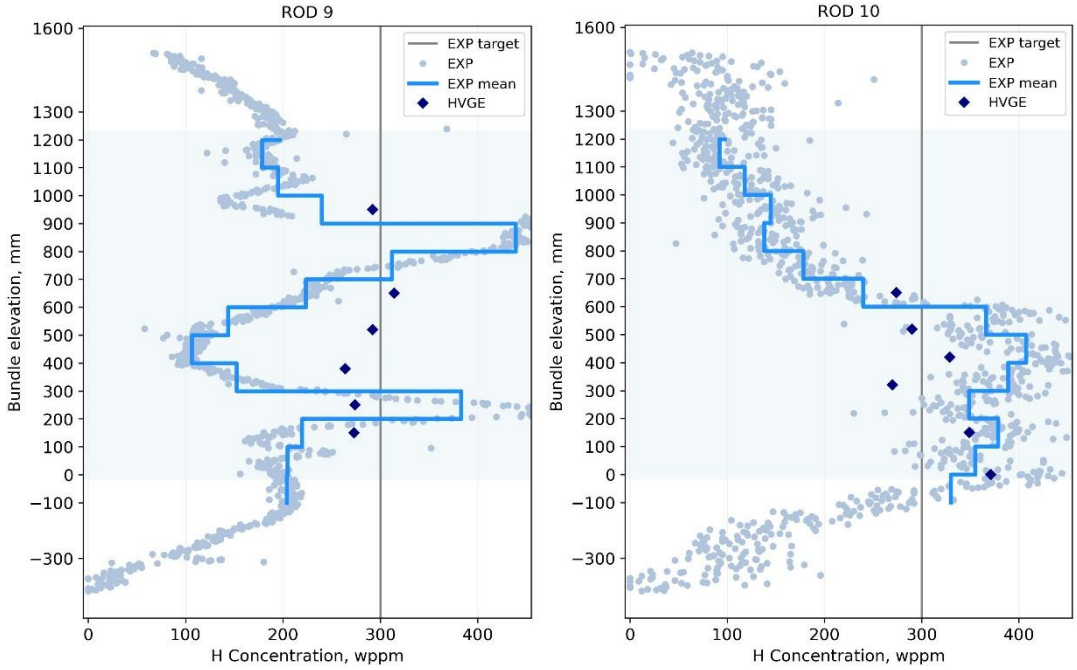

Fig. B. 5 Axial hydrogen distribution in rods № 9 (left) and № 10 (right): estimates vs. HVGE

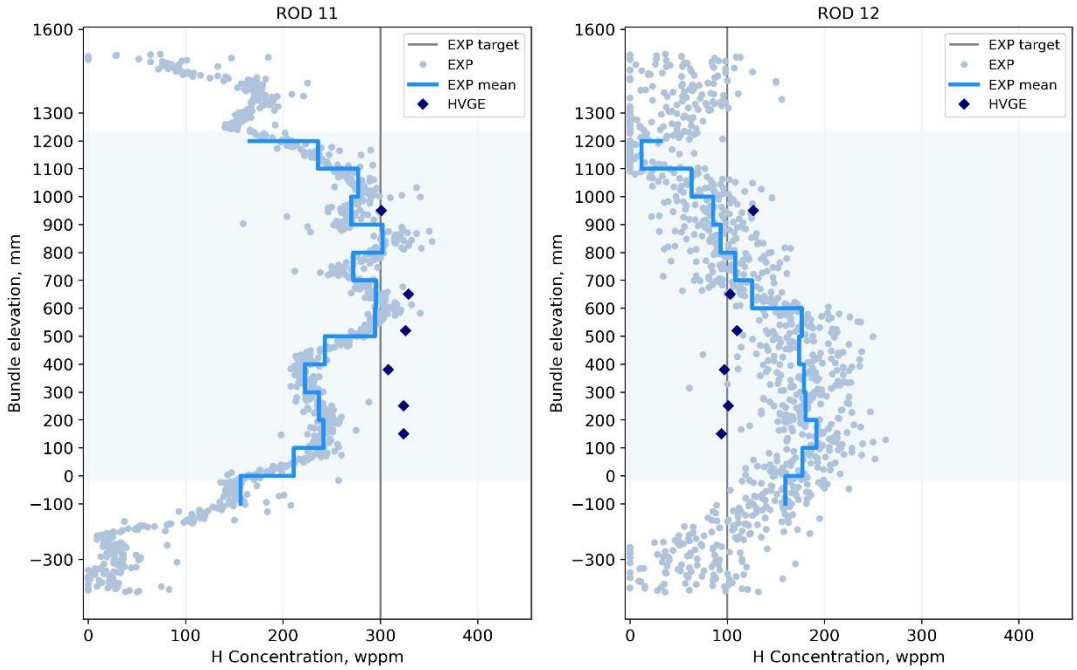

Fig. B. 6 Axial hydrogen distribution in rods № 11 (left) and № 12 (right): estimates vs. HVGE

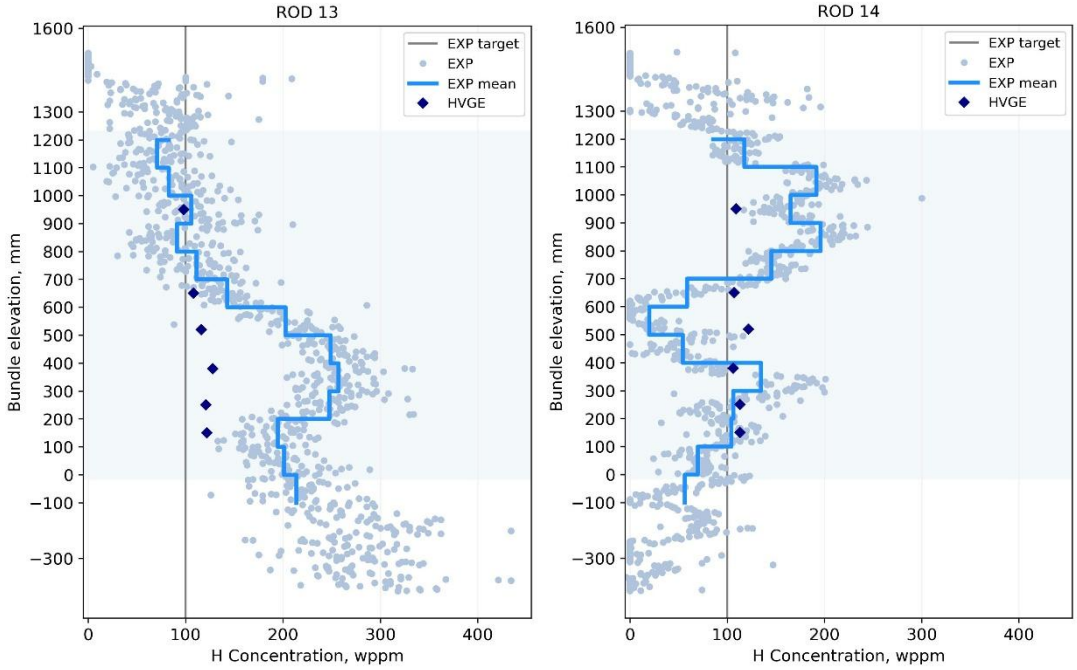

Fig. B. 7 Axial hydrogen distribution in rods № 13 (left) and № 14 (right): estimates vs. HVGE

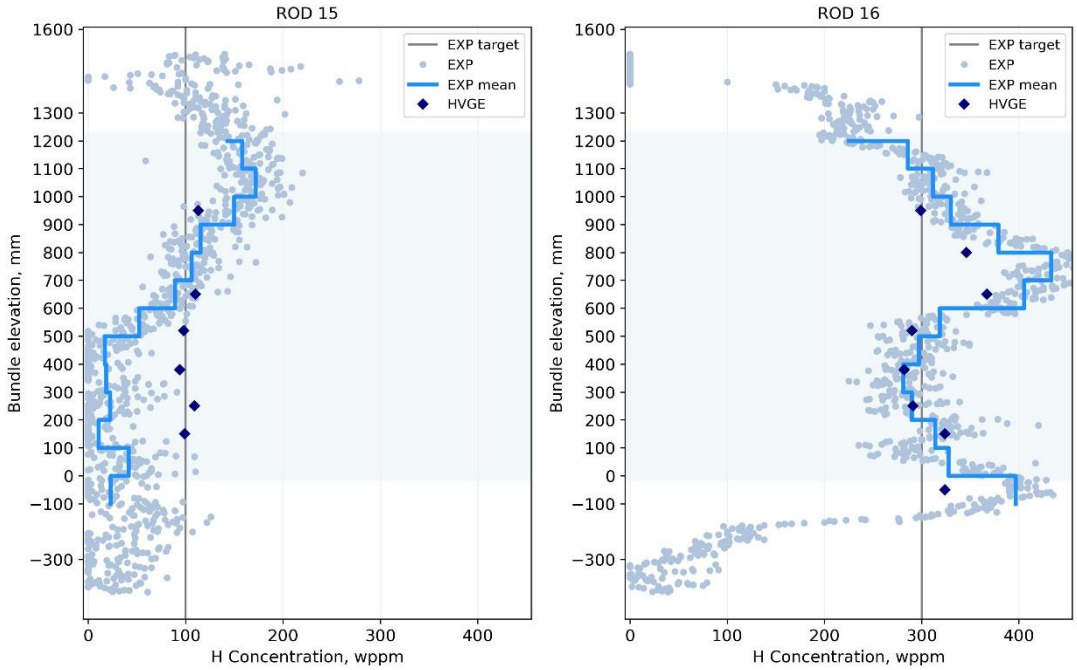

Fig. B. 8 Axial hydrogen distribution in rods № 15 (left) and № 16 (right): estimates vs. HVGE

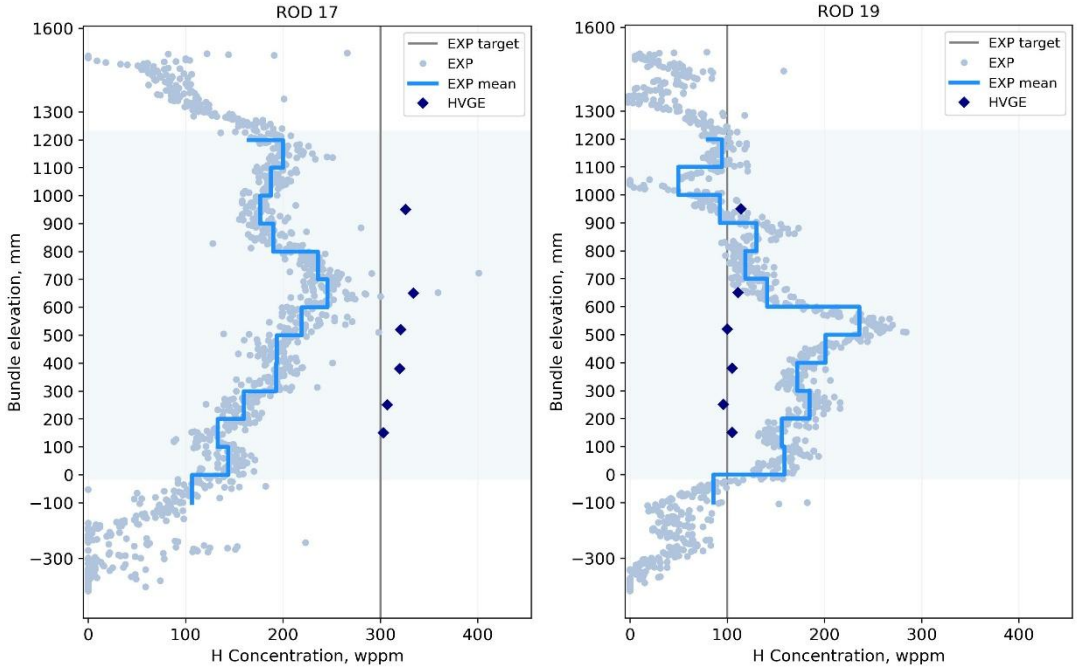

Fig. B. 9 Axial hydrogen distribution in rods № 17 (left) and № 19 (right): estimates vs. HVGE

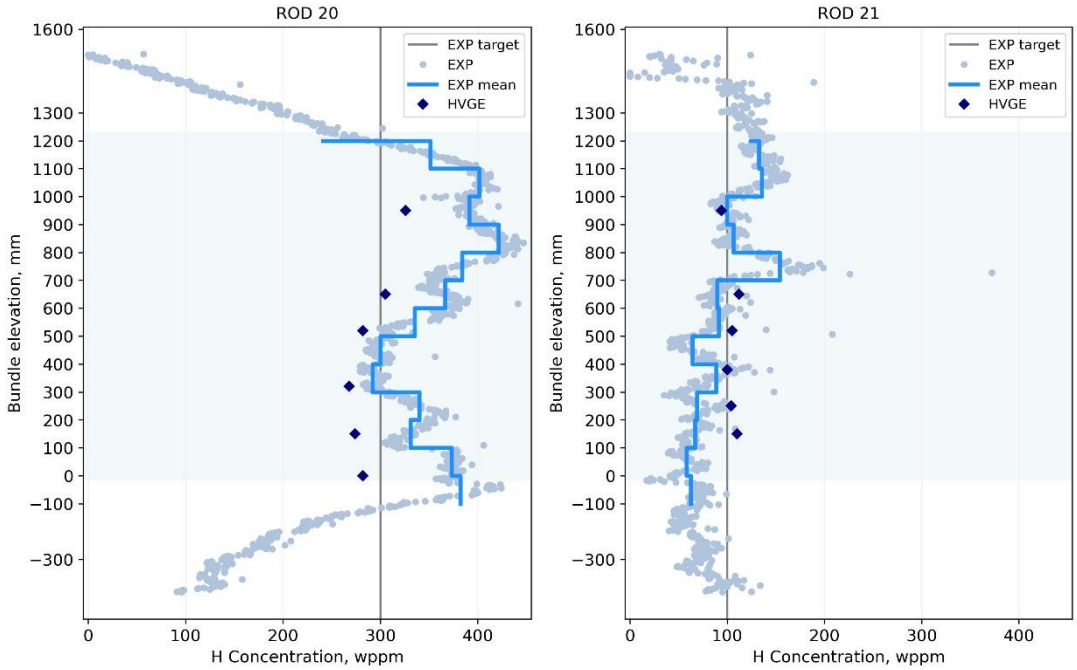

Fig. B. 10 Axial hydrogen distribution in rods № 20 (left) and № 21 (right): estimates vs. HVGE

C Estimation of Uncertainty in Hydride Morphology Metrics

Scope and approach

The uncertainty of the hydride morphology metrics derived from metallographic cross-sections was estimated by performing repeated independent measurements within the same method. Repeatability was quantified by measuring the scatter of data obtained from different sectors of the same tubular cross-section that corresponded to identical experimental conditions. In total, nine cross-sections were analysed, with two to eight independent measurements taken per cross-section. The chosen samples covered the full range of morphological metrics and parameters of the experiment.

In this work, the term “uncertainty” is used in the sense of the standard deviation (STD) of the measured metric, i.e. the characteristic scatter expected for a single measurement carried out under the same conditions.

Repeatability (within cross-section)

For each cross-section and hydride morphology metric, Radial Hydride Fraction (RHF) and Radial Hydride Continuity Path (RHCP), the mean value $\bar{x}$ and σ_{rep} were computed from the set of independent measurements x_i ($i = 1, \dots, n$). The sample standard deviation was calculated using the following equation:

$$\sigma_{rep} = \sqrt{\frac{1}{n-1}\sum_{i=1}^{n}(x_i - \bar{x})^2} \quad (1)$$

The individual measurements, corresponding mean values, and standard deviations are summarized in Tab. C. 1 and visualized in Fig. C. 1 and Fig. C. 2. The observed repeatability scatter was typically below $\sigma_{rep} = 0.05$ for RHF and below $\sigma_{rep} = 0.08$ for RHCP. These values have been chosen as conservative estimates of the standard deviation of RHF and RHCP. For several cross-sections at low values of the morphology metrics, the values of σ_{rep} were approximately 2–3 times smaller.

Tab. C. 1 Hydride morphology metrics: mean ± standard deviation (STD)

* – previous single measurement

** – anomaly of the hydride morphology (rod 13, 950 mm, 135°)

Rod	Cladding material	H concen-tration	Inner pressure	Eleva-tion, mm	Angle, °	RHF	RHCP
2	Zry-4	C_{max}	P_{max}	380	0	0.26	0.35
					135	0.23	0.29
					180*	0.24	0.30
					225	0.21	0.22
					270	0.25	0.35
					315	0.25	0.33
					mean ± STD	**0.24 ± 0.02**	**0.31 ± 0.05**
				650	0*	0.27	0.30
					45	0.32	0.36
					180	0.26	0.258
					225	0.23	0.263
					mean ± STD	**0.27 ± 0.04**	**0.30 ± 0.05**
3	Opt.ZIRLO	C_{min}	P_{max}	520	—*	0.19	0.28
					—	0.10	0.15
					—	0.11	0.13
					mean ± STD	**0.13 ± 0.05**	**0.19 ± 0.8**
4	Zry-4	C_{min}	P_{min}	520	0	0.17	0.26
					45*	0.19	0.20
					90	0.18	0.26
					315	0.16	0.22
					mean ± STD	**0.18 ± 0.01**	**0.24 ± 0.03**
6	Zry-4	C_{max}	P_{min}	520	0*	0.07	0.20
					90	0.10	0.26
					mean ± STD	**0.09 ±0.02**	**0.23 ± 0.04**
8	Zry-4	C_{min}	P_{max}	650	0	0.682	0.48
					45*	0.68	0.44
					90	0.56	0.34
					135	0.64	—
					225	0.63	—
					315	0.59	—
					mean ± STD	**0.63 ± 0.05**	**0.42 ± 0.07**
10	Opt.ZIRLO	C_{max}	P_{max}	650	0	0.05	0.14
					45	0.09	0.20
					90	0.09	0.19
					135	0.04	0.13
					180	0.04	0.12
					225	0.06	0.197
					270*	0.08	0.13
					315	0.10	0.23
					mean ± STD	**0.07 ± 0.02**	**0.17 ± 0.04**
13	Opt.ZIRLO	C_{min}	P_{min}	950	0	0.07	0.11
					45	0.05	0.13
					90	0.05	0.10
					135*	0.09**	0.23**
					225*	0.03	0.12
					270	0.03	0.119
					mean ± STD	**0.05 ±0.02**	**0.13 ± 0.05**
16	Opt.ZIRLO	C_{max}	P_{min}	800	0	0.02	0.11
					90	0.01	0.13
					180	0.02	0.125
					270*	0.03	0.14
					mean ± STD	**0.02 ± 0.01**	**0.13 ± 0.01**

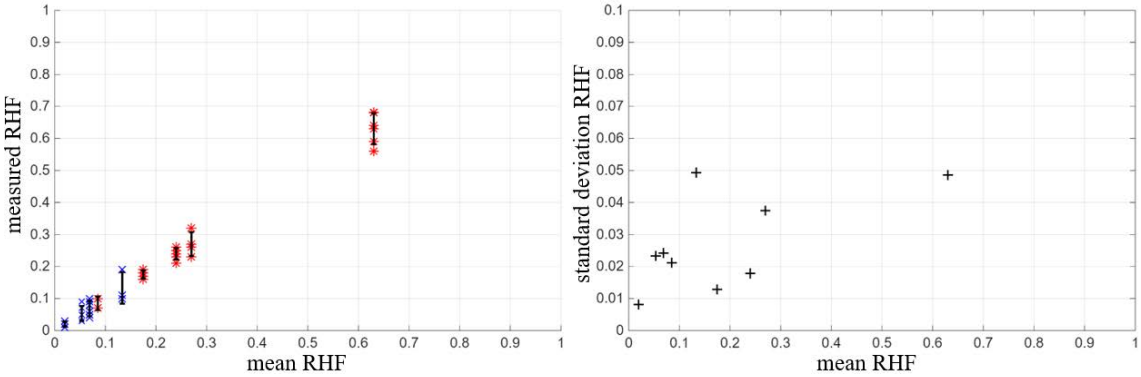

Fig. C. 1 RHF scattering (left) and standard deviation σ_1 (right)

Red markers – Zircaloy-4, blue markers – opt. ZIRLO, black lines – mean ± standard deviation.

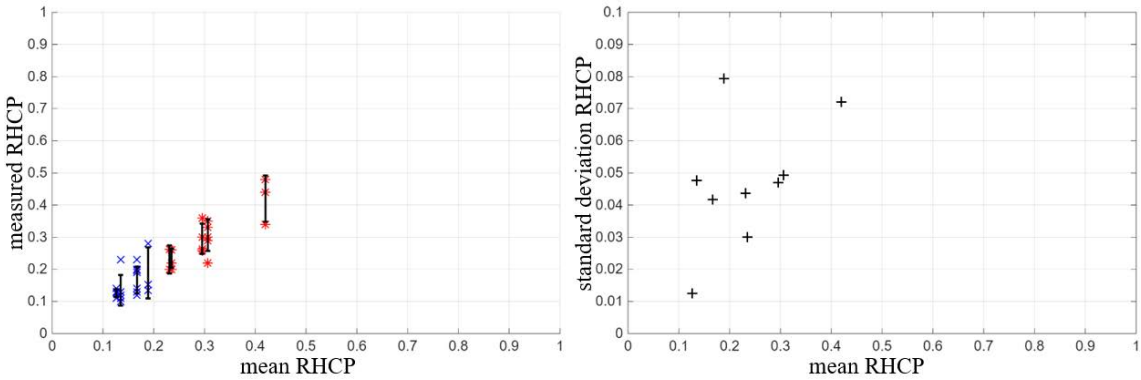

Fig. C. 2 RHCF scattering (left) and standard deviation σ_1 (right)

Red markers – Zircaloy-4, blue markers – opt. ZIRLO, black lines – mean ± standard deviation.

User effect

In addition to the scatter within cross-sections, a comparable contribution arises from variability in the identification and classification of hydride features, which depends on the user. This “user effect” was estimated through a comparison, in which two users analysed two micrographs independently using the same analysis approach. The results are reported in Tab. C. 2.

Due to the limited number of operators involved in the study (two), it is not possible to rigorously separate this contribution into systematic and random components. Nevertheless, the inter-operator difference provides a practical estimate of the characteristic operator-related variability. The corresponding standard deviation component is denoted as σ_{user}.

Tab. C. 2 User effect on hydride morphology assessment

*STD – standard deviation σ_2

Rod	Cladding material	H content	Inner pressure	Elevation, mm	Angle, °	RHF			RHCP		
						user 1	user 2	**STD***	user 1	user 2	**STD***
2	Zry-4	C_{max}	P_{max}	520	0	0.26	0.21	**0.04**	0.35	0.18	**0.12**
8	Zry-4	C_{min}	P_{max}	520	0	0.63	0.58	**0.04**	0.42	0.32	**0.07**

Combination of independent uncertainty components

Assuming that the repeatability component σ_{rep} and the user component σ_{user} are independent, the combined standard deviation can be estimated as:

$$\sigma_{tot} = \sqrt{\sigma_{rep}^2 + \sigma_{user}^2} \tag{2}$$

Using the conservative repeatability estimates $\sigma_{rep} = 0.05$ for RHF and $\sigma_{rep} = 0.08$ for RHCP, the total standard deviation is obtained from Eq. (2). Depending on the magnitude of the user-effect contribution inferred from Tab. C. 2, the combined uncertainty is on the order of $\sigma_{tot} \approx 0.07$ for RHF and $\sigma_{tot} \approx 0.1 - 0.14$ for RHCP.

Conclusion

Based on repeated within-cross-section measurements and a conservative approach to accounting for operator variability, the estimated standard deviation (1σ) of hydride morphology metrics is:

RHF: $\sigma_{tot} \approx 0.07$;

RHCP: $\sigma_{tot} \approx 0.14$

For Hydride Continuity Coefficient (HCC), the expected uncertainty is comparable to that for RHCP, and it is conservatively assumed not to be less than $\sigma_{tot} \approx 0.1$.

Gesellschaft für Anlagen- und Reaktorsicherheit (GRS) gGmbH

Schwertnergasse 1
50667 Köln
Telefon +49 221 2068-0
Telefax +49 221 2068-888

Boltzmannstraße 14
85748 Garching b. München
Telefon +49 89 32004-0
Telefax +49 89 32004-300

Kurfürstendamm 200
10719 Berlin
Telefon +49 30 88589-0
Telefax +49 30 88589-111

Theodor-Heuss-Straße 4
38122 Braunschweig
Telefon +49 531 8012-0
Telefax +49 531 8012-200

www.grs.de

ISBN 978-3-911727-49-5